

Hadronic Fragmentation Studies in Diffractive Deep Inelastic Scattering at HERA

Daniel Peter Traynor

Department of Physics,

Queen Mary,

University of London

*A thesis submitted in accordance with the regulations
for the Degree of Doctor of Philosophy
in the University of London*

September 25th, 2001

Declaration

No portion of the work referred to in this thesis has been submitted in support of an application for another degree or qualification of this or any other institute of learning.

Copyright

Copyright in text of this thesis rests with the Author. Copies (by any process) either in full, or of extracts, may be made only in accordance with the instructions given by the Author and lodged in the University Library. Details may be obtained from the Librarian. This page must form part of any such copies made. Further copies (by any process) of copies made in accordance with such instructions may not be made without the permission (in writing) of the Author.

The ownership of any intellectual property rights which may be described in this thesis is vested in the University of London, subject to any prior agreement to the contact, and may not be made available for use of third parties without the written permission of the University, which will prescribe the terms and conditions of any such agreement.

Abstract

Deep inelastic ep scattering (DIS) data recorded in 1996 using the H1 detector at HERA is used to study fragmentation spectra in the Breit frame of reference. An overview of the H1 detector is included as is the physics relevant to this analysis. The kinematics and cross-sections for inclusive and diffractive DIS, the different models of fragmentation and the Breit frame of reference are discussed. Details of data quality and the event selection, the Monte-Carlo simulation and the different methods for the reconstruction of event kinematics are also studied.

The rapidity spectra for the diffractive event selection clearly shows the expected suppression of tracks in the target hemisphere. The average charged multiplicity in the current hemisphere, $\langle n \rangle$, is shown to compare well with DIS at low β and with e^+e^- at high β . The evolution of the peak and width of the current hemisphere fragmentation functions for charged particles is studied as a function of photon virtuality, Q , and is found to agree with results obtained in non-diffractive DIS. Studies of the transverse momentum (p_t) spectra as a function of Q also showed that the diffractive and non-diffractive DIS data agree with each other.

Comparison with various models of diffraction are made with the resolved pomeron-model (H1 fit 2) providing the best description of the data. The results lend support to the concept of process independent parton fragmentation universality. The data can be interpreted in a picture where the diffractive final state originates from either a $q\bar{q}$ or a $q\bar{q}g$ partonic configuration but are also consistent with restricting the phase space that is implicit in making a selection of β .

Contents

1	H1 Detector	18
1.1	Introduction	18
1.2	HERA	18
1.3	Overview of H1	20
1.4	Tracking	20
1.4.1	Backward Drift Chamber (BDC)	22
1.4.2	Central Trackers (CIP,CIZ,CJC1,COP,COZ,CJC2)	23
1.4.3	Forward Tracker (FTD)	24
1.4.4	Silicon Detectors (CST and BST)	25
1.5	Calorimetry	25
1.5.1	SpaCal	26
1.5.2	Liquid Argon Calorimeter (LAr)	27
1.5.3	Tail Catcher (TC)	28
1.5.4	Plug Calorimeter	28
1.6	Forward Detectors	29
1.6.1	Forward Muon Detector (FMD)	29
1.6.2	Proton Remnant Tagger (PRT)	29
1.6.3	Forward Proton Spectrometer (FPS)	31
1.7	Other Components	31
1.7.1	Time-of-Flight	31
1.7.2	Luminosity	33

1.7.3	Trigger	33
2	<i>ep</i> Physics	36
2.1	Motivation	36
2.2	Introduction	37
2.3	DIS Kinematics	37
2.4	DIS Cross Section	39
2.5	Quark Parton Model	40
2.6	Photoproduction	47
3	Diffraction	49
3.1	Introduction	49
3.2	Diffraction Kinematics	49
3.3	Diffraction Cross Section	51
3.4	Models of Diffraction	51
4	Fragmentation	57
4.1	Introduction	57
4.2	Parton Cascade models	58
4.2.1	Parton Showers	58
4.2.2	Colour Dipole Model	59
4.3	Hadronisation Models	60
4.3.1	Local Parton-Hadron Duality	60
4.3.2	Independent Fragmentation	61
4.3.3	String Model	61
4.3.4	Cluster Model	62
5	Data Selection	64
5.1	Introduction	64
5.2	Physics Event Selection	64

5.2.1	Trigger	64
5.2.2	General DIS selection	65
5.2.3	Non-Diffractive (inclusive) DIS	66
5.2.4	Diffractive DIS	68
5.2.5	Tests for Trigger Bias	69
5.3	Track Selection	70
5.3.1	Central Track Selection	70
5.3.2	Forward Track Selection	72
5.3.3	Combined Tracks	72
5.4	Data Correction	73
5.5	Comparison with Monte-Carlo	74
5.5.1	DIS and MEAR	74
5.5.2	DIFFMY and MEAR	75
5.5.3	DIFFMY and RAPGAP	77
5.5.4	DIFFMX and RAPGAP	81
5.6	Studies of Systematic Errors	82
5.6.1	Energy Scales	82
5.6.2	Monte-Carlo Corrections	84
5.6.3	Detector Efficiency	85
6	Breit Frame Studies	87
6.1	Introduction	87
6.2	The Breit Frame	87
6.3	Event Kinematics	90
6.3.1	The Electron Method	90
6.3.2	The Jacquet-Blondel Method	91
6.3.3	The Double Angle Method	91
6.3.4	The Sigma Method	92
6.3.5	The Mixed Method	92

6.3.6	Resolution Studies	93
7	Rapidity Spectra	97
7.1	Introduction	97
7.2	Data Quality	99
7.3	Results	104
7.4	Model comparisons	109
7.5	Summary	110
8	The Fragmentation Function	115
8.1	Introduction	115
8.2	Data Quality	117
8.3	Average charged Multiplicity	122
8.4	Model comparisons	127
8.5	Peak Position and Width of the Fragmentation Function	128
8.6	Summary	132
9	Transverse Momentum Spectra	134
9.1	Introduction	134
9.2	Data Quality	135
9.3	Results	140
9.4	Summary	145

List of Figures

1.1	The HERA collider.	19
1.2	A 3D view of the H1 Detector	21
1.3	H1 Tracking Chambers	22
1.4	Schematic view showing the rotated layers and sectors of the BDC. . .	23
1.5	H1 Central Tracking Chambers	23
1.6	The Forward Tracker	25
1.7	The SpaCal calorimeter (electromagnetic and hadronic sections). Also shown are the central (CST) and backward (BST) scilicon trackers. . .	26
1.8	The upper half of the Liquid Argon Calorimeter. The dashed line shows the beam pipe, and <i>wvp</i> refers to the nominal interaction vertex position. .	27
1.9	The Forward Muon Detector (FMD)	30
1.10	The Proton Remnant Tagger (PRT)	30
1.11	The different paths followed by the background signal and the interac- tion signal to the SpaCal detector.	32
1.12	The energy and timing of signals in the SpaCal detector before any SpaCal ToF cuts have been applied.	32
2.1	Deep Inelastic scattering	38

2.2	Measurement of the reduced DIS scattering cross section. The H1 data are solid points and the fixed target μp data (BCDMS) are triangles. The curves represent the QCD calculation of the cross section (solid) and of the structure function F_2 (dashed) which in most of the x range is identical to the cross section. At lowest x the cross section is lower than F_2 which is attributed to the longitudinal structure function F_L .	41
2.3	Areas of validity for the different evolution schemes.	44
2.4	(a) Initial and (b) final state Compton QCD and (c) Boson Gluon Fusion.	46
2.5	(a) Direct and (b) resolved Photoproduction processes.	47
3.1	Generic diagram for diffractive DIS events. The four vectors of the system X (X), system Y (Y), the exchange photon (q), the incoming proton (P), and the four-momentum transfer at the proton vertex (t).	50
3.2	The diffractive structure function $F_2^{D(3)}$. The curves show Regge fits, the dashed curve is the contribution from the pomeron only, the dotted curve shows pomeron + interference, the solid curve shows the total pomeron + interference + reggeon contributions.	52
3.3	Diffractive DIS as modelled by photon fluctuations in the proton rest frame (left) and the PDF picture (right).	54
3.4	The β dependence of $F_2^{D(3)}$ at a constant value of $x_{\mathbb{P}} = 0.001$ in a parameterisation of the H1 $F_2^{D(3)}$ using the BEKW model. The dotted line is the $q\bar{q}g$ contribution, the dashed line is the transverse $q\bar{q}$ contribution, dashed-dotted line is the longitudinal $q\bar{q}$ contribution, the solid line is the full contribution.	55
3.5	Soft Colour Interactions. The dashed lines are soft gluons.	56
4.1	Initial state and final state parton showers	58
4.2	The Colour Dipole Model (CDM)	60
4.3	The Lund String Hadronisation Model	63

4.4	The Cluster Model of Hadronisation.	63
5.1	The $Q^2 - x$ plane showing the kinematic cuts.	67
5.2	A schematic representation of where events for the different selections are in $M_X - M_Y$ phase space. The circle represents the general selected phase space. This is then divided into different regions by the DIFFMX and DIFFMY selections which place different restrictions on M_X and M_Y	69
5.3	(a) The efficiency of S0 as a function of Q . The ratio of the ORed triggers S1->S13 (Total) over S0 for the multiplicity of tracks in the current region of the Breit frame for (b) DIS and (c) DIFFMY event selections.	71
5.4	The Z vertex position for MEAR Monte-Carlo (histogram) vs Data (points) (a) before and (b) after correction.	74
5.5	Scattered Electron Energy for MEAR Monte-Carlo (histogram) vs Data (points) (a) before reweighting and (b) after reweighting.	75
5.6	MEAR vs data for some event and track distributions for DIS events.	76
5.7	A comparison of the MEAR Monte-Carlo with data for the DIFFMY event selection.	77
5.8	The diffractive variables M_X , $x_{\mathcal{P}}$, β and η_{max} before altering the \mathcal{R} contribution for the DIFFMY selection.	79
5.9	The diffractive variables M_X , $x_{\mathcal{P}}$, β and η_{max} after altering the \mathcal{R} contribution for the DIFFMY selection.	80
5.10	RAPGAP vs data event and track distributions for the DIFFMY event selection.	81
5.11	The diffractive variables M_X , $x_{\mathcal{P}}$, β and η_{max} for the DIFFMX event selection.	82
5.12	RAPGAP vs data for some event and track distributions for the DIFFMX event selection.	83

6.1	The Breit frame of reference in the quark parton model.	88
6.2	e^+e^- centre of mass system. One hemisphere is equivalent to the current hemisphere.	89
6.3	Higher order processes as viewed in the Breit frame. (a) BGF events, (b) initial state QCD Compton, and (c) final state QCD Compton.	89
6.4	The resolution of Q^2 for the five different reconstruction methods in the Q^2 range $15 < Q^2 < 20 \text{ GeV}^2$	94
6.5	The resolution of x for the five different reconstruction methods in the Q^2 range $15 < Q^2 < 20 \text{ GeV}^2$	95
7.1	The rapidity plateau as seen in the Breit frame.	98
7.2	Comparison between uncorrected Data and reconstructed MEAR (for DIS) or RAPGAP (for the diffractive selections). (statistical errors only)	99
7.3	Acceptance correction factors with statistical errors. The correction factor for DIS in the last bin is 8, for DIFFMX is 20. (statistical errors only)	100
7.4	The resolution in Y as a function of Y for the different event selections. The solid line shows the bin-width ($Y \sim 0.6$). (statistical errors only)	101
7.5	The purity in Y as a function of Y for the different events selections. The solid line shows an (arbitrary) minimum value for the purity of 35%. In some intervals there are no data points because no tracks were both generated and reconstructed in that interval. (statistical errors only)	102
7.6	Comparison in rapidity of preliminary DIS results with the most recent (this analysis) DIS results (statistical and systematic errors).	103
7.7	Comparison in rapidity of two different definitions of deep-inelastic scattering, DIS ($egap > 0.5 \text{ GeV}$) and DIS2 (\overline{DIFFMY}) (statistical errors only). Note that it is expected that the results should not be differentially affected by the systematic errors.	105

7.8	Rapidity plateau data comparing DIS, DIFFMX and DIFFMY selections (statistical and systematic errors).	107
7.9	Rapidity plateau data comparing DIFFMY for $\beta < 0.2$ and $\beta > 0.2$ (statistical and systematic errors).	108
7.10	Comparison of rapidity distributions with predictions from a resolved pomeron model using three different parameterisations from H1 and the saturation model. For (a) the DIFFMY selections, (b) low β DIFFMY, and (c) high β DIFFMY.	111
7.11	Comparison of rapidity distributions from the LEPTO Monte-Carlo with different implementations of Soft Colour Interactions (SCI). For (a) the DIFFMY selections, (b) low β DIFFMY, and (c) high β DIFFMY. Note that only in the high β DIFFMY sample can fits 2 and 3 be differentiated.	112
8.1	The fragmentation function, $1/Ndn^\pm/dx_p$, of the DIFFMY event selection for the current hemisphere of the Breit frame (raw distributions and statistical errors only).	116
8.2	The fragmentation function, $D(\xi)$, of the DIFFMY event selection for the current hemisphere of the Breit frame (raw distributions and statistical errors only).	117
8.3	Comparison of uncorrected data and RAPGAP Monte-Carlo for the DIFFMY event selection (statistical errors only).	118
8.4	Acceptance correction factors applied to the data for the DIFFMY event selection (statistical errors only).	119
8.5	The resolution in ξ as a function of ξ for the DIFFMY event selection. The solid line shows the bin-width ($\xi \sim 0.25$) (statistical errors only).	120
8.6	The purity in ξ as a function of ξ for the DIFFMY event selection. The solid line shows a minimum value for the purity of 35% (statistical errors only).	121

8.7	Comparison of Preliminary DIS results with the most recent (this analysis) DIS results for the $\langle n \rangle$. (statistical and systematic errors). The DIS data points have been shifted by 0.1 GeV for ease of comparison.	123
8.8	Data comparing $\langle n \rangle$ for DIS, DIFFMX and DIFFMY selections (statistical and systematic errors).	124
8.9	The ratio of events with an empty current hemisphere as a function of the Q^2 bin for DIS, DIFFMX and DIFFMY event selections. (statistical errors only)	125
8.10	Comparison of $\langle n \rangle$ for DIFFMY $\beta < 0.2$ and DIFFMY $\beta > 0.2$. (statistical and systematic errors). The DIS data points have been shifted by 0.1 GeV for ease of comparison.	126
8.11	Comparison of $\langle n \rangle$ for two different definitions of deep-inelastic scattering, DIS ($egap > 0.5$ GeV) and DIS2 (\overline{DIFFMY}). (statistical errors only)	127
8.12	The averaged charged multiplicity as a function of the energy scale Q . The solid curve is a fit to many e^+e^- results as a function of the centre of mass energy E^* ($E^* = Q$), the dashed line a prediction for the MEAR Monte-Carlo for DIS events and the dotted and dashed-dotted lines comes from RAPGAP using the resolved P model and the fit 2 parameterisation from H1.	128
8.13	The average charged multiplicities as a function of the energy scale Q . The data is compared with a prediction of the saturation model.	129
8.14	The fragmentation function, $D(\xi)$, for the DIFFMY event selection after acceptance corrections together with Gaussian fits in the region of the peak. (corrected distributions and statistical errors only)	130

8.15	The energy evolution of (a) the peak position and (b) the width of the fragmentation function for both DIS and DIFFMY selections. The solid (dashed) line is the simultaneous fit of the MLLA parameterisation to DIS (DIFFMY) data.	131
9.1	The transverse momentum spectra, $\frac{1}{N}dn_{tracks}^{\pm}/dp_t^2$, as a function of p_t for charged hadrons in the current hemisphere of the Breit frame (statistical errors only). The fits shown are made within restricted p_t ranges but plotted over the whole p_t range.	136
9.2	Comparison of uncorrected data and RAPGAP Monte-Carlo for the DIFFMY event selection. (statistical errors only)	137
9.3	Acceptance correction factors applied to the data for the DIFFMY event selection. (statistical errors only)	138
9.4	The resolution of p_t as a function of reconstructed p_t for the DIFFMY event selection (RAPGAP Monte-Carlo). The solid line shows the bin-width employed. (statistical errors only)	139
9.5	The purity in p_t as a function of reconstructed p_t for the DIFFMY event selection (RAPGAP Monte-Carlo). The solid line shows an arbitrary minimum value for the purity of 35%. (statistical errors only)	140
9.6	The b values of the exponential fits as a function of Q for DIS (stars) and DIFFMY (open triangles). The DIS data points have been shifted to the right by 0.1 GeV for ease of comparison. The inner error bars are statistical and outer error bars also include systematic errors added in quadrature.	141
9.7	The m values of the power law fits as a function of Q for DIS (stars) and DIFFMY (open triangles). The DIS data points have been shifted to the right by 0.1 GeV for ease of comparison. The inner error bars are statistical and outer error bars also include systematic errors added in quadrature.	142

9.8 The m values of the power law fits as a function of Q for DIS only. Also shown are three different fits to the data. The inner error bars are statistical and outer error bars also include systematic errors added in quadrature. 144

List of Tables

1.1	The summary of H1 operation since 1994. In shifted vertex running (svtx) the interaction vertex is shifted away from the nominal position to extend the kinematic range accessible by H1. The value $\langle z - iP \rangle$ represents the mean distance from the nominal interaction vertex. In minimum bias running (mbr) the prescales on the trigger setup are changed to allow more low Q^2 events to be recorded. The centre of mass energy is E_{cm} . The luminosity recorded on tape with the major detectors fully operational and after corrections for satellite bunches is L , with percentage error dL	33
1.2	Cross sections and rates at design luminosity ($L = 1.5 \times 10^{31} \text{ cm}^2\text{s}^{-1}$)	34
6.1	Resolution of Q^2 ($gQ^2 - Q^2$)/ gQ^2 (g indicates generator value)	93
6.2	Resolution of y ($gy - y$)/ gy (g indicates generator value)	93
6.3	Resolution of x ($gx - x$)/ gx (g indicates generator value). Highlighted values show the best resolution.	96
7.1	$1/Ndn/dY$ as a function of Y for the DIS, DIFFMX and DIFFMY selections. The errors are the statistical error and then systematic error	114
7.2	$1/Ndn/dY$ as a function of Y for the low and high β DIFFMY selections. The errors are the statistical error and then systematic error .	114
8.1	The $\langle n \rangle$ as a function of Q^2 for the DIS, DIFFMX and DIFFMY selections. The errors are the statistical error and then systematic error.	133

8.2	The $\langle n \rangle$ as a function of Q^2 for the low and high β DIFFMY selections. The errors are the statistical error and then systematic error	133
8.3	The energy evolution of the peak position and width of the fragmentation function for both DIS and DIFFMY selections. The errors are the statistical error and then systematic error	133
9.1	Results from the exponential fits to the p_t spectra of the DIS and DIFFMY selections. The errors are the statistical error and then systematic error	145
9.2	Results from the power law fits to the p_t spectra of the DIS and DIFFMY selections. The errors are the statistical error and then systematic error except for A where only the statistical error is given. . .	146

Chapter 1

H1 Detector

1.1 Introduction

This chapter gives an overview of the HERA accelerator and the H1 detector and then a detailed discussion of the components of the H1 detector concentrating on those systems important to the analysis.

1.2 HERA

HERA [3] is the world's only electron-proton storage ring and has been built at the DESY laboratory in Hamburg, Germany. It consists of two independent accelerators designed to accelerate, store and collide counter-rotating beams of electrons¹ and protons. In 1996 the accelerators collided 27.5 GeV electrons with 820 GeV protons² at a centre of mass energy (\sqrt{s}) of 300 GeV. The lay-out of HERA is shown in figure 1.1.

HERA is made up of a series of stages. Two linear accelerators produce beams of particles (450 MeV electrons and 50 MeV protons) which accumulate in the DESY II and DESY III storage rings. The particles are then accelerated to 8 GeV and are

¹Through this thesis electrons and positons will be generically referred to as electrons.

²From 1998 HERA has operated with 920 GeV protons.

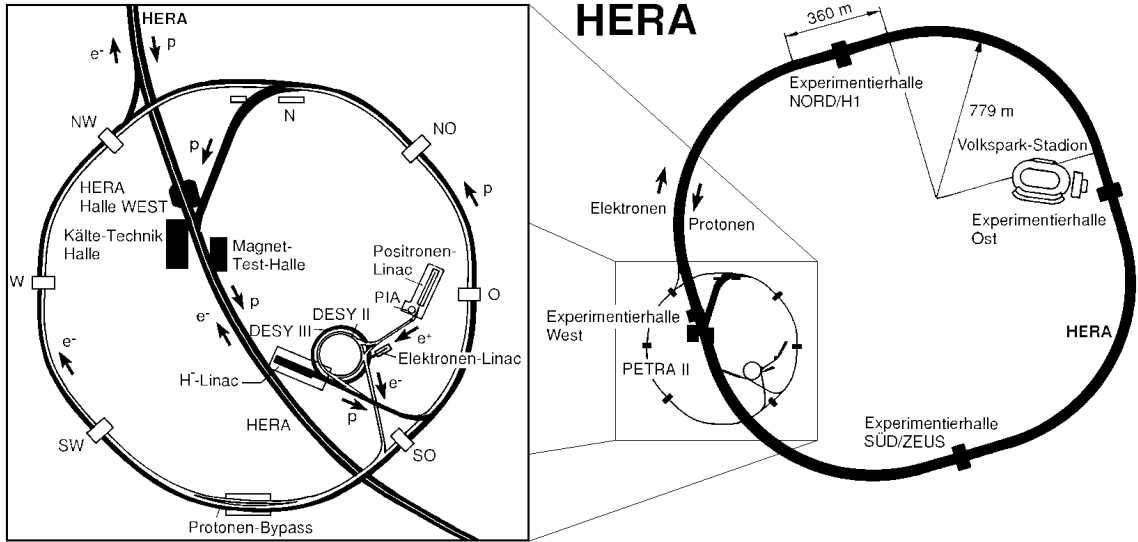


Figure 1.1: The HERA collider.

injected into the PETRA ring. In PETRA the electrons are accelerated to 12 GeV and the protons to 40 GeV and then enter HERA in groups of up to 70 bunches. Six injection cycles are needed to fill HERA with a possible maximum of 210 bunches.

In practice there are 175 paired bunches of electrons and protons which cross at the interaction points every 96 ns. In addition there are 14 unpaired electron bunches and 6 unpaired proton bunches which are used for calibration and background studies. Typical electron currents are 30 mA and proton currents are 80 mA. The design specific luminosity is $1.5 \times 10^{31} \text{ cm}^{-2}\text{s}^{-1}$ and the highest luminosity reached in 2000 was $1.7 \times 10^{31} \text{ cm}^{-2}\text{s}^{-1}$.

There are four interaction points at HERA but only two detectors (H1 and ZEUS) are designed to study electron-proton collisions. Two other experiments have more specialised functions. HERMES examines collisions between a polarised electron beam and atomic nuclei in order to measure the polarised nucleon structure functions. HERA-B, which was commissioned in 1999-2000, is investigating B meson production via the interaction of the proton beam halo with wires placed inside the beam pipe.

1.3 Overview of H1

A detailed description of the H1 detector can be found in [4, 5].

H1 uses a right handed coordinate system with the z -axis running parallel to the beams with the incoming proton direction defining the positive z direction and the y -axis pointing vertically up. The polar angle θ is measured with respect to the z -axis such that a non-scattered proton has an angle of $\theta = 0^\circ$ and is said to be going in the forward direction. Similarly a non-scattered electron has an angle of $\theta = 180^\circ$ and is said to be going in the backward direction.

A 3D view showing the main components of the H1 detector is shown in figure 1.2. H1 measures charged particles by tracking chambers (2,3) and muon chambers (9) with a 1.2 TeV magnetic field produced by a superconducting coil (6), and energy measurements are made by calorimeters (4,5,10,12,13).

The asymmetric beam energies at HERA means that there will be a larger multiplicity and energy flow in the forward direction. As a result the H1 detector has an asymmetric design to enhance the detection of the dense multi-particle final state from the break up of the proton in the forward direction. The backward region is optimised to measure the scattered electron energy and position, since the electron is important for determining the event kinematics in measurements of the DIS cross section.

1.4 Tracking

The H1 tracking system is designed to provide simultaneous track triggering, reconstruction and particle identification for the event topology particular to HERA electron proton collisions. The tracking system is divided into three regions; backward, central and forward (figure 1.3).

HERA Experiment H1

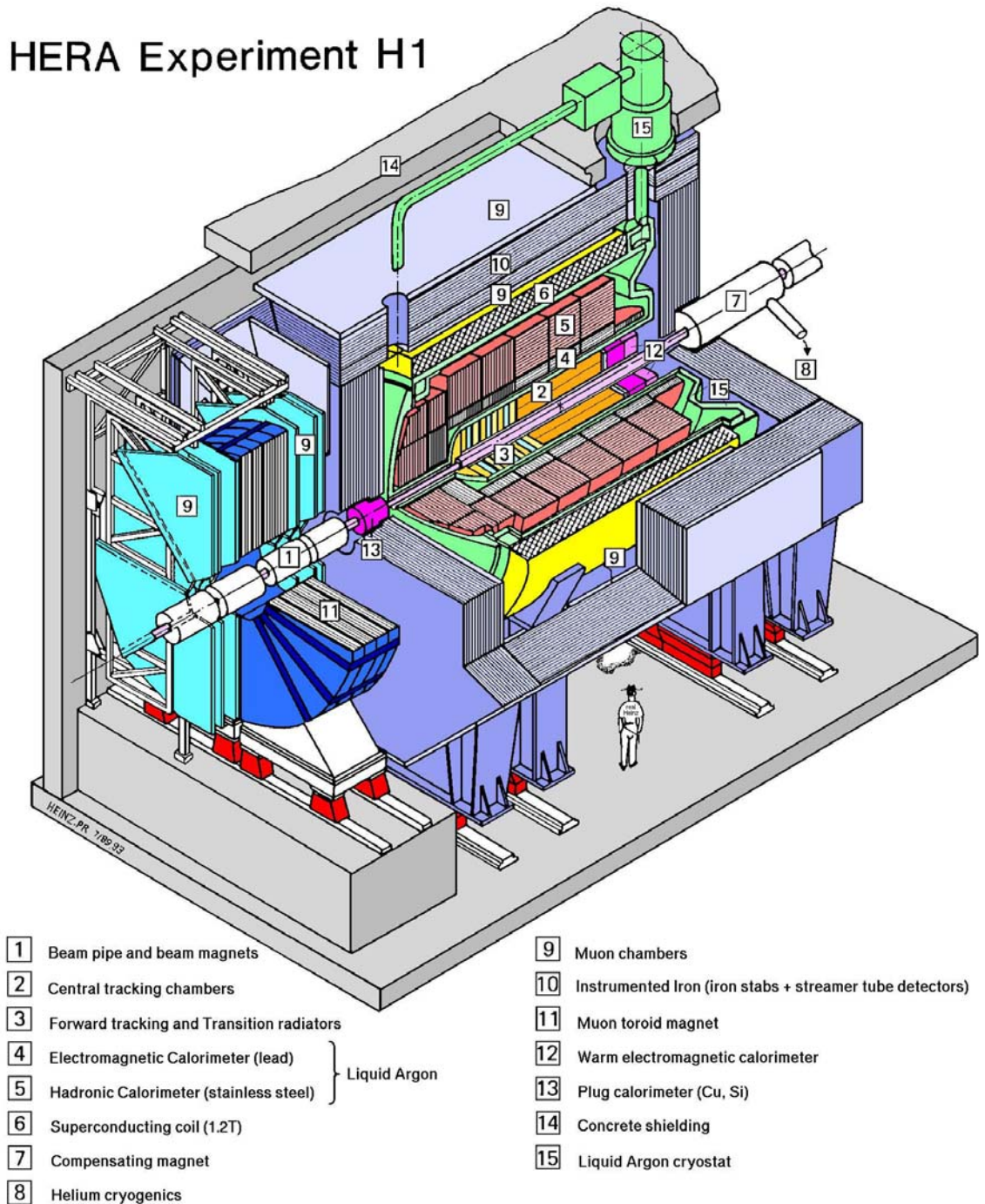


Figure 1.2: A 3D view of the H1 Detector

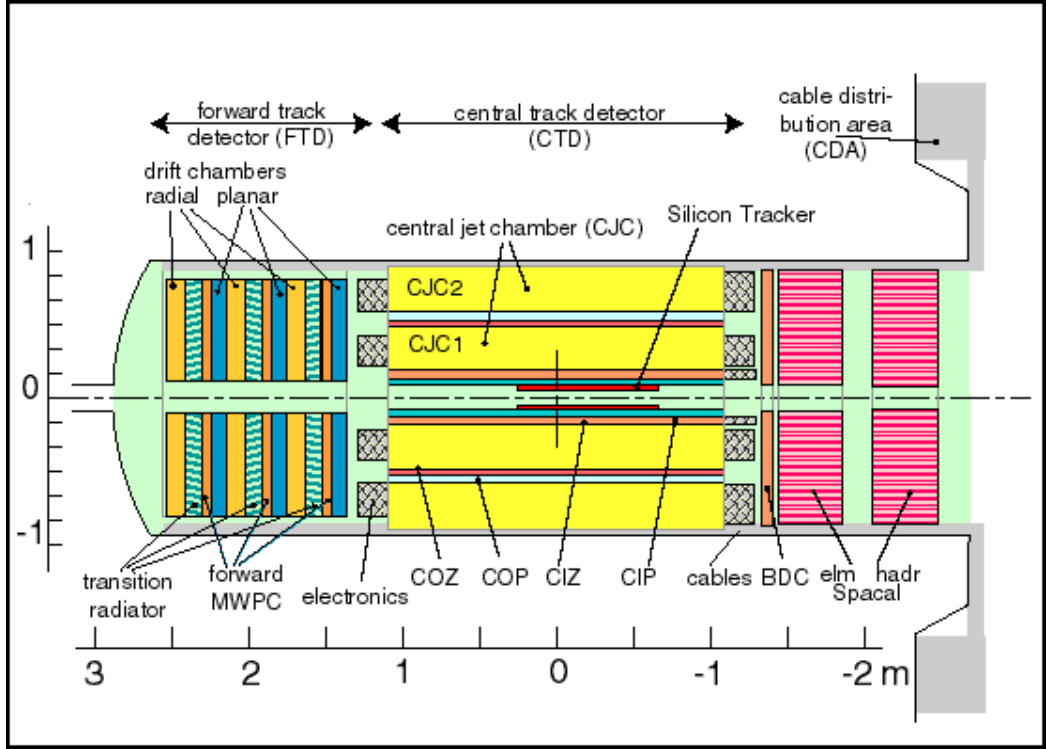


Figure 1.3: H1 Tracking Chambers

1.4.1 Backward Drift Chamber (BDC)

The Backward Drift Chamber (BDC) is designed to provide accurate measurement of the scattered electron in the region $153^\circ < \theta < 177.5^\circ$ which corresponds roughly to $1 < Q^2 < 100 \text{ GeV}^2$. The Backward Drift Chamber (BDC) consists of four double-layer drift chambers mounted just in front of the SpaCal calorimeter. Each layer is divided into 8 sectors, each sector consists of 32 drift cells thus the readout consists of 2048 channels. Sense wires are arranged to provide the best measurement of the polar (θ) angle of the scattered electron. Each double layer is rotated by 11.25° with respect to the previous layer to obtain some measurement of the ϕ angle. The resolution of the BDC for the measurement of the polar angle of the scattered electron is better than 1 mrad.

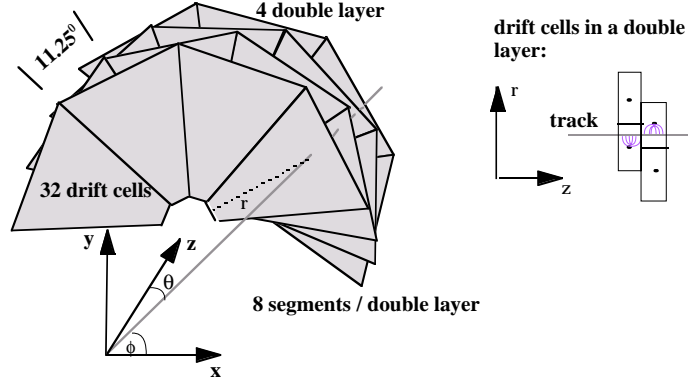


Figure 1.4: Schematic view showing the rotated layers and sectors of the BDC.

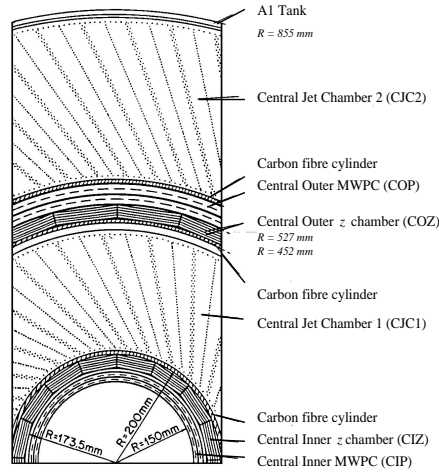


Figure 1.5: H1 Central Tracking Chambers

1.4.2 Central Trackers (CIP,CIZ,CJC1,COP,COZ,CJC2)

The Central Tracking Detector (CTD) [6] consists of six chambers which cover the region $25^\circ < \theta < 155^\circ$ and are shown in figure 1.5.

Track reconstruction is performed by the inner and outer Central Jet Chambers (CJC1 and CJC2). The wires of these chambers run parallel to the beam pipe and are grouped into drift cells which are shifted 30° from the radial direction so that ionisation electrons drift perpendicular to the high momentum tracks in the ambient magnetic field and the left-right ambiguity is also resolved. The chambers have a resolution in the $r - \vartheta$ plane of $170 \mu\text{m}$ and in the z direction of 2.5 cm .

To obtain a better measurement of the z -coordinate there are two sets of drift

chambers, the Central inner and outer z -chamber (CIZ, COZ), with sense wires perpendicular to the beam pipe. The CIZ covers the region $16^\circ < \theta < 169^\circ$, and the COZ covers the region $25^\circ < \theta < 156^\circ$. This improves the resolution in z to between $200 - 500 \mu\text{m}$

Triggering and timing information for the central trackers is supplied by two proportional chambers. The Central Inner Proportional chamber (CIP) and the Central Outer Proportional chamber (COP). Information from the proportional chambers can be used to deduce the event vertex, and validate other detector data such as calorimeter and muon information. Background from uncorrelated noise and synchrotron radiation can be rejected as well.

1.4.3 Forward Tracker (FTD)

Due to the asymmetry of the electron and proton beam energies many charged particles are produced at small angles to the incident proton (forward) direction. The forward tracker (FTD) [7] is designed to maintain good efficiency for triggering and reconstruction in the forward region ($5^\circ < \theta < 25^\circ$). The FTD consists of three identical super modules arranged along the z axis (figure 1.6). Each super module includes

1. Three layers of planar drift chambers at different orientations to provide accurate θ measurements. Each planar module gives an angular resolution in the $x - y$ plane of less than 1 mm.
2. A multi-wire proportional chamber (FWPC) for fast triggering. A track that crosses at least two of the three FWPC modules (i.e. in the angular range $5.1^\circ < \theta < 21.6^\circ$) has a timing resolution of 20 ns, which is less than the bunch crossing rate.
3. A passive transition radiator and a radial wire chamber which provides accurate $r\phi$ information, moderate radius measurement by charge division and limited

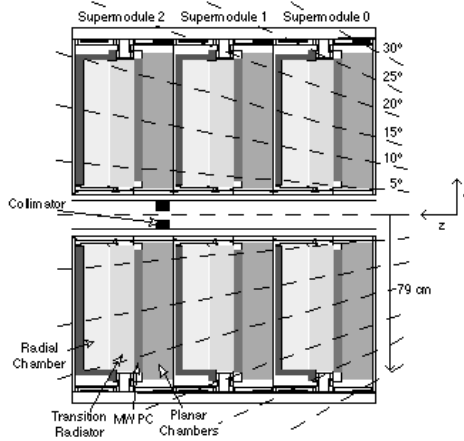


Figure 1.6: The Forward Tracker

particle identification by measuring the transition radiation produced immediately upstream (although this has never successfully worked). The radial chambers give a momentum measurement with a resolution of $\sigma_p/p^2 < 0.003 \text{ GeV}^{-1}$.

1.4.4 Silicon Detectors (CST and BST)

The Silicon Tracker is divided into two sections (figure 1.7), the Central Silicon Tracker (CST) and the Backward Silicon Tracker (BST). They are positioned between the beam pipe and the CTD. The CST gives an improved vertex determination (e.g. of use for B meson decays) while the BST is used to improve the reconstruction of small angle tracks in the backward region (e.g. scattered electrons close to 180°). Information from the silicon trackers is still not presently available for analysis.

1.5 Calorimetry

The calorimetry in H1 is composed of several different detectors. The LAr calorimeter covers the polar angular range $3^\circ < \theta < 154^\circ$. The calorimeter coverage is completed by a PLUG calorimeter in the forward direction covering $0.3^\circ < \theta < 4^\circ$ and by the SpaCal calorimeter in the backward region covering $153^\circ < \theta < 177.5^\circ$. The tail-catcher system (TC) is used to provide a rough measurement of hadronic particle

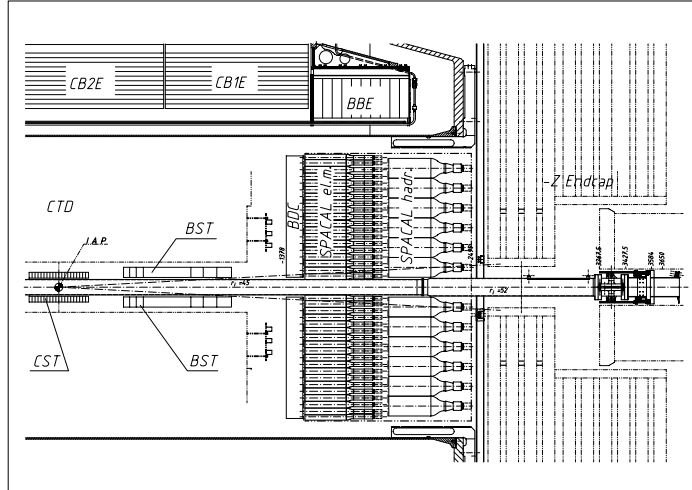


Figure 1.7: The SpaCal calorimeter (electromagnetic and hadronic sections). Also shown are the central (CST) and backward (BST) silicon trackers.

leakage out of the LAr calorimeter. Both the LAr and SpaCal are separated into two longitudinal sections, one for the accurate measurement of electromagnetic particles (including the scattered electron) and the second to complete the measurement of hadronic activity.

1.5.1 SpaCal

The Lead Scintillating-fibre Spaghetti Calorimeter (SpaCal) [8] is primarily designed to detect, trigger and measure the scattered electron from DIS events in the low Q^2 region ($1 < Q^2 < 100 \text{ GeV}^2$), and to measure hadrons produced in photoproduction (figure 1.7).

The electromagnetic section is constructed from 0.5 mm radius scintillating plastic fibres embedded in a lead absorber matrix, giving a lead-to-fibre volume ratio of 2.3 : 1, a radiation depth of 28 lengths (X_0) and an interaction depth of 1 length (λ). The SpaCal also has a timing resolution of less than 1 ns making it the most accurate device for timing ep interactions in HERA. It has an energy resolution for a 27.5 GeV electron of $\sigma_E/E = 7.5\%/\sqrt{E \text{ (GeV)}}$ with a scale uncertainty of 1.0 %

The hadronic section is made in a similar way but with a fibre radius of 1 mm to give a lead-to-fibre ratio of 3.4 : 1. It adds one further interaction length and has an

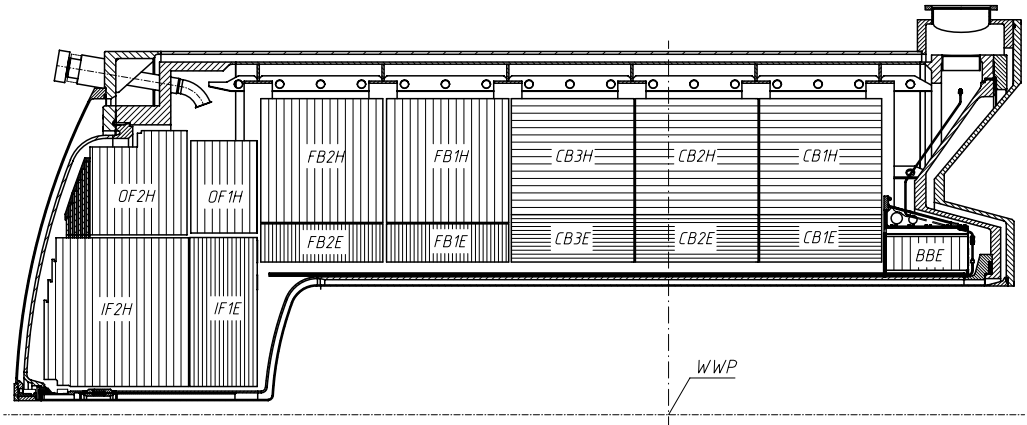


Figure 1.8: The upper half of the Liquid Argon Calorimeter. The dashed line shows the beam pipe, and *wvp* refers to the nominal interaction vertex position.

energy resolution for hadrons of $\sigma_E/E = 30\%/\sqrt{E \text{ (GeV)}}$.

1.5.2 Liquid Argon Calorimeter (LAR)

The Liquid Argon Calorimeter (LAR) [9] covers the region $4^\circ < \theta < 153^\circ$ as shown in figure 1.8. It is divided into two longitudinal parts: an electromagnetic section, which can be used for the detection and measurement of scattered electrons at high Q^2 , and a hadronic section for the measurement of the hadronic final state.

The calorimeter is housed in a cryostat *inside* the main solenoid coil reducing the amount of dead material in front of the calorimeter. The calorimeter is split into eight self-supporting “wheels” along the beam axis. The first 6 wheels in the backward and central region are split into 8 segments (octants) in ϕ , while the two forward wheels are split into two segments only, to minimise dead regions due to cracks. The most backward wheel is called the BBE and has no hadronic section. The calorimeter is highly segmented with about 45000 readout cells.

The electromagnetic section uses lead plates as absorbers, has a total thickness of 20 to 30 radiation lengths and an energy resolution of $\sigma_E/E \simeq 0.12/\sqrt{E \text{ (GeV)}}$. The hadronic part uses stainless steel as absorber, has a thickness of 5 to 8 interaction lengths and an energy resolution $\sigma_E/E \simeq 0.5/\sqrt{E \text{ (GeV)}}$. The electromagnetic energy

scale is known to 3% while the hadronic energy scale is known to 4%.

The energy measured has to be corrected for the losses due to absorption by dead material in front of the calorimeter and cracks between the segments and wheels within the calorimeter. These losses have been estimated to be about 10% in low Q^2 DIS events. The LAr calorimeter is a non-compensating calorimeter, with the response to hadrons about 30% smaller than to electrons of the same energy. A weighting procedure is used to correct for this.

1.5.3 Tail Catcher (TC)

The iron return yoke of the main solenoid magnet surrounds all major detector components of H1. It is interleaved with slits which can be instrumented to provide both a measure of the energy (serving as a hadronic Tail Catcher (TC) for the LAr) and for measurement of penetrating tracks (muons). The tail catcher has a total depth of 4.5 interaction lengths and an energy resolution of $150\%/\sqrt{E}$ (GeV).

1.5.4 Plug Calorimeter

The Plug calorimeter (PLUG) was designed to fill the gap in acceptance between the beam pipe and the LAr calorimeter. Its purpose is to minimise the loss of energy and longitudinal momentum improving the determination of the event kinematics from the hadronic final state. In addition the energy emitted in a narrow cone around the beam pipe can be used to separate the proton jet as well as to veto beam gas and beam wall background.

The Plug is a sampling calorimeter made up of nine layers of copper absorber plates interleaved with eight sensitive layers of silicon detectors with a total depth of 4.3 interaction lengths. Lateral and longitudinal shower leakage and coarse sampling limits the resolution of the plug to only $150\%/\sqrt{E}$ (GeV).

Due to radiation damage and consequent poor modelling of the Plug calorimeter in the Monte-Carlo simulation, the Plug is not used in this analysis.

1.6 Forward Detectors

In this analysis the forward detectors are used to detect a gap in rapidity between the observed hadronic system and the scattered proton. This is the classic signature of a diffractive event.

1.6.1 Forward Muon Detector (FMD)

The Forward Muon Detector (FMD) is primarily designed for the triggering and reconstruction of muons, for this purpose it has an angular coverage of $3^\circ < \theta < 17^\circ$ (figure 1.9). The FMD comprises of six double layers of drift chambers, three either side of a toroidal magnet. To reduce background, a “hit” in the FMD requires that both layers fire in coincidence. The toroidal magnet bends the muons and allows their momenta to be measured in the range $5 < p < 100$ GeV.

The FMD is also sensitive to particles at much lower angles due to secondary scattering from the beam pipe or with beam pipe gas. This property of the FMD is also used to help detect if there is a rapidity gap in the event. To reduce background from synchrotron radiation only the three layers behind the toroid magnet are used. The FMD is sensitive to particles in the pseudo rapidity range $2.5 < \eta < 6$.

1.6.2 Proton Remnant Tagger (PRT)

The proton remnant tagger (PRT) is used to help detect particles from the dissociated proton in non-diffractive DIS. It is situated 24 m from the nominal interaction point in the forward direction. It is made up of seven individual detectors arranged around and between the electron and proton beam pipes (figure 1.10). Each detector consists of two separate scintillators. Only if both scintillators fire in coincidence with the time expected for particles from an ep interaction to reach the tagger is a signal registered. The PRT is sensitive to particles in the pseudo-rapidity range $6 < \eta < 8$.

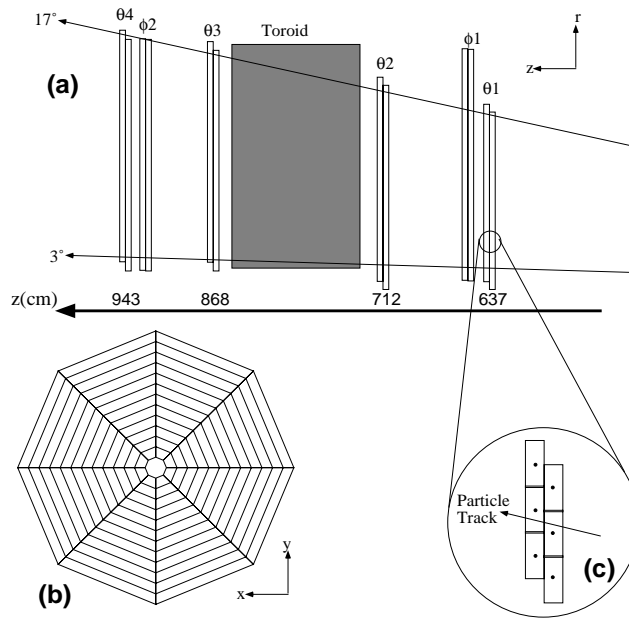


Figure 1.9: The Forward Muon Detector (FMD)

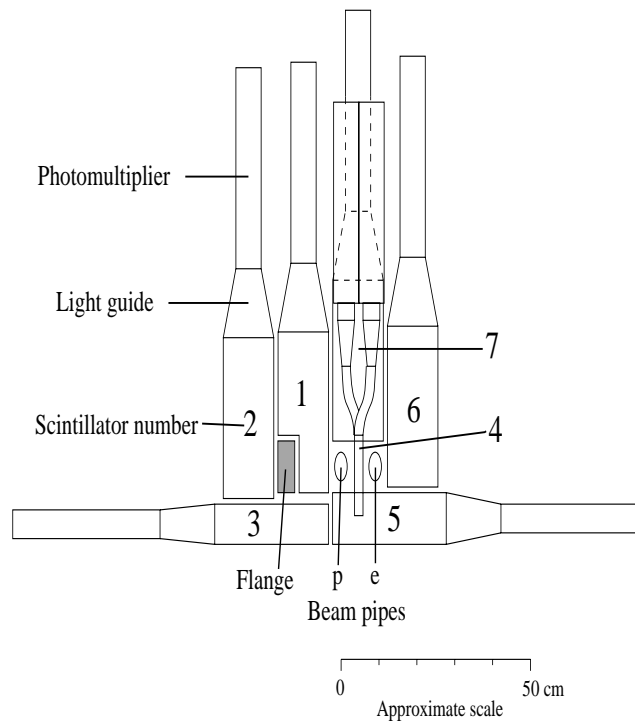


Figure 1.10: The Proton Remnant Tagger (PRT)

1.6.3 Forward Proton Spectrometer (FPS)

The Forward Proton Spectrometer (FPS) is made up of two stations at 81 m and 90 m. They use Roman pots which are lowered into the beam pipe to measure low angle scattered protons from diffractive events. They are not used in this analysis.

1.7 Other Components

1.7.1 Time-of-Flight

The Time-of-Flight (ToF) system is composed of several scintillating detectors located near the beam pipe in the forward and backward direction whose timing measurement is used to reject background. Beam-induced background is a result of interaction between the beam and beam pipe gas or the beam pipe wall. The ToF system uses the difference in time of arrival between particles from the interaction point and particles from the background, which result from the different paths they follow to get to the detector, to reject background events.

In addition to the scintillating detectors the ToF information from the SpaCal detector is also used. Particles from the interaction point have to travel for an additional three metres compared with background particles from the proton beam this corresponds to a Time-of-Flight difference of about 10 ns (figure 1.11).

In addition to the background signal from the main proton bunches there also exists a second background signal from proton satellite bunches. Proton satellite bunches arise from protons escaping into adjacent radio frequency buckets either side (± 5 ns) of the main proton bunch. Figure 1.12 shows the energy (the raw ADC value from the electronics) and time (in ns) of signals in the SpaCal from several thousand events. The physics signal is clearly seen at 19 ns while the main proton beam background is at 8 ns and the satellite background is at 14 ns.

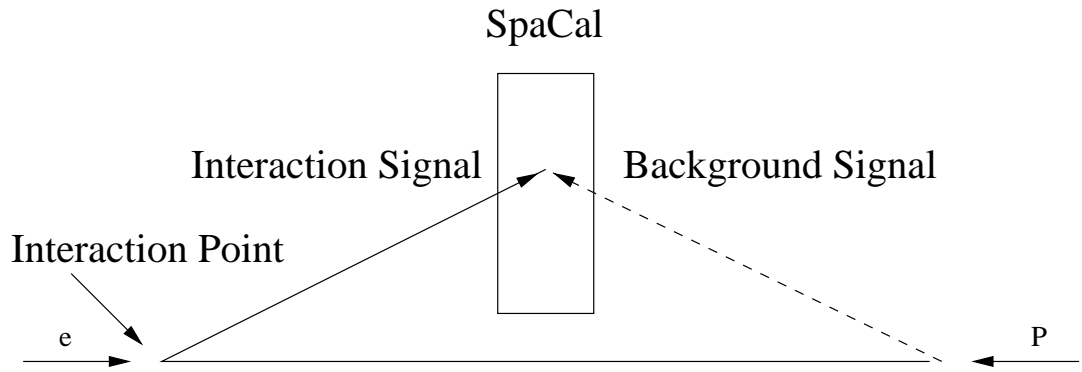


Figure 1.11: The different paths followed by the background signal and the interaction signal to the SpaCal detector.

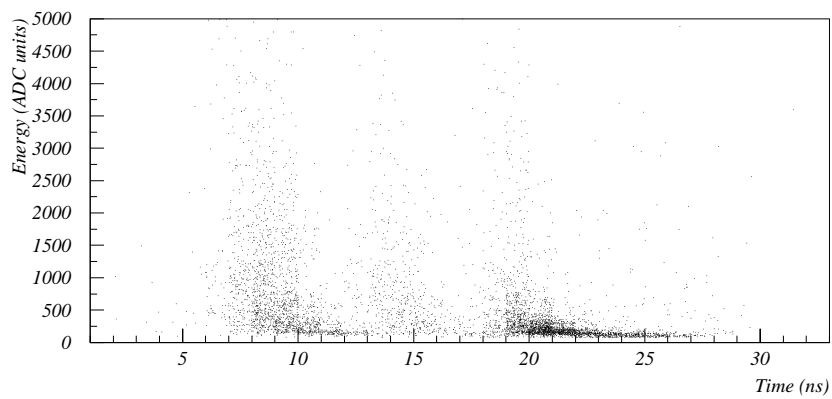


Figure 1.12: The energy and timing of signals in the SpaCal detector before any SpaCal ToF cuts have been applied.

Year	type	e^+/e^-	E_{cm} (GeV)	$\langle z - \text{iP} \rangle$ (cm)	L (pb^{-1}) Physics	dL/L (%)
2000	svtx	e^+	318.4	+72.2	0.678	3.6
2000		e^+	318.4	+7.06	48.67	1.5
1999	mbr	e^+	318.4	+2.9	4.37	1.2
1999		e^+	318.4	-0.2	18.86	1.5
1999		e^-	318.4	-0.5	10.74	1.3
1998		e^-	318.4	-0.8	3.38	1.3
1997	mbr	e^+	300.6	-0.3	2.47	1.5
1997		e^+	300.6	-0.9	22.21	1.5
1996		e^+	300.6	-1.5	8.35	1.8
1995		e^+	300.6	-1.7	4.19	1.4
1995	svtx	e^+	300.6	+70.1	0.12	2.6
1994		e^+	300.6	+5.0	2.82	1.5

Table 1.1: The summary of H1 operation since 1994. In shifted vertex running (svtx) the interaction vertex is shifted away from the nominal position to extend the kinematic range accessible by H1. The value $\langle z - \text{iP} \rangle$ represents the mean distance from the nominal interaction vertex. In minimum bias running (mbr) the prescales on the trigger setup are changed to allow more low Q^2 events to be recorded. The centre of mass energy is E_{cm} . The luminosity recorded on tape with the major detectors fully operational and after corrections for satellite bunches is L , with percentage error dL .

1.7.2 Luminosity

The luminosity system relies on measurement of the known Bethe-Heitler reaction ($ep \rightarrow ep\gamma$) cross-section. The main source of background is from bremsstrahlung from beam gas $eA \rightarrow eA\gamma$, which is removed statistically using data from the electron pilot bunches. The proton satellite bunches can contribute up to 10% of the proton current and their contribution has to be removed from the luminosity as well. The luminosity produced by HERA during its operation (1994-2000) can be seen in table 1.1

1.7.3 Trigger

The trigger system is designed to select interesting ep physics and reject background events. Common background sources are synchrotron radiation from the electron beam, beam gas interaction, beam halo muons and even muons from cosmic radiation. The ToF system is part of the trigger system and is described in section 1.7.1. The trigger system also differentiates between different classes of physics, the physics

Process	Cross section	Rate
beam gas interactions		50 kHz
cosmic μ in barrel		700 Hz
tagged γp	1.6 μb	25 Hz
$c\bar{c}$ total	1 μb	15 Hz
DIS low Q^2	150 nb	2.2 Hz
DIS high Q^2 (e' in LAr)	1.5 nb	1.4 per min
charged current DIS $p_t > 25$ GeV	50 pb	3 per hour
W production	0.4 pb	0.5 per day

Table 1.2: Cross sections and rates at design luminosity ($L = 1.5 \times 10^{31} \text{ cm}^2\text{s}^{-1}$)

processes of interest cover a wide range of cross sections and rates. Table 1.2 shows typical background and physics cross-sections. Due to a limited available bandwidth for recording data, certain physics classes with high cross sections have to be prescaled (e.g. photoproduction and low Q^2 DIS). The triggers used within this analysis are described in more detail in chapter 5.

The trigger is split into four levels.

The Level 1 system consists of nine different trigger systems each based on the information from one subdetector. The output of each trigger system is fed into a central trigger logic where they are combined into various subtriggers. Each subtrigger is assigned to a given physics event class (physics trigger), to experimental data needed for measuring the efficiency of a given detector (monitor trigger) or to cosmic ray events for calibration (cosmic trigger).

Due to the high bunch crossing rate and to keep dead-time to a minimum, the trigger system is pipe-lined. Pipelining means that the output signals from all sub-detectors are stored until the signal is rejected or passed on to the next level trigger. The input rate into the Level 1 trigger is 10.4 MHz, the output rate is 1 kHz, the rate of each subtrigger can be prescaled in order to maintain the required output rate. The time taken to make a decision is $2.5 \mu\text{s}$ (24 bunch crossings). The fully pipelined Level 1 trigger system runs deadtime free.

The Level 2 trigger examines the event topology in greater detail using both a topological correlator and a neural network approach which use the same information

as on level one but applies more advanced (and time consuming) algorithms to study topological and other complex correlations for the event. The time taken for the level two trigger to make a decision is $20 \mu\text{s}$, and the output rate is 50 Hz

As long as the Level 1 trigger output rate is below 1 kHz and the Level two output rate below 50 Hz then the overall dead time is below 10%.

Events accepted by the Level 2 trigger are sent, in full, to the Level 4 trigger³. The level four trigger uses a simplified version of the full event reconstruction routines to examine the event topologies in order to discriminate between the different classes of events and for background rejection. Accepted events are written to tape and fully reconstructed. The output of the level four system is below 8 Hz. A small fraction (typically 1%) of all rejected events is always kept for monitoring purposes.

³The Level 3 trigger has never been implemented

Chapter 2

ep Physics

2.1 Motivation

This thesis is principle a study of the process of quark fragmentation. That is how the struck quark from the hard interaction forms the hadrons that are observed by experiment. Specifically a comparison will be made between the fragmentation of quarks produced by different processes, from diffractive Deep Inelastic Scattering (DIS), from non-diffractive DIS and from quarks produced in $e^+e^- \rightarrow q\bar{q}$. This comparison will test the concept of quark fragmentation universality, i.e. the fragmentation of a quark from a diffractive process should be the same as that for a quark from a non-diffractive process and for that from a quark created from the vacuum in e^+e^- annihilation.

There is no clear theoretical consensus on how the process of diffractive DIS may be understood within QCD. A variety of different models of diffraction will be tested to see how well they compare to the diffractive data.

The experimental definition of what constitutes a diffractive event is the observation of a large gap in rapidity with no hadronic activity. There exist different definitions of how large and where the rapidity gap should be. Tests of the effect on the results to different definitions of diffractive DIS will also be made.

2.2 Introduction

Deep Inelastic Scattering (DIS) refers to the an interaction in which a scattered lepton gives rise to an exchange boson which is able to resolve the partons that make up the proton. We may consider there to be three distinct and factorisable stages to deep inelastic ep scattering.

1. A hard subprocess characterised by the exchange of a highly virtual boson liberating one or more partons from the proton.
2. Perturbative parton cascade development by $q \rightarrow qg$, $g \rightarrow gg$, and $g \rightarrow q\bar{q}$ splitting.
3. Non-perturbative hadronisation of partons into hadrons.

Stages two and three are generally referred to as fragmentation and are discussed in chapter 4.

DIS is not the only physics process. Indeed photoproduction, which dominates the cross-section at HERA, is also important from a fundamental physics viewpoint.

2.3 DIS Kinematics

The basic process of neutral current deep-inelastic electron proton scattering is

$$e + p \rightarrow e' + H, \tag{2.1}$$

where e and e' are the incoming and outgoing electron respectively, p is the incoming proton and H is the hadronic final state produced by the scattering process.

The cross-section for DIS processes at fixed centre of mass energy (\sqrt{s}) can be summarised by the use of two independent kinematic variables chosen from several possible candidates [10]. Conventionally we use Q^2 , the negative four-momentum transfered squared, and Bjorken- x , which in the naive Quark-Parton Model, is the

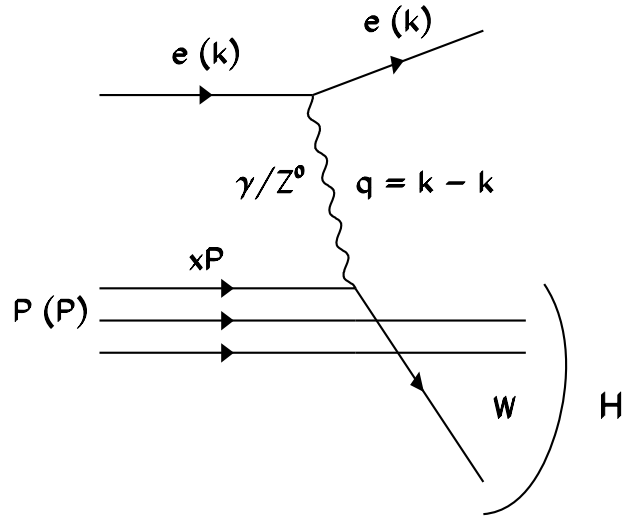


Figure 2.1: Deep Inelastic scattering

fraction of the proton's momentum carried by the struck quark in the proton infinite momentum frame. Other useful kinematic variables are y , the fraction of the energy transferred from the initial electron to the hadronic system in the rest frame of the incoming proton, and W , the invariant mass of the total hadronic system, H .

These kinematic variables are expressed as Lorentz invariant scalar functions of the four-momenta of the incoming and outgoing particles (as defined in figure 2.1) in equations 2.2, 2.3, 2.4, and 2.5 below

$$Q^2 = -q^2 = -(k - k')^2, \quad (2.2)$$

$$x_{bj} = \frac{Q^2}{2P \cdot q} \approx \frac{Q^2}{Q^2 + W^2}, \quad (2.3)$$

$$y = \frac{P \cdot q}{P \cdot k}, \quad (2.4)$$

$$W^2 = (P + q)^2 = sy - Q^2 + m_p^2, \quad (2.5)$$

where m_p is the proton mass, and the total invariant energy squared $s = (P + k)^2 =$

$4E_e E_p$. The relationship between the kinematic variables is often given as

$$Q^2 = sxy. \quad (2.6)$$

With HERA beam energies of 27.5 GeV electrons and 820 GeV protons, s reaches approximately 90,000 GeV². For $Q^2 > 10$ GeV² (the region where perturbative QCD is certainly applicable) values of x down to 10^{-4} can be reached.

The various methods for reconstructing the event kinematics are described in chapter 6.

2.4 DIS Cross Section

This thesis is only concerned with neutral current low- Q^2 DIS processes, therefore contributions from charged current (W^\pm boson exchange) will be ignored. Contributions from Z^0 exchange are suppressed due to the large mass of the Z^0 and can be neglected.

The inclusive differential cross section for inelastic positron-proton scattering may be written as¹

$$\frac{d^2\sigma_{e+p}^{NC}(x, Q^2)}{dx dQ^2} = \frac{4\pi\alpha_{em}^2}{xQ^4} [xy^2 F_1(x, Q^2) + (1-y) F_2(x, Q^2)], \quad (2.7)$$

where the structure of the proton is parameterised by two independent structure functions, $F_1(x, Q^2)$ and $F_2(x, Q^2)$. The two independent structure functions are required since the cross section has two independent contributions from the absorption of transversely (σ_T) and longitudinally (σ_L) polarised virtual photons. $F_1(x, Q^2)$ describes σ_T and $F_2(x, Q^2)$ describes $\sigma_T + \sigma_L$. It is common to redefine the cross section in terms of F_2 and the longitudinal structure function $F_L(x, Q^2)$ where $F_L = F_2 - 2xF_1$

¹A full discussion on DIS and QCD can be found in [11]

²A third structure function $F_3(x, Q^2)$ is introduced for Z^0 and W^\pm exchange.

$$\frac{d^2\sigma_{e+p}^{NC}(x, Q^2)}{dx dQ^2} = \frac{2\pi\alpha_{em}^2}{xQ^4} \left[(1 + (1-y)^2) F_2(x, Q^2) - y^2 F_L(x, Q^2) \right]. \quad (2.8)$$

A useful quantity known as the reduced cross section, σ_r , can be defined from 2.8 by taking the kinematic factors to the left hand side,

$$\frac{xQ^4}{2\pi\alpha_{em}Y_+} \frac{d^2\sigma_{e+p}^{NC}}{dx dQ^2} = \sigma_r = F_2(x, Q^2) - \frac{y^2}{Y_+} F_L(x, Q^2), \quad (2.9)$$

where $Y_+ = 1 + (1-y)^2$. The structure functions cannot be calculated and have to be determined from experimental data. Figure 2.2 [12] shows the reduced cross section as measured by H1 (closed points) together with data from a muon-proton scattering experiment BCDMS [13] (triangles). The fit is a Next to Leading Order (NLO) QCD fit to the H1 and BCDMS cross section data. The dashed curve is the F_2 structure function determined by this fit. At low x , corresponding to large y , σ_r differs from F_2 slightly due to a non-zero F_L .

2.5 Quark Parton Model

The Quark Parton Model (QPM) was first put forward by Feynman [14] and is based on two important assumptions,

- The proton is made up of point-like constituent partons with the momentum of the proton being shared among the partons.
- The short time scale (of order $1/Q$) of the interaction causes the photon to see a frozen state of non-interacting quarks at large Q^2 with the final hadronisation process occurring long after the interaction.

This allows us to consider the interaction as the sum of incoherent scatterings from the point like constituents and to ignore the hadronisation process in the calculation of the cross section. The neutral current cross section in the QPM can be written as,

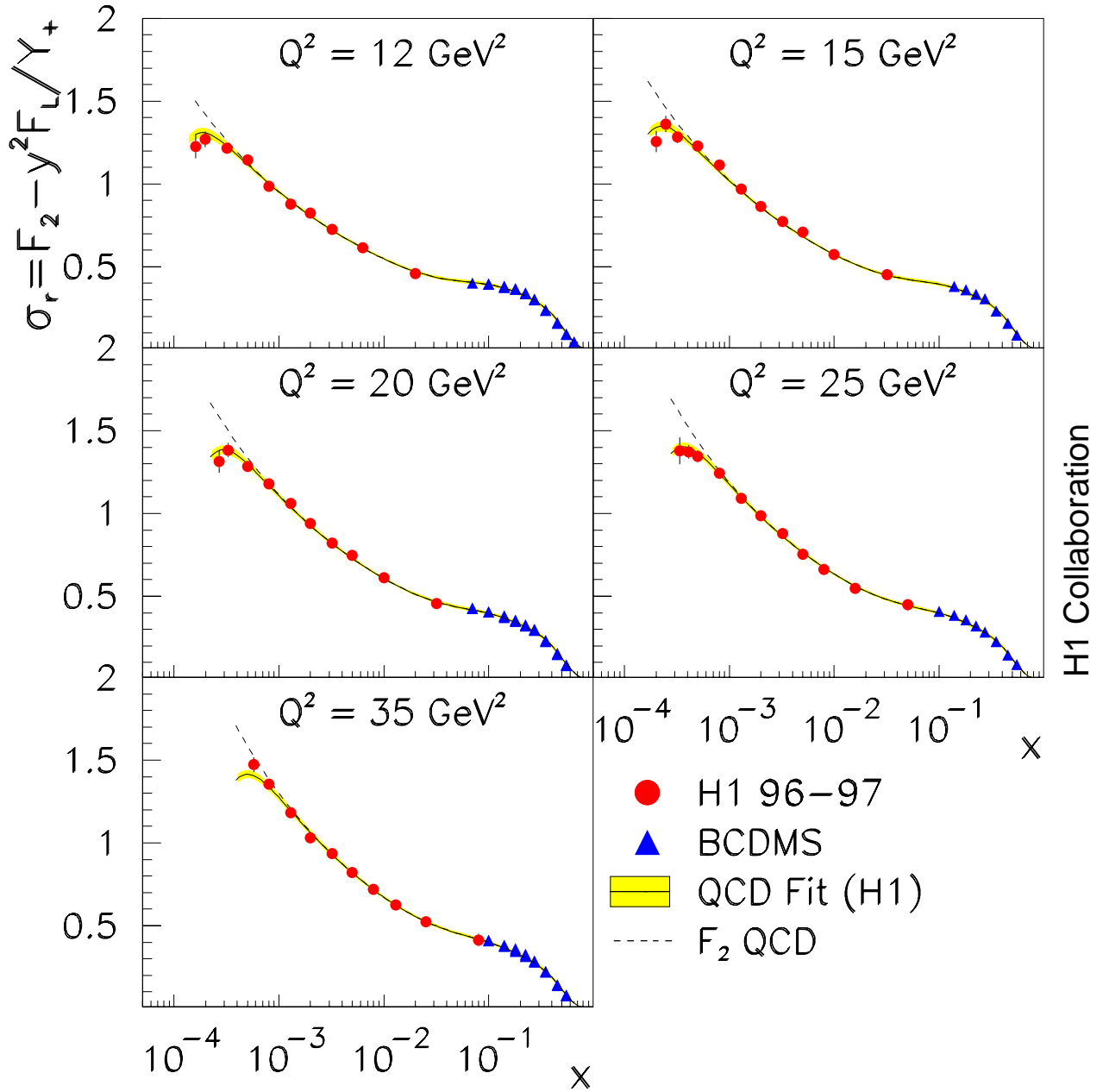


Figure 2.2: Measurement of the reduced DIS scattering cross section. The H1 data are solid points and the fixed target μp data (BCDMS) are triangles. The curves represent the QCD calculation of the cross section (solid) and of the structure function F_2 (dashed) which in most of the x range is identical to the cross section. At lowest x the cross section is lower than F_2 which is attributed to the longitudinal structure function F_L .

$$\frac{d^2 \sigma_{e+p}^{NC}(x, Q^2)}{dx dQ^2} = \frac{2\pi\alpha^2}{Q^2} [Y^+] \sum_i e_i^2 f_i(x), \quad (2.10)$$

where f_i is the probability of finding a quark of flavour i in the proton with a fraction x of its momentum (the parton density function), and the electric charge of the quark is e_i .

Comparing equation 2.7 to 2.10 we see that, ignoring F_L ,

$$\frac{F_2}{x} = 2 \cdot F_1 = \sum_i e_i^2 f_i(x). \quad (2.11)$$

The QPM provides us with a relationship between the structure functions and the parton density functions (PDF(s)). The structure functions do not depend on Q^2 , but only on x , often referred to as Bjorken scaling [15] and is consistent with the initial SLAC measurements [16]. This allows us to interpret F_2 as a measure of how the proton's momentum is distributed amongst its constituent charged partons.

In the naive QPM three massless valence quarks would have an equal 1/3 share of the proton's momentum ($x = 1/3$), but from Figure 2.2 this is clearly not the case. In order to describe the data, QCD corrections to the structure of the proton must be considered in which gluon radiation is allowed. Valence quarks can exchange momentum via gluons and so no longer have to have a 1/3 share of the proton's momentum. Gluons themselves carry a share of the protons momentum and can split into $q\bar{q}$ pairs (sea quarks) resulting in a large number of low momentum partons³.

The shape of the cross section in figure 2.2 can be understood as an initial increase due to the finite number of valence quarks and the further rise at small x due to an increase in the gluon distribution. As Q^2 increases so does resolving power and we find more quarks at small x resulting in a scale-violating Q^2 dependence of the structure functions.

³Additional measurements of F_2 [17] covering a larger range of Q^2 than the SLAC data clearly show that F_2 depends on Q^2 (scaling violation).

In QCD the structure functions are now related to a convolution of (process-independent) parton distribution functions, which are taken from experiment, with the (process-dependent) cross-sections of the ‘hard’ scattering process, which are calculable in perturbative QCD up to next-to-leading order in α_s . Initial parton distributions can-not be calculated from QCD, therefore parametrisations are used of experimental data and evolution equations are used to predict the parton distributions in different regions of phase space.

In perturbative QCD the expansion of F_2 contains terms of the form $(\alpha_s \ln(Q^2/Q_0^2))$ and $(\alpha_s \ln(1/x))$. In the DGLAP evolution scheme $(\alpha_s \ln(1/x))$ terms are neglected, this approximation is valid as long as x is not small. If x is small then $(\alpha_s \ln(1/x))$ terms become large and can not be ignored. The BFKL scheme takes the $(\alpha_s \ln(1/x))$ terms to dominate over $(\alpha_s \ln(Q^2/Q_0^2))$ terms and is valid in the low x region. The CCFM equations try to strike a balance to provide a smooth transition between the two. The perturbative QCD picture breaks down at low Q^2 and the regge model, where the exchange of a single gauge boson (photon) is replaced by that of virtual ‘hadrons’ (called a Regge Trajectory), is used to describe the cross-section. Figure 2.3 illustrates the different regions in Q^2 and x in which each possible scheme is valid.

DGLAP Evolution Equations

The parton density functions are determined from data at a starting scale Q_0^2 . Below this scale (about $Q_0^2 \sim 1 \text{ GeV}^2$) perturbative physics is not applicable. The functions are then evolved to higher Q^2 using the DGLAP (Dokshitzer, Gribov, Lipatov, Altarelli, Parisi) evolution equations [18, 19, 20]. The evolution of the quark and gluon densities is described by a parton splitting process where the probability for parton branchings $q \rightarrow qg$, $g \rightarrow q\bar{q}$, $g \rightarrow gg$ is given by,

$$P_{qg(z)} = \frac{1}{2} [z^2 + (1-z)^2], \quad (2.12)$$

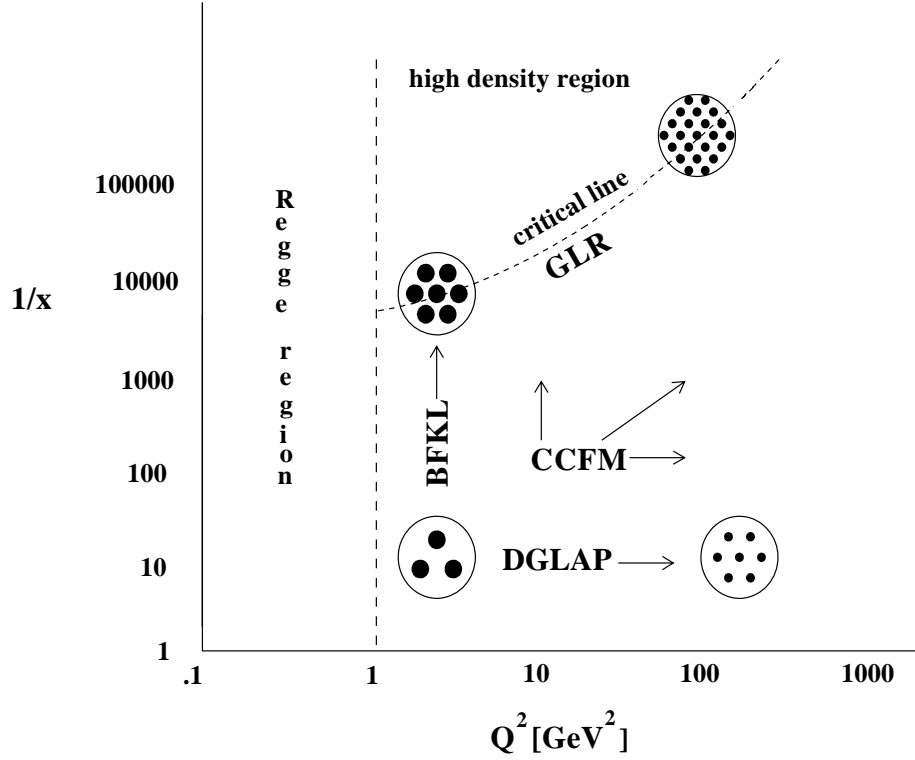


Figure 2.3: Areas of validity for the different evolution schemes.

$$P_{gq(z)} = \frac{4}{3} \left[\frac{1 + (1-z)^2}{z} \right], \quad (2.13)$$

$$P_{gg(z)} = 6 \left[\frac{(1-z)}{z} + z(1-z) + \frac{z}{(1-z)} \right], \quad (2.14)$$

where $P(z)$ is the probability that a parton of four-momentum zp will be produced from a parton of initial momentum p . The emitted partons have a strong ordering in transverse momenta ($k_{T,i}^2$), such that $k_{T,i}^2 \ll k_{T,i+1}^2 \ll \dots \ll Q^2$ and the longitudinal momenta (x_i) satisfy the constraint $x_i > x_{i+1} > \dots > x$.

BFKL Evolution

In the low x region the BFKL (Balitsky, Fadin, Kuraev, Lipatov) equations [21, 22] describe the evolution of quark and gluon distributions in x . In this case the emitted partons transverse momenta ($k_{T,i}^2$) is unordered while the longitudinal momenta (x)

is strongly ordered $x_i \gg x_{i+1} \gg \dots \gg x$, and $\alpha_s(x)$ is fixed.

CCFM Evolution

The CCFM (Catani, Ciafaloni, Fiorani, Marchesini) equations [23, 24] treat both the small and large x regions in a unified way and is based on the coherent radiation of gluons which leads to angular ordering of the gluons. At very small x the angular ordering does not constrain the transverse momenta and gives BFKL-like emission, while at larger x the angular ordering becomes equivalent to an ordering in the gluon transverse momenta and gives DGLAP like behaviour.

Monte-Carlo implementation

Monte-Carlo event generators, which contain a model of the relevant physics processes (e.g. those described in this and the next two chapters), are used to estimate detector acceptance corrections that have to be applied to raw data, in order to extract the ‘true’ physics signal. The basic Monte-Carlo model used in this analysis is the LEPTO [25] generator.

The generation of simulated physics events starts with the calculation of the underlying parton dynamics to a given order in α_s (usually to leading order). Leading order effects include the radiation of a gluon by the quark before and/or after the hard scattering (initial and final state Compton QCD (CQCD) figure 2.4a,b) and the interaction of a gluon via the production of a $q\bar{q}$ pair with the exchange boson (Boson Gluon Fusion (BGF) figure 2.4c). Additional effects such as QED radiation of the electron which changes the electron energy can also be included in the simulation.

These cross sections are then convoluted with parton distributions evolved (normally using DGLAP) from a starting scale of Q_0^2 to give a partonic final state. Fragmentation models (described in Chapter 4) are then used to produce a description at the hadron level.

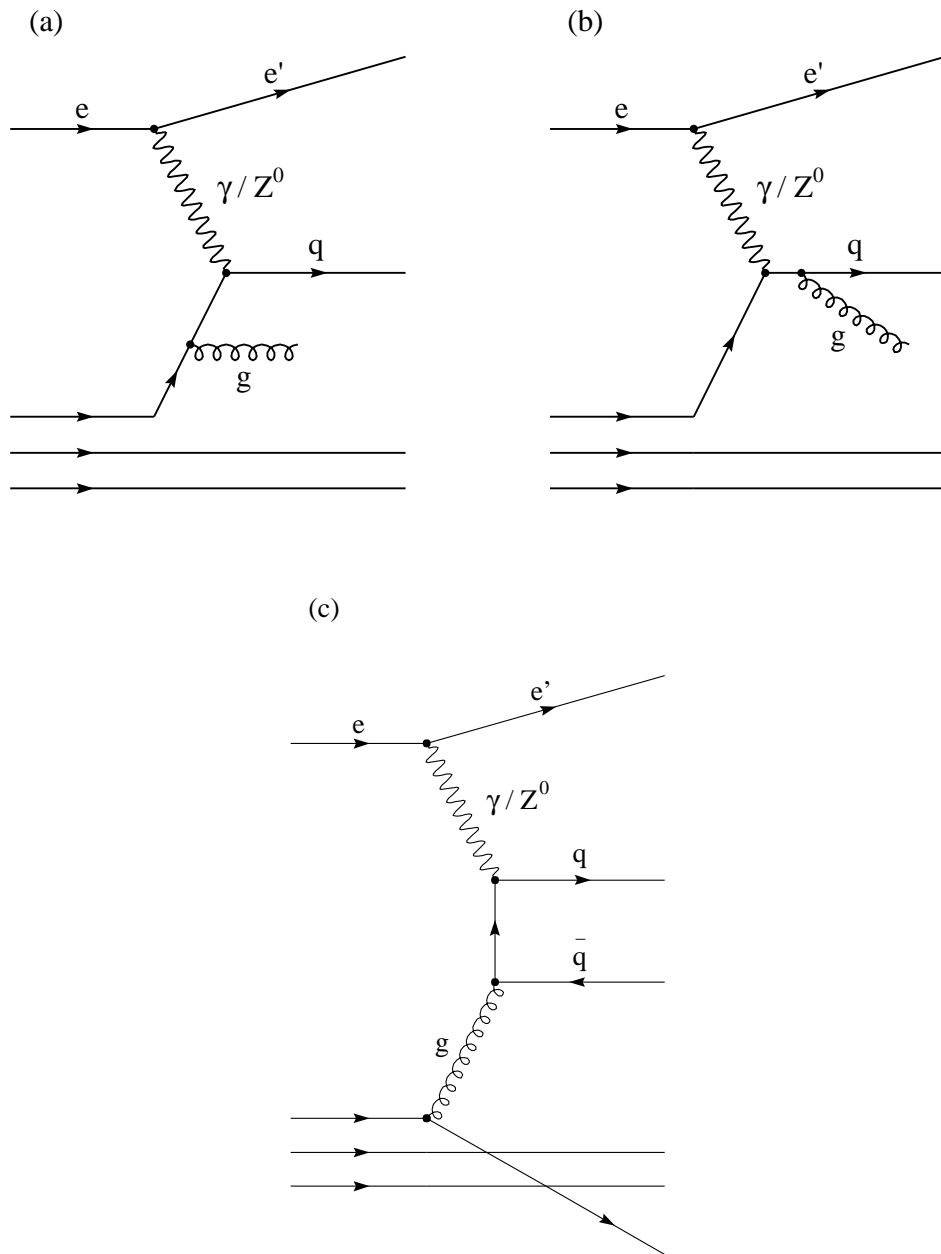


Figure 2.4: (a) Initial and (b) final state Compton QCD and (c) Boson Gluon Fusion.

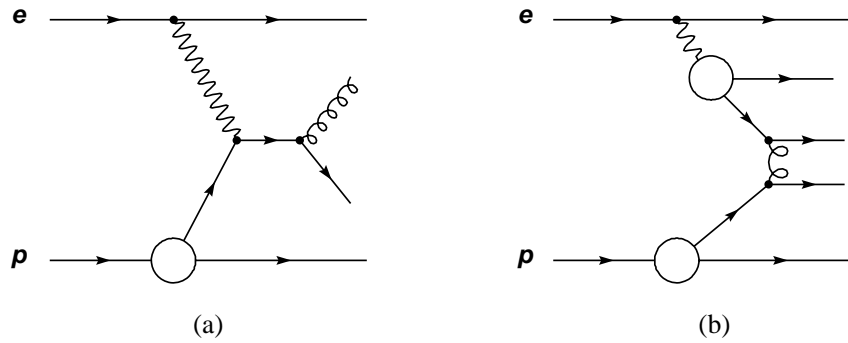


Figure 2.5: (a) Direct and (b) resolved Photoproduction processes.

2.6 Photoproduction

Most of the cross-section at HERA is at $Q^2 \sim 0$ and is called photoproduction. In this case the electron scatters through a small angle and emits a quasi-real photon which then interacts with the proton. The photon can fluctuate into a $q\bar{q}$ pair and as long as the fluctuation time is large compared to the interaction time. The Photon has a probability to interact as a photon directly or first resolve itself into partons which then take part in the interaction. The almost real photons can interact with the proton in three ways

1. Vector Dominance Model (VDM). At low W the photon can fluctuate into a low mass vector meson and interact with the proton.
2. Direct. The photon interacts directly with a quark from the proton, figure 2.5 ($Q^2 > P_t^2$ where P_t is the transverse momentum of the hadronic system).
3. Resolved. A parton from the proton interacts with a quark or gluon from the photon (i.e. the parton probes the photon and resolves its structure). The structure of the photon can be described by a photon structure function F_2^γ figure 2.5b. ($Q^2 < P_t^2$)

Photoproduction events represent a major source of background to DIS studies, since the real scattered lepton goes down the beam pipe and a neutral pion plus tracks

from other sources can be misidentified as the scattered electron.

Chapter 3

Diffraction

3.1 Introduction

There exists a subclass of DIS events of distinctly separate properties, called diffractive events. These events are identified by a gap in rapidity between the outgoing proton system Y , and the observed hadronic system X (figure 3.1). They constitute approximately 10% of the DIS cross section at HERA. These events are evidence of a colourless exchange mechanism between the proton and exchange boson, commonly referred to as pomeron (P) exchange. There is no clear theoretical consensus on how this colourless exchange process may be understood within QCD.

3.2 Diffractive Kinematics

In diffractive DIS additional variables are needed to describe the kinematic as well as the conventional kinematics introduced for DIS events. Using the four-momenta defined in figure 3.1 the kinematics variables are defined as

$$M_Y^2 = Y.Y, \tag{3.1}$$

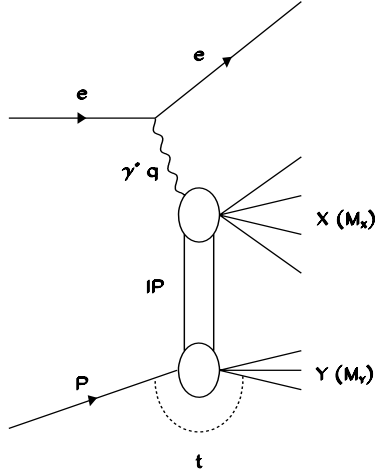


Figure 3.1: Generic diagram for diffractive DIS events. The four vectors of the system X (X), system Y (Y), the exchange photon (q), the incoming proton (P), and the four-momentum transfer at the proton vertex (t).

$$M_X^2 = X \cdot X, \quad (3.2)$$

$$t = (P - Y)^2 = (q - X)^2, \quad (3.3)$$

$$\beta = \frac{Q^2}{2q \cdot (P - Y)} \sim \frac{Q^2}{Q^2 + M_X^2}, \quad (3.4)$$

$$x_P = \frac{q \cdot (P - Y)}{q \cdot P} \sim \frac{Q^2 + M_X^2}{Q^2 + W^2}, \quad (3.5)$$

$$x_P = \frac{x_{bj}}{\beta}, \quad (3.6)$$

Where M_X and M_Y are the invariant masses of the hadronic system X and Y , the

squared momentum transfer at the PY vertex is t , and β and $x_{\mathbb{P}}$ can be interpreted in a QPM-like picture as the momentum fraction of the \mathbb{P} exchange carried by the struck quark and the momentum fraction of the proton carried by the \mathbb{P} , respectively. The approximations made for equations 3.3 and 3.5 are that t and the mass of the proton are small compared to the centre-of-mass energy.

3.3 Diffractive Cross Section

In analogy to the study of the proton structure, a diffractive structure function (F_2^D) can be defined that is a differential of F_2

$$\frac{d^5 \sigma_{ep \rightarrow eXY}}{d\beta dQ^2 dx_{\mathbb{P}} dt dM_Y} = \frac{2\pi\alpha_{em}^2}{\beta Q^4} (Y_+) F_2^{D(5)}(\beta, Q^2, x_{\mathbb{P}}, t, M_Y). \quad (3.7)$$

Since the Y system is not measured directly an integration over t and M_Y has to be made with the diffractive event selections restricting $M_Y < 1.6 \text{ GeV}$ and $t < 1 \text{ GeV}$. The triple-differential cross section is defined as

$$\frac{d^3 \sigma_{ep \rightarrow eXY}}{d\beta dQ^2 dx_{\mathbb{P}}} = \frac{2\pi\alpha_{em}^2}{\beta Q^4} (Y_+) F_2^{D(3)}(\beta, Q^2, x_{\mathbb{P}}). \quad (3.8)$$

The diffractive structure function ($F_2^{D(3)}(\beta, Q^2, x_{\mathbb{P}})$) has been measured by H1 [1] figure 3.2 and ZEUS [26].

3.4 Models of Diffraction

Regge theory and the pomeron

The most popular and successful description of diffractive DIS is based on the QCD-Regge approach. The colourless exchange process is thought to occur via pomeron and reggeon exchange and the diffractive structure function can be parameterised into a pomeron and reggeon contribution (assuming no interference)

H1 1994 Data

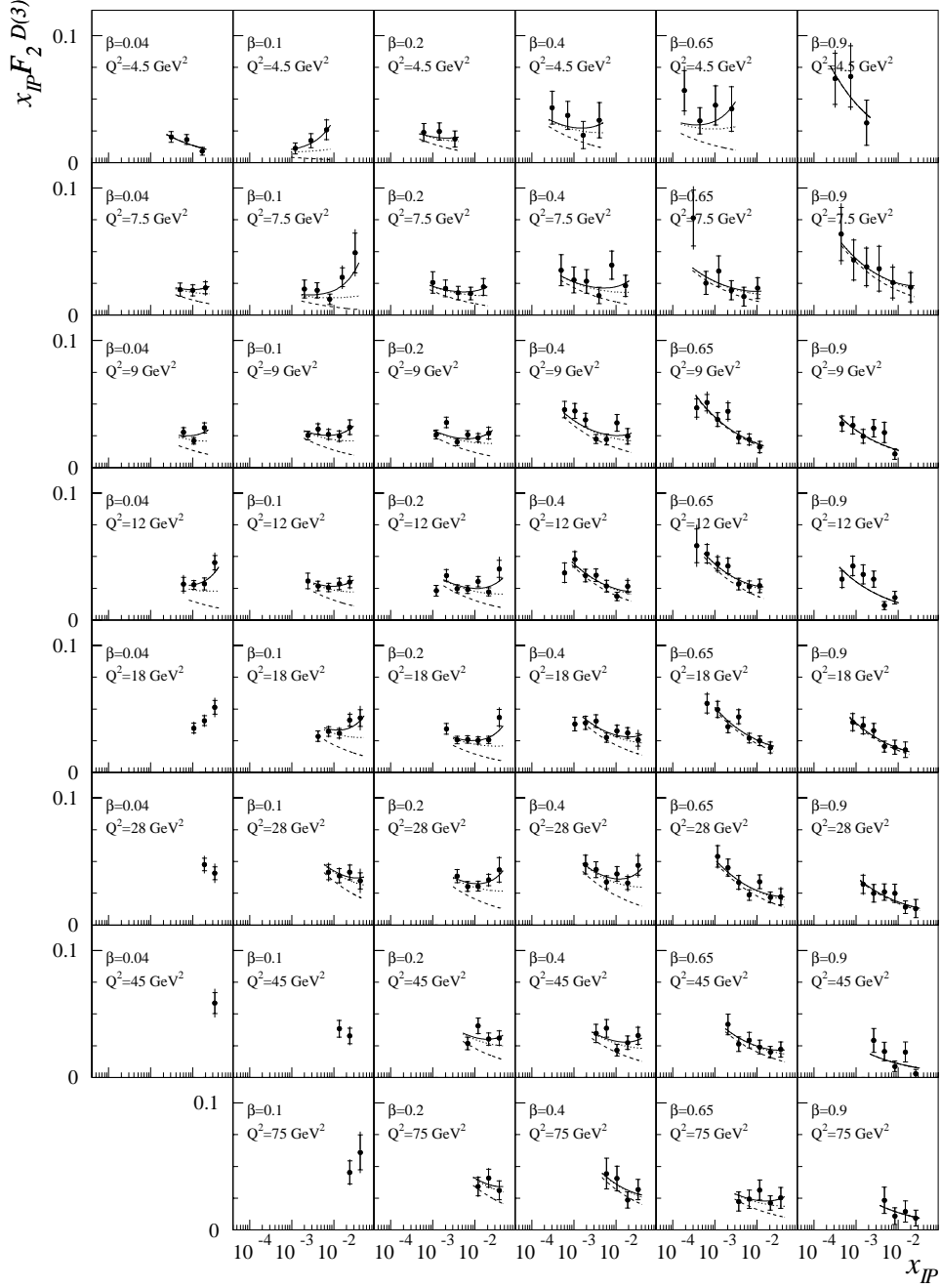


Figure 3.2: The diffractive structure function $F_2^{D(3)}$. The curves show Regge fits, the dashed curve is the contribution from the pomeron only, the dotted curve shows pomeron + interference, the solid curve shows the total pomeron + interference + reggeon contributions.

$$F_2^{D(3)}(\beta, Q^2, x_{\mathbb{P}}) = f_{\mathbb{P}/p}(x_{\mathbb{P}}) F_2^{\mathbb{P}}(\beta, Q^2) + f_{\mathbb{R}/p}(x_{\mathbb{R}}) F_2^{\mathbb{R}}(\beta, Q^2), \quad (3.9)$$

where $F_{2\mathbb{P}}$ and $F_{2\mathbb{R}}$ are the pomeron and reggeon structure functions, $f_{\mathbb{P}/p}(x_{\mathbb{P}})$ is the flux of pomerons in the proton and $f_{\mathbb{R}/p}(x_{\mathbb{R}})$ is the reggeon flux. The non-perturbative flux factors are taken from Regge fits to previous pp and γp data.

The reggeon structure function can be understood in terms of Regge theory as the exchange of mesons from a Regge trajectory. The pomeron structure function can be expressed in terms of quark distributions (as was done for the proton structure function)

$$F_2^{\mathbb{P}}(\beta, Q^2) = \beta \sum_i e_i^2 f_i(x, Q^2) \quad (3.10)$$

where $f_i(x, Q^2)$ is the parton density function for each parton family i , of charge e_i , within the pomeron. The structure of the pomeron is, in this picture, understood in terms of parton dynamics and the evolution of this structure ought to be calculable using perturbative QCD.

Attempts to describe the data (figure 3.2) with only a pomeron exchange fail and the additional reggeon exchange term is needed [1]. When the pomeron structure function is described by parton distributions which evolve according to NLO DGLAP evolution equations, the data requires that approximately 80 – 90 % of the momentum is carried by gluons (the H1 conjecture of a singular gluon distribution).

Dipole Models

Another view of diffraction is as a partonic fluctuation of the photon interacting elastically with the proton. In the rest frame of the proton the photon fluctuates into partons (e.g. $q\bar{q}$ or $q\bar{q}g$) long before the interaction with the proton occurs (figure 3.3 left). The pomeron exchange interaction is modelled in perturbative QCD

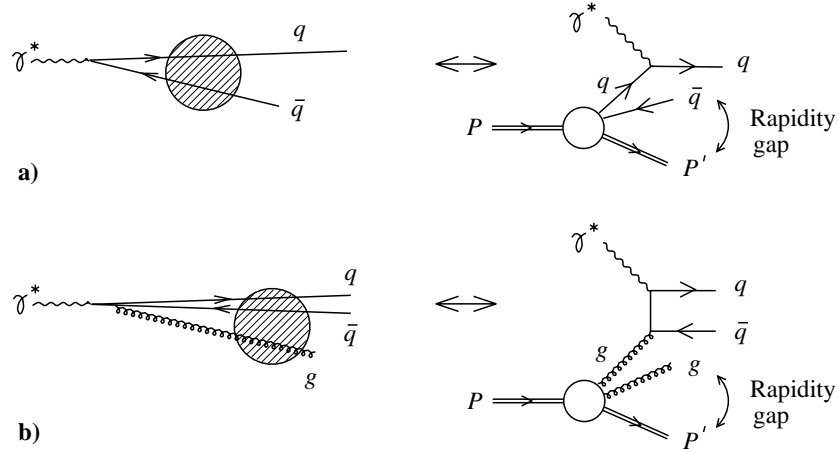


Figure 3.3: Diffractive DIS as modelled by photon fluctuations in the proton rest frame (left) and the PDF picture (right).

by two gluon exchange.

A parameterisation of the diffractive cross section for H1 data has been done by Bartels, Ellis, Kowalski and Wusthoff [27] which contains contributions of $q\bar{q}$ and $q\bar{q}g$ production from transverse polarised photons and $q\bar{q}$ from longitudinal polarised photons and includes both leading and higher twist¹ contributions. It is interesting to note that when the fluctuations of the photon are viewed in a PDF picture an analogy can be drawn with DIS, $q\bar{q}$ production becomes quark scattering with an additional \bar{q} and $q\bar{q}g$ production becomes boson-gluon fusion with an additional gluon (figure 3.3 right).

The main feature of the parameterisation is the decomposition of the β spectrum into three contributions which reside in separate regions with only little overlap: $q\bar{q}g$ production at low β transverse $q\bar{q}$ production at medium β , and longitudinal $q\bar{q}$ production at high β figure 3.4.

Soft Colour Interactions

Soft Colour Interactions (SCI) [28] were originally conceived as an alternative way to model diffractive events. In this model, changes to the colour structure after the hard interaction produce the rapidity gap. At low x most events are due to boson-gluon

¹Higher twist contributions are made only for the transverse $q\bar{q}$ production.

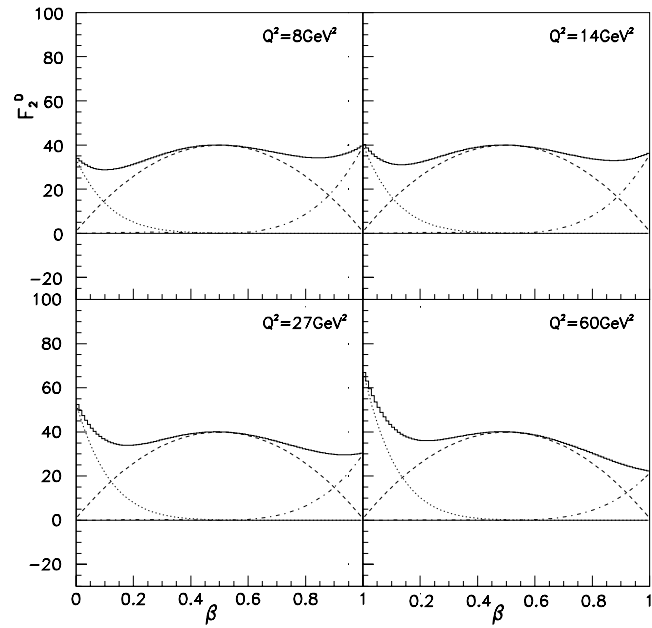


Figure 3.4: The β dependence of $F_2^{D(3)}$ at a constant value of $x_P = 0.001$ in a parameterisation of the H1 $F_2^{D(3)}$ using the BEKW model. The dotted line is the $q\bar{q}g$ contribution, the dashed line is the transverse $q\bar{q}$ contribution, dashed-dotted line is the longitudinal $q\bar{q}$ contribution, the solid line is the full contribution.

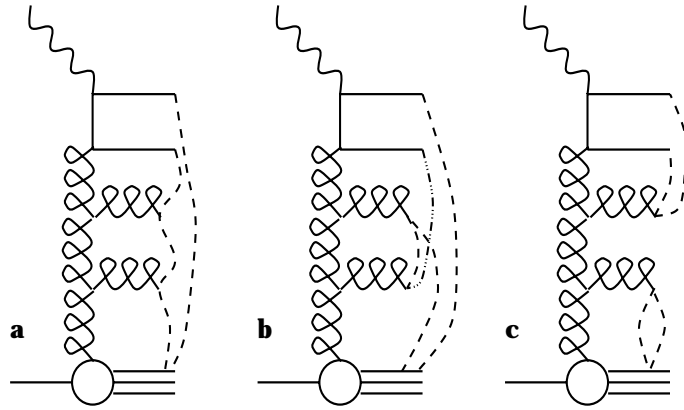


Figure 3.5: Soft Colour Interactions. The dashed lines are soft gluons.

fusion, in the string model two strings would span the BGF diagram (figure 3.5a). The produced quark-antiquark pair then leave the proton and soft gluons are exchanged between them and the proton remnant (figure 3.5b). These gluons have little effect on the momentum but may change the colour configuration in such a way that the $q\bar{q}$ is no longer connected to the proton (figure 3.5c).

Monte-Carlo Models

The RAPGAP generator [29] is used to generate diffractive DIS processes of the type $ep \rightarrow eXp$ and is based on the QCD-Regge model of diffraction. In this model the proton couples to either a pomeron (\mathbb{P}) or a meson (reggeon, \mathbb{R}), which then goes into the hard interaction. The pomeron structure function ($F_2^{\mathbb{P}}(\beta, Q^2)$) is taken from H1 QCD fits [1], while the reggeon structure function ($F_2^{\mathbb{R}}(\beta, Q^2)$) is taken from a GRV parameterisation of the structure function of a pion. The rest of the simulation is similar to that described for LEPTO in Chapter 2.

Soft Colour Interactions are implemented in the LEPTO Monte-Carlo generator. Previous studies have shown that SCI fails to describe the hadronic final state in DIS producing much higher multiplicities in the target region [30] and is not used in this analysis for acceptance corrections.

Chapter 4

Fragmentation

4.1 Introduction

Given factorisation, fragmentation can be studied separately from the hard subprocess, this allows the comparison of fragmentation of the struck quark in DIS with fragmentation of a quark produced from the vacuum in e^+e^- annihilation. The concept that the fragmentation of a quark is independent of the mechanism of its production is called quark universality and is a natural assumption of the standard model of particle physics. Given the same circumstances quark universality means that the fragmentation of a quark from the proton should be the same as that for a quark created from the vacuum in e^+e^- annihilation and for a quark from the pomeron. It is a major thrust of this thesis to examine quark fragmentation universality.

Fragmentation is a strong interaction process and should therefore be described by quantum chromodynamics (QCD). The complete perturbative calculation is only typically available to NLO. Parton cascades based on leading log resummations allow QCD calculations to be extended to multiparton states. A description of hadronisation is not available in perturbative QCD and so a phenomenological model, or the hypothesis of Local Parton Hadron Duality, must be used instead.

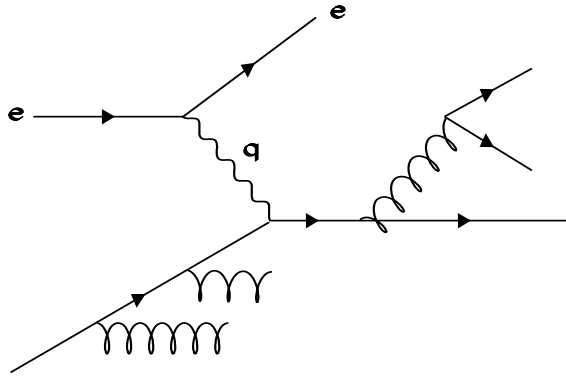


Figure 4.1: Initial state and final state parton showers

4.2 Parton Cascade models

Perturbative QCD calculations are only available up to finite orders because the calculation of matrix elements above leading order (LO) is extremely difficult¹. In order to describe further gluon emission, both before (initial state radiation) and after (final state radiation) the hard scattering, parton cascade models are used.

4.2.1 Parton Showers

The parton shower model (PS) describes the parton cascade process by the splitting of a parent parton into two daughters. The splitting continues with the daughters going on to form parents (figure 4.1). Possible transitions are $q \rightarrow qg$, $g \rightarrow q\bar{q}$, $q \rightarrow gg$. The evolution of the shower is based on leading $\log Q^2$ DGLAP splitting functions [18, 19, 20].

In the initial cascade, at each branching, one parton becomes more space-like ($m^2 < 0$) which will go on to enter the hard interaction while the other becomes more time-like ($m^2 > 0$). After the hard interaction the outgoing quark is off-shell in a time-like manner. The time-like quark's off-shell mass is reduced by further splitting into daughter partons. Any time-like partons from the initial state cascade will also

¹Calculations to next-to-leading order (NLO) have been made but can't yet be interfaced with parton cascade models used in a Monte-Carlo model because of negative weights which such diagrams imply. They are not used in this analysis.

undergo a similar development, until all partons are essentially on-shell.

Gluon coherence which leads to the suppression of soft gluon emission at wide angles has to be imposed on the parton shower model. This is done by restricting successive gluon emissions to decreasingly smaller angles, known as angular-ordering. The transverse momentum, k_t , of emitted partons must also be highly ordered. Every new emission must be smaller than the preceding one (i.e. $k_t(1) \gg k_t(2) \gg k_t(3)$) for the parton shower to provide a good description of the process of parton emission. The cascade is terminated by an infrared cut-off in k_t , below this the perturbative description breaks down and phenomenological models of hadronisation must be used.

The parton shower model of the parton cascade is implemented in the LEPTO Monte-Carlo [25]. In this analysis Monte-Carlo produced with LEPTO using Parton Showers is referred to as MEPS (Matrix Element + Parton Showers).

4.2.2 Colour Dipole Model

Gluon radiation is very similar to classical radiation from an electric dipole. Thus a $q\bar{q}$ pair can be treated as a colour dipole emitting a gluon rather than independent sources of gluons.

The Colour Dipole Model (CDM) [31, 32, 33, 34] works in this way. The $q\bar{q}$ dipole emits one gluon. Two colour dipoles are then formed, one between the quark and the anti-colour charge of the gluon, the other between the antiquark and the colour charge of the gluon. Further gluon emission is possible by the new dipoles. This process is assumed to generalise to an arbitrary number of gluons with each new gluon splitting the dipole into two new dipoles. The emission of a gluon from a dipole is independent of other dipoles but the effect of the radiation pattern from the dipoles, which includes interference effects, in the CDM implies gluon coherence which in other models has to be more crudely modeled. The CDM model also requires the emission of gluons to be ordered in k_t as in the parton shower model but the ordering is not as strong (i.e. $k_t(1) > k_t(2) > k_t(3)$)

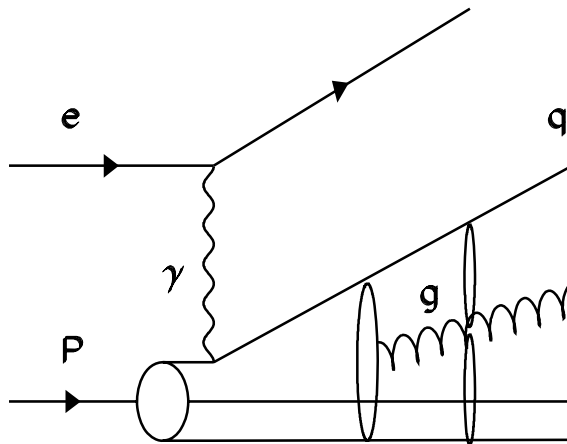


Figure 4.2: The Colour Dipole Model (CDM)

When applied to DIS the CDM does not distinguish between initial and final state gluon emission. Instead all gluon radiation is assumed to be described by radiation from dipoles, this is very similar to what happens to the $q\bar{q}$ created from the vacuum in an e^+e^- annihilation. In e^+e^- the quarks are thought of as point-like but in DIS only the struck quark is point-like whilst the proton remnant must be considered as an extended object (figure 4.2). The radiation of small wavelengths from an extended source is suppressed. When this is implemented in the CDM this results in a reduction in the phase space available for radiation in the target region.

The CDM is implemented in the Ariadne Monte Carlo [35]. It is not a full event generator but replaces parton showers in the LEPTO Monte-Carlo. In this analysis the Monte-Carlo produced with Ariadne is referred to as MEAR (Matrix Element + Ariadne).

4.3 Hadronisation Models

4.3.1 Local Parton-Hadron Duality

The hypothesis of local parton-hadron duality (LPHD) [36, 37] is based on the observation that perturbation theory seems to work down to unexpectedly low scales and claims that at some effective mass cut-off, Q_0 , in an extended cascade the parton may

be replaced by a hadron.

LPHD assumes that the general features (e.g. energy flow and quantum numbers like quark flavour) of the partonic final state can be related to the hadronic spectra by the introduction of an overall normalisation constant determined by experiment. This approach has the advantage that the results of analytical calculations, such as those obtained from the Modified Leading Log Approximation (MLLA) [38], can be compared directly to the measured distributions of hadrons. The model successfully describes many of the gross features of hadronisation.

4.3.2 Independent Fragmentation

The simplest scheme for generating hadron distributions from partons is to assume that each parton fragments independently. The Independent Fragmentation Model, first proposed by Feynman and Field [39], implements this idea.

The fragmenting quark is combined with an antiquark from a $q\bar{q}$ pair created out of the vacuum to give a meson with energy fraction z . The leftover quark with energy fraction $(1 - z)$ fragments in the same way, and so on until the leftover energy falls below some cutoff. The longitudinal momentum distribution is determined by this splitting, the probability for which is controlled by an arbitrary function taken from a parametrisation of data. The transverse momentum distribution is described by a Gaussian of width given by an intrinsic Fermi motion.

Neither energy nor momentum can be conserved simultaneously by a simple version of the model and it does not reproduce particles densities, for these reasons it is not used very often.

4.3.3 String Model

The colour field around quarks is QED-like at short distances due to asymptotic freedom, but at long distances, gluon self-interaction makes field lines attract each other. This produces a linear rise in the interquark potential as the quarks move apart

which ultimately results in confinement.

The Lund string model [40, 41] of the hadronisation phase of fragmentation is based on the dynamics of a relativistic string (or gluonic “flux tube”) stretched between coloured partons.

In the simple case of $e^+e^- \rightarrow q\bar{q}$ the string is stretched from the quark to the anti-quark, with the gluons (produced in the parton cascade phase) acting as kinks on the string. As the quark and antiquark move apart in opposite directions they lose kinetic energy to the string. The string has a uniform energy per unit length, corresponding to the linear interquark potential. If the string gets long enough $q\bar{q}$ pair production can split the string in to two colour singlet string pieces. Further string splitting is possible until we are left with small quark antiquark string segments that are identified with mesons (figure 4.3).

The production of $q\bar{q}$ pairs can be described by a tunnelling probability

$$\exp \left[a - b \left(m_q^2 + p_t^2 \right) \right] \quad (4.1)$$

which produces a Gaussian transverse momentum distribution (from the Fermi motion of the quarks). The model is infrared safe and the string segments are causally disconnected and decay independently of each other.

The picture becomes much more complicated when extended to DIS. At lowest order we can think of the proton remnant as a tightly bound diquark and treat this like an antiquark with a colour string between it and the struck quark. More complicated interactions may require multiple colour strings to be used.

4.3.4 Cluster Model

One problem with the string model is that it has a large number of free parameters and so is not a very predictive model [42]. A simpler model of hadronisation is the cluster model.

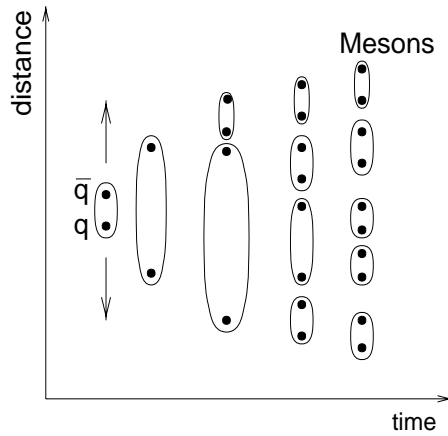


Figure 4.3: The Lund String Hadronisation Model

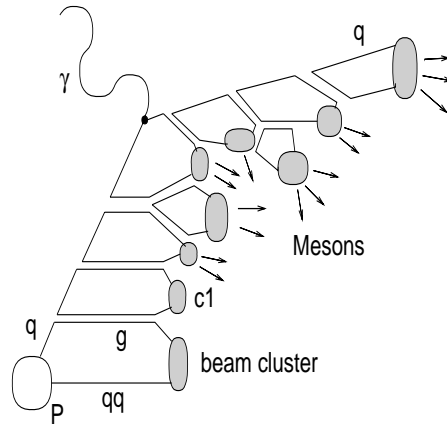


Figure 4.4: The Cluster Model of Hadronisation.

The cluster model, as implemented in the HERWIG Monte-Carlo [43], models the hadronisation process by the formation and decay of colourless clusters. The partons are generated in a perturbative shower and at a given cut-off gluons are formed into light $q\bar{q}$ pairs. Coloured objects that are close to one another are combined into colourless objects which then decay isotropically until they can be identified with known resonances, then decay according to known branching ratios and available phase space (figure 4.4).

The cluster model gives a fair description of data but has problems in several areas. Attempts to solve these problems involve adding extra adjustable parameters which produce a more string-like model.

Chapter 5

Data Selection

5.1 Introduction

The event and track selection used in this analysis are detailed, together with quality control checks on the Monte-Carlo simulation used for detector corrections.

5.2 Physics Event Selection

The data used in this analysis is a selection of neutral current low Q^2 events taken by the H1 detector in 1996. The majority of data recorded is due to beam-gas, cosmic-ray and photoproduction events. In order to obtain a pure sample of DIS events, with good acceptance of the hadronic final state and the scattered electron, and also to minimise QED radiative corrections, the following event selection is applied to the data.

5.2.1 Trigger

A cocktail of ORd triggers is used to provide an unbiased selection of DIS events. The triggers used for the selection of the 1996 low Q^2 data are based on the identification of a scattered electron candidate in the SpaCal. In order to reduce background rates the

SpaCal is split into regions where different thresholds on the energy can be applied. This is useful in the inner region where hot-spots of background activity, generated by synchrotron radiation, can develop which would lead to large background rates in the triggers. Most triggers used also have additional requirements based on time of flight information (see chapter 1). See section 5.2.5 for a study of the trigger bias.

5.2.2 General DIS selection

From the triggered DIS events the following set of cuts are applied to produce a data sample suitable for physics analysis.

The virtuality of the photon is required to be in the range $12 < Q^2 < 100 \text{ GeV}^2$. This means that the scattered electron is well within the acceptance of the SpaCal¹.

The events are explicitly selected to have an identified scattered positron with an energy $E_e > 14 \text{ GeV}$. At high Q^2 this helps to remove photoproduction events where a low energy pion from the hadronic final state can be misidentified as the scattered electron.

The polar angle of a hypothetical scattered QPM quark (θ_q), calculated using four momentum conservation with the scattered lepton and assuming the quark is massless is

$$\cos \theta_q = 1 - \frac{2yE_e}{yE_e + \left(\frac{Q^2(1-y)}{4E_e y}\right)}, \quad (5.1)$$

and is required to be in the range $10^\circ < \theta_q < 150^\circ$. This means that the majority of the hadronic system is inside the acceptance of the H1 track detectors and thus minimises corrections at the cost of removing $\sim 25\%$ of events. Alternatively the hadronic activity could be measured directly via the calorimetry although this raises questions of possible biasing the event selection and introduces problems of applying this cut at the generated Monte-Carlo level or for theoretical calculations.

¹Unless otherwise stated the electron only method is used to reconstruct the event kinematics (see chapter 6).

To reject beam associated background, we demand that there be no veto from the time of flight system and that an event vertex be reconstructed within 35 cm of the nominal vertex position. The dimensionless inelasticity variable, $y = Q^2/xs$, is required to be in the range $0.055 < y < 0.6$. The sum $\sum_i (E^i - p_z^i)$ over all calorimeter energy deposits, which should approximately equal twice the electron energy (55 GeV) for DIS, is required to be in the range 35 GeV to 70 GeV. Together these conditions ensure that contamination from mis-identified photoproduction events is below the 1% level [44] and reduce corrections for QED radiative effects which are large at $y \sim 0$ and $y \sim 1$.

There is a problem arising from the remaining initial state QED radiation leading to an incorrect measurement of Q^2 which in turn affects the boost to the Breit frame. The miscalculation of the boost results in a wrongly determined Breit frame axis. In most cases this leads to a depleted (or even empty) current region where the scattered quark fragments are expected. To cut out events which have a sizable QED radiative corrections, the $0.055 < y < 0.6$ selection is reimposed using hadronic system variables calculated with the Jaquet Blondel method.

In figure 5.1 the data is plotted on the (x, Q^2) plane, also shown are the effect of several important kinematic cuts. The electron energy and upper y cuts ($E_e > 14$ and $y < 0.6$) have no effect on the low Q^2 event selection but are included to reinforce the fact that the events lie with these cuts, and, for historical reasons since non-diffractive analyses have extended to high Q^2 where these cuts are required.

5.2.3 Non-Diffractive (inclusive) DIS

Previous DIS studies included a further cut to remove events with little forward energy flow by requiring that the total summed energy (*egap*) deposited in the polar region $4^\circ < \theta < 15^\circ$ to be greater than 0.5 GeV. The discovery of diffractive events with a hard scale was a surprise and early DIS Monte-Carlos were incapable of describing

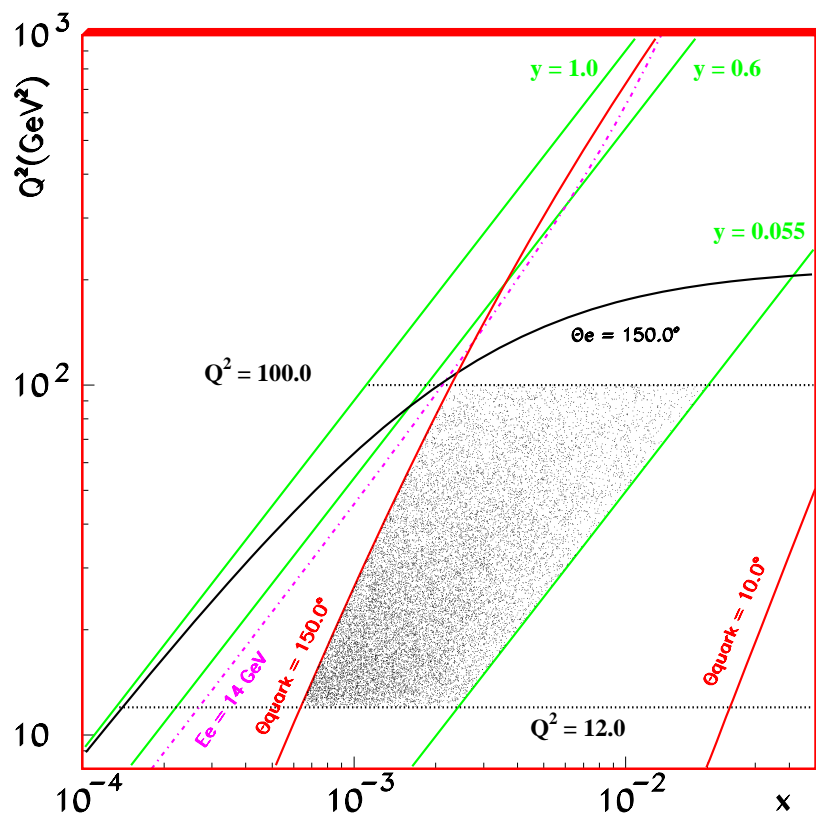


Figure 5.1: The $Q^2 - x$ plane showing the kinematic cuts.

them. The cut was designed to remove these events and completes the DIS² event selection.

5.2.4 Diffractive DIS

The DIFFMX event selection is made up of events that pass the general event selection but fail the non-diffractive DIS event selection (i.e., $egap < 0.5$ GeV). The “MX” in DIFFMX indicates that this selection works by restricting the mass of the observed hadronic system X .

The DIFFMY event selection requires an absence of hadronic activity in the very forward region and is based on the standard H1 definition of diffraction [1]. There must be no signal above noise levels in the forward muon detector, FMD ($N_{FMD} < 2$)³ and proton remnant tagger, PRT ($PRT = 0$) detectors. The most forward hadronic energy cluster with energy $E > 400$ MeV must be at pseudo-rapidity $\eta < 3.3$. Non-diffractive contributions are suppressed by requiring $x_P < 0.05$. Low mass vector meson production are excluded by requiring $3.0 < M_X < 36$ GeV. These cuts correspond to the approximate restrictions $M_Y \leq 1.6$ GeV and $|t| \leq 1$ GeV for reconstructed events. The “MY” in DIFFMY indicates that this selection works by (indirectly) restricting the mass of the outgoing baryonic system Y .

A total of 108 000 events pass the general DIS event selection. Out of this, 100 000 are DIS, and 8 000 are DIFFMX and the DIFFMY sample is made up of 10 000 events (figure 5.2). Only thirty percent of DIFFMY events are also selected by the DIFFMX cut. This means that the $egap$ cut fails to remove a large fraction of events standardly classed as diffractive from the DIS sample (mainly large M_X events). An important extension to this analysis is to study what effect these events have on the robustness of the published DIS results. To do this a second DIS selection (DIS2) is defined as those events that fail the DIFFMY cut. The DIS2 sample is made up of 98,000

²All event selections contain deep inelastic scattering events, but for convenience and emphasis I refer to this non-diffractive selection as DIS.

³About 25% of random events have one “hit” in the FMD essentially caused by random noise[45]. To allow for this the number of hits in the FMD has to be less than two.

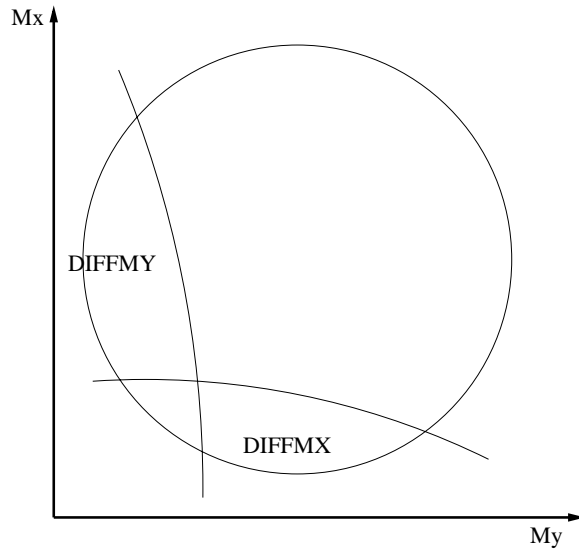


Figure 5.2: A schematic representation of where events for the different selections are in $M_X - M_Y$ phase space. The circle represents the general selected phase space. This is then divided into different regions by the DIFFMX and DIFFMY selections which place different restrictions on M_X and M_Y .

events.

5.2.5 Tests for Trigger Bias

The simplest of the OR'd triggers (called S0) requires just a cluster of deposited energy above threshold in coincidence with the Time of Flight (ToF) window. Due to instabilities in the trigger and off line energy re-calibration, the trigger energy threshold and timing could in principle bias the event selection.

To test for any bias in the S0 trigger a sample of events that has no pre-selection is required. The random trigger provides such a sample. The random trigger sample of events is obtained by accepting a fraction of all events, chosen at random, irrespective of whether they would pass any trigger selection. After applying the event selection the random trigger events can be compared to the S0 triggered events. In Figure 5.3(a) the efficiency of S0 triggered events compared to random triggered events is shown as a function of Q . The efficiency of S0 is found to be high ($\sim 97\%$) and independent of Q .

The S0 trigger fires at a high rate but due to bandwidth limitations the number

of events that can be written to tape is limited and the trigger has to be “prescaled” to reduce the rate at which it fires⁴. In order to recover these events an OR of 14 triggers (including S0) is used. Most of the other triggers (S1 to S13) used have additional requirements based on the z vertex position, event multiplicity, or the energy in the LAr and are also prescaled. Since this analysis is a track based study of the hadronic final state it is important to show that these triggers do not bias the event multiplicity of the physics event selections. Figure 5.3(b,c) shows the firing ratio of triggers S1→S13 to S0 as a function of the multiplicity of tracks in the current region of the Breit frame. Although the current region of the Breit only covers a small region of phase space it does so in the central region of the detector where most of the additional triggers are located. Any bias in these triggers should be evident in this distribution. No bias can be seen in the DIS or DIFFMY event selections [46].

5.3 Track Selection

In addition to the event selection cuts are also applied to the tracks accepted for analysis to protect against badly reconstructed tracks. The H1 tracking systems has been described in chapter 1. Standard H1 track selection is based upon whether the track is detected in the central tracker, forward tracker, or both.

5.3.1 Central Track Selection

- The polar angle of the track θ_{Track} is required to be in the range $20^\circ < \theta_{Track} < 160^\circ$
- Transverse momentum $p_t > 0.15 \text{ GeV}$.
- The track must be associated with a vertex such that the distance of closest approach (DCA) of the track in the $x - y$ plane to the z -axis is less than

⁴Prescaling means that a randomly chosen but fixed percentage of events (depending on the prescale chosen) are thrown away.

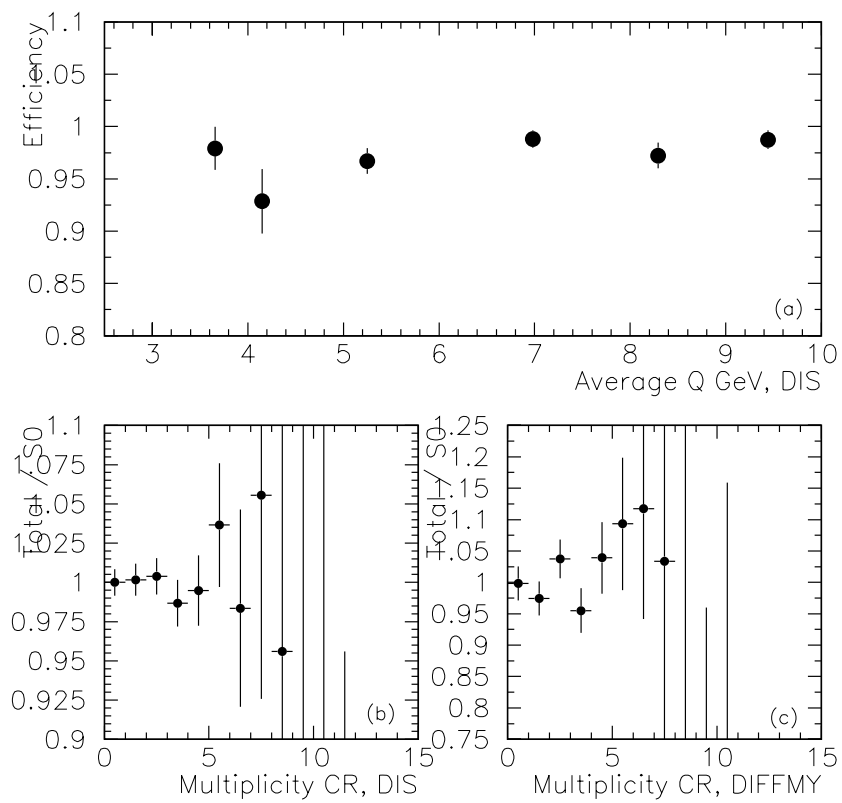


Figure 5.3: (a) The efficiency of S0 as a function of Q . The ratio of the ORed triggers S1->S13 (Total) over S0 for the multiplicity of tracks in the current region of the Breit frame for (b) DIS and (c) DIFFMY event selections.

2.0 cm.

- The radial distance from the beam line to the start of the track (R_0) must be less than 50 cm.
- Tracks with $\theta_{\text{Track}} < 150^\circ$ must be longer than 10 cm and tracks with $\theta_{\text{Track}} > 150^\circ$ must be longer than 5 cm. The last two requirements avoid “split” tracks (where two sections of the same track are unable to be connected in the reconstruction) from entering the analysis.

5.3.2 Forward Track Selection

- $6^\circ < \theta_{\text{Track}} < 25^\circ$
- $p > 0.5$ GeV. This cut suppresses products from low momentum scattering in the end wall CJC, which are badly modelled in Monte-Carlo simulation.
- Track curvature is used to calculate track momentum. Energetic particles produce a straight track, so the momentum error, $\delta p/p$, is large. We require, $\delta p/p \leq 1.0$ and correct for the remaining poorly measured tracks.
- R_0 must be less than 10.0 cm.
- A fit to the vertex has to have a $\chi^2_{\text{vertex fit}}/\text{NDF}$ less than 10.0.
- To suppress tracks that are associated with wrong hits in the forward tracker, a fit is applied to each track with $\chi^2_{\text{track fit}}/\text{NDF} \leq 25.0$.

5.3.3 Combined Tracks

A selection is applied to tracks that traverse both trackers

- $DCA < 5.0$ cm
- $\chi^2_{\text{track fit}}/\text{NDF} \leq 50.0$

- $p_t > 0.15$ GeV
- $\delta p/p \leq 1.0$
- $R_0 < 50.0$ cm.

5.4 Data Correction

Monte-Carlo is used to correct data for detector acceptance and inefficiencies and for QED radiative effects. All data will be corrected back to the true phase space defined as; $12 < Q^2 < 100$ GeV, $0.05 < y < 0.6$, $10^\circ < \theta_q < 150^\circ$, additionally for the DIS selection; $egap > 0.5$ GeV, for the DIFFMX selection; $egap < 0.5$ GeV, and for the DIFFMY selection; $3 < M_X < 36$, $M_Y < 1.6$ GeV, $|t| < 1.0$ GeV, $x_P < 0.05$.

The data is corrected in this analysis by a bin-by-bin method. The acceptance correction factors, CF , for each bin of any given distribution are given by

$$CF_i = \frac{n_i^{gen}}{n_i^{rec}}, \quad (5.2)$$

where n_i^{gen} is the number of generated events in the i^{th} bin after the generator event selection and n_i^{rec} is the number of reconstructed events after the reconstructed event selection.

QED radiation will change the four vector of the incoming electron. This can cause problems in the reconstruction of the event kinematics which in turn affects the boost to the Breit frame. Radiative corrections can be included into the correction factor by turning off radiative effects for the generated events ($n_i^{gen,norad}$) so the expression for the CF is modified to

$$CF_i = \frac{n_i^{gen,norad}}{n_i^{rec,rad}}, \quad (5.3)$$

In order for the correction factors to be accurate the reconstructed distribution from Monte-Carlo must give a fair description of the raw data.

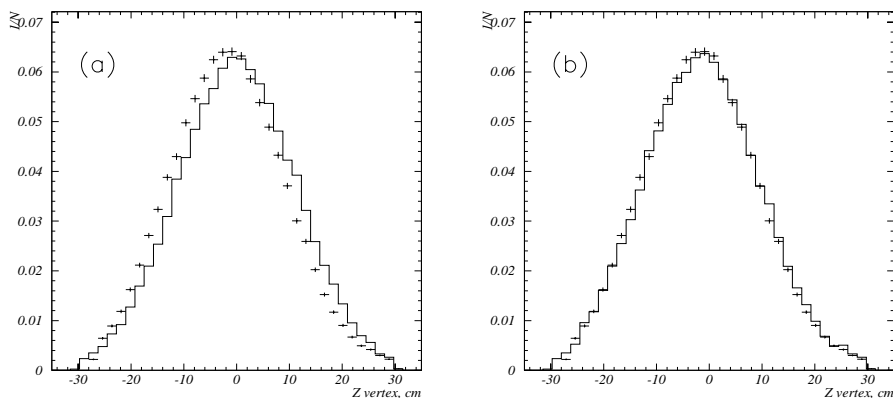


Figure 5.4: The Z vertex position for MEAR Monte-Carlo (histogram) vs Data (points) (a) before and (b) after correction.

5.5 Comparison with Monte-Carlo

5.5.1 DIS and MEAR

In this section, reconstructed MEAR Monte-Carlo distributions are compared to raw DIS data. In general MEAR gives a good description of the data but two problem distributions were evident, the z vertex position (figure 5.4a) and the scattered electron energy (figure 5.5a). All distributions are normalised by the number of events (N).

ZVTX

The $ZVTX$ of the Monte-Carlo was found to be shifted in the positive z direction compared to the data. To improve the description each event of the Monte-Carlo is reweighted using a simple linear function between ± 25 cm of the form

$$new\ weight = old\ weight * (ZVTX * (0.013) + 1). \quad (5.4)$$

It was found that this worked for both MEAR (figure 5.4b) and RAPGAP Monte-Carlos, as expected from what is a simulation fault.

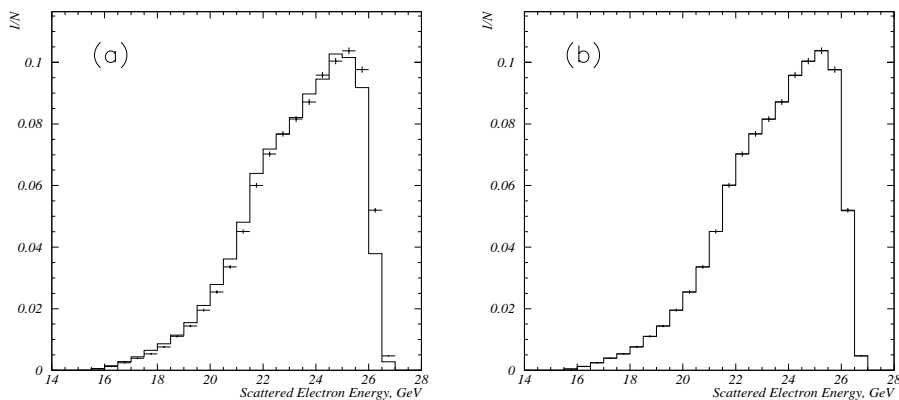


Figure 5.5: Scattered Electron Energy for MEAR Monte-Carlo (histogram) vs Data (points) (a) before reweighting and (b) after reweighting.

Electron energy

The scattered electron energy is reweighted event by event by using the exact bin ratio between the data and Monte-Carlo, hence the reweighted Monte-Carlos scattered electron energy distribution is exactly the same as the data (figure 5.5b).

General

Figure 5.6 shows some important event and track quantities after both the z -vertex and scattered electron energy have been altered. They show that the MEAR Monte-Carlo gives a good description of the DIS event selection.

5.5.2 DIFFMY and MEAR

The Ariadne parton cascade model used in the MEAR Monte-Carlo includes a model which attempts to produce large rapidity gap events. For each event it considers the probability that the struck quark is part of a pomeron, in which case the $x_{\mathbb{P}}$ and t are generated according to inbuilt structure functions for the pomeron. The result is a dipole between the struck quark and pomeron remnant of mass M_X and a rapidity gap between the pomeron and the proton. Unfortunately this model fails to describe even the basic diffractive variables, and worse still the data has $\sim 25\%$ more tracks

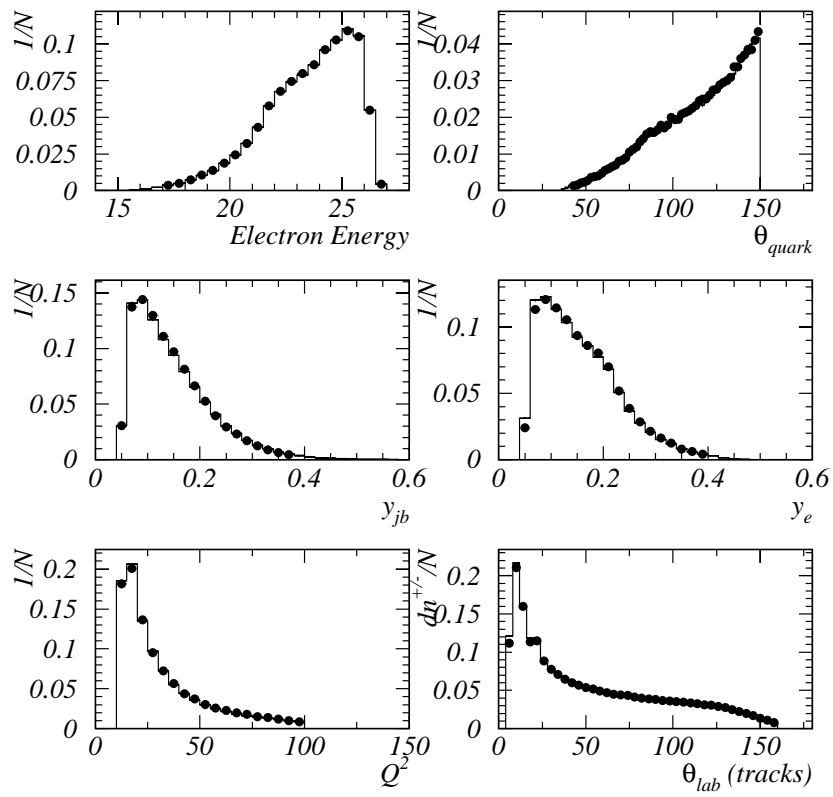


Figure 5.6: MEAR vs data for some event and track distributions for DIS events.

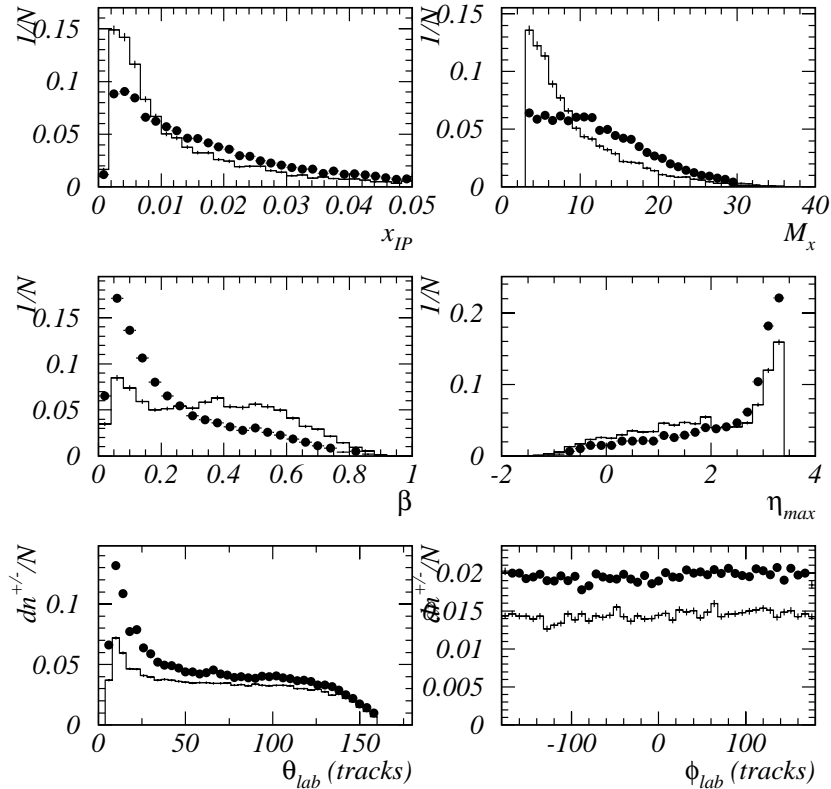


Figure 5.7: A comparison of the MEAR Monte-Carlo with data for the DIFFMY event selection.

than the MEAR Monte-Carlo has been able to generate (figure 5.7).

5.5.3 DIFFMY and RAPGAP

Comparisons between data and RAPGAP Monte-Carlo showed up several discrepancies. The z vertex showed similar simulation problems as with the MEAR Monte-Carlo and were altered using the same linear function. Although showing similar symptoms, the scattered electron energy distribution has a better description than was the case for MEAR and has not been reweighted.

A detailed study of the forward detectors was carried out in [45] and shows that while the forward muon detector is accurately described in the Monte-Carlo simulation, the proton remnant tagger (PRT) is not. The simulation of the PRT in the

Monte-Carlo is too efficient at detecting the proton remnant.

By studying the PRT in events where there is activity in the forward region (by adding the additional cuts $\eta_{max} > 3.3$ and $N_{FMD} > 1$ to the DIS event selection) and taking the ratio of the hit response of the data and the Monte-Carlo we obtain a correction factor for each of the seven scintillators which are applied to the PRT when making the DIFFMY event selection. It was found necessary to apply an additional overall correction factor to the PRT. This was attributed to problems with either the simulation of the shower in the material surrounding the PRT or to too large primary remnant multiplicities, resulting in a higher number of multiple hits in the Monte-Carlos PRT. When compared with data this could not be corrected for by recalibrating each scintillator individually.

The suggested correction factors in [45] were found to be similar to those used in this analysis. The overall effect of this reweighting is to add $\sim 1\%$ more events to the DIFFMY sample.

M_x problem (\mathcal{P} and \mathcal{R} mix)

One *MAJOR* discrepancy, undoubtedly related to physics, was seen for the diffractive kinematic variables $x_{\mathcal{P}}$, M_x , β and η_{max} (figure 5.8). The default RAPGAP is unable to reproduce the low M_x and low $x_{\mathcal{P}}$ behaviour of the data. A solution was to reduce the relative reggeon (\mathcal{R}) contribution by 50% (figure 5.9). This was later found to be required for other analyses [47] and might be related to an incorrect parameterisation of the \mathcal{R} content of the data in the Monte-Carlo [48].

General

In general the shapes of the various quantities of the DIFFMY data selection are reproduced by the RAPGAP Monte-Carlo (figure 5.10), but not as well as the MEAR reproduces the DIS data selection. Most obvious is the deficit of tracks in the RAPGAP Monte-Carlo in the forward region. A known deficiency in the RAPGAP Monte-

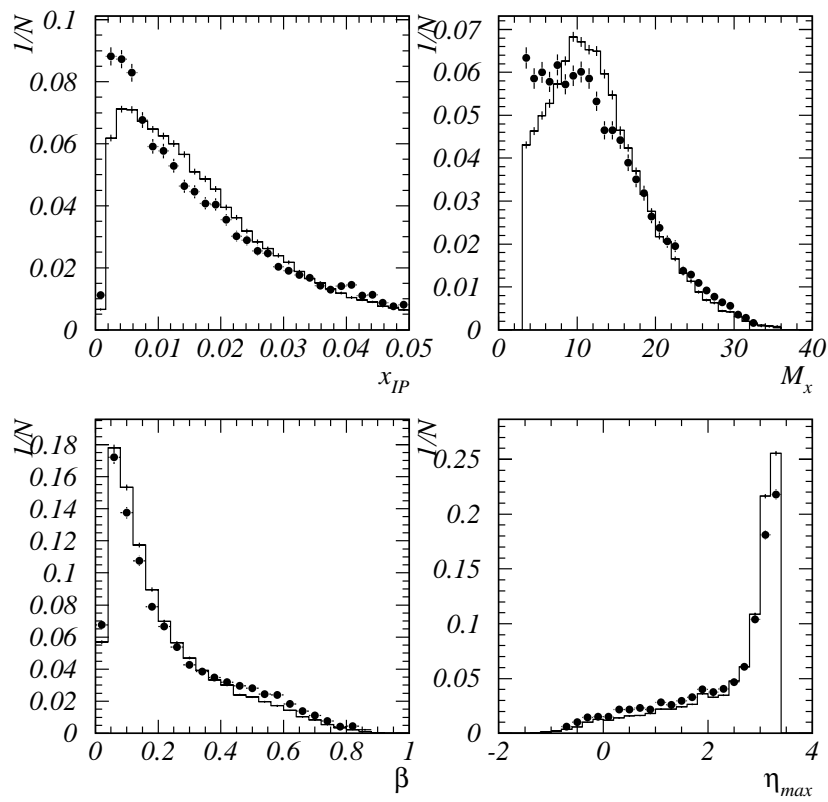


Figure 5.8: The diffractive variables M_x , x_{IP} , β and η_{max} before altering the \mathcal{R} contribution for the DIFFMY selection.

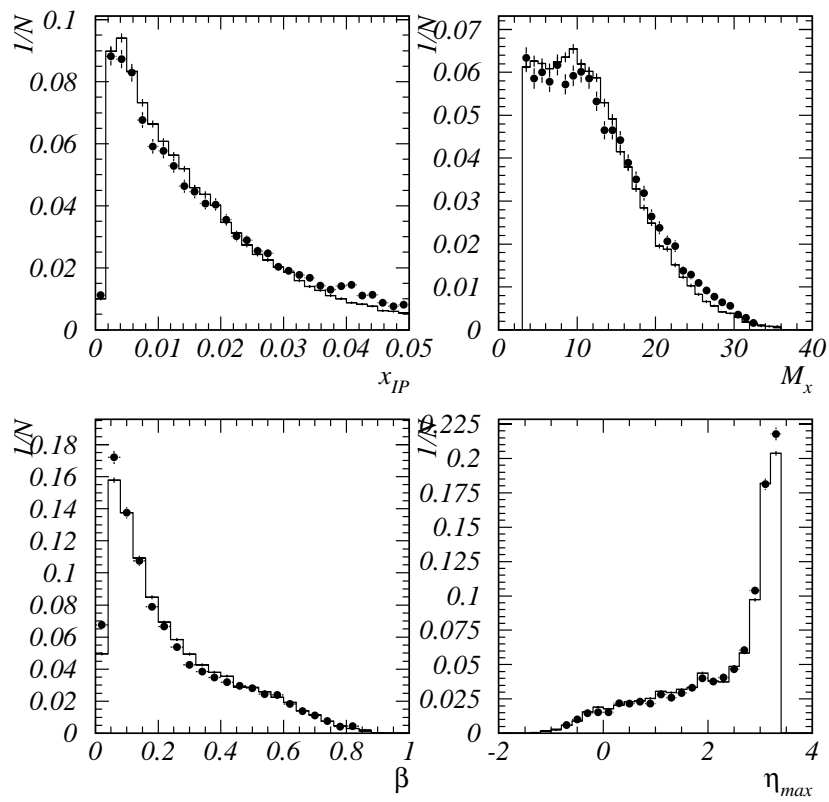


Figure 5.9: The diffractive variables M_X , x_{IP} , β and η_{max} after altering the \mathbb{R} contribution for the DIFFMY selection.

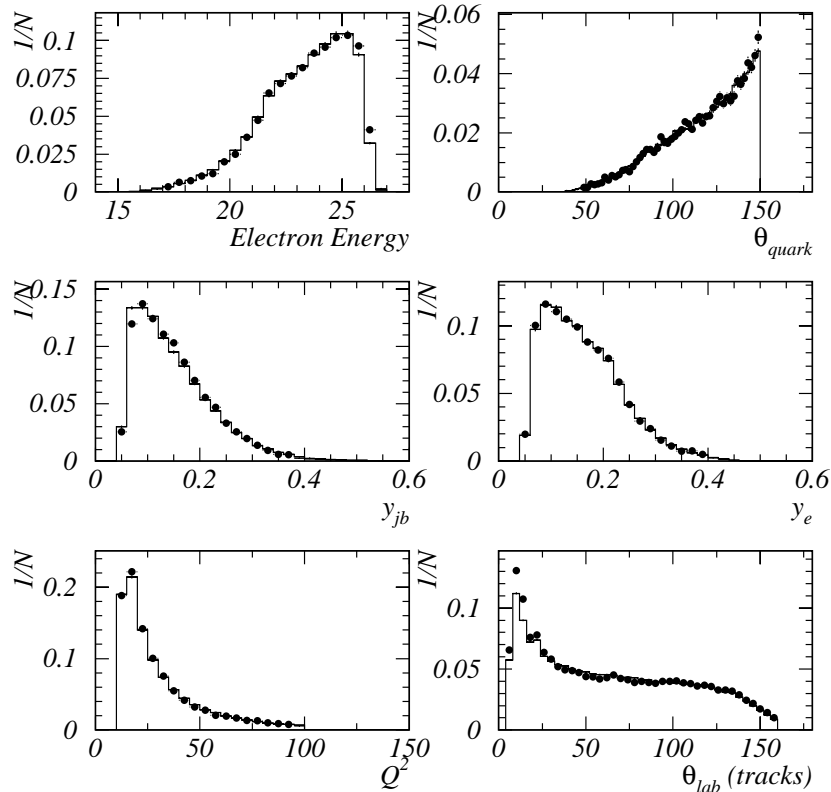


Figure 5.10: RAPGAP vs data event and track distributions for the DIFFMY event selection.

Carlo is that it does not include proton dissociation. Also the version used in this analysis does not include non-diffractive DIS events. Both of these processes may contribute to additional tracks in the forward region which may describe the deficit. Despite these problems it is still acceptable to use this Monte-Carlo for detector effect corrections for the DIFFMY event selection.

5.5.4 DIFFMX and RAPGAP

The description of the DIFFMX event selection by the RAPGAP Monte-Carlo is slightly worse than for the DIFFMY event selection although shapes and normalisation of most distributions are satisfactory (figure 5.11 and 5.12). Due to the restrictive nature of the egap cut in the DIFFMX selection almost all \mathcal{R} events are removed

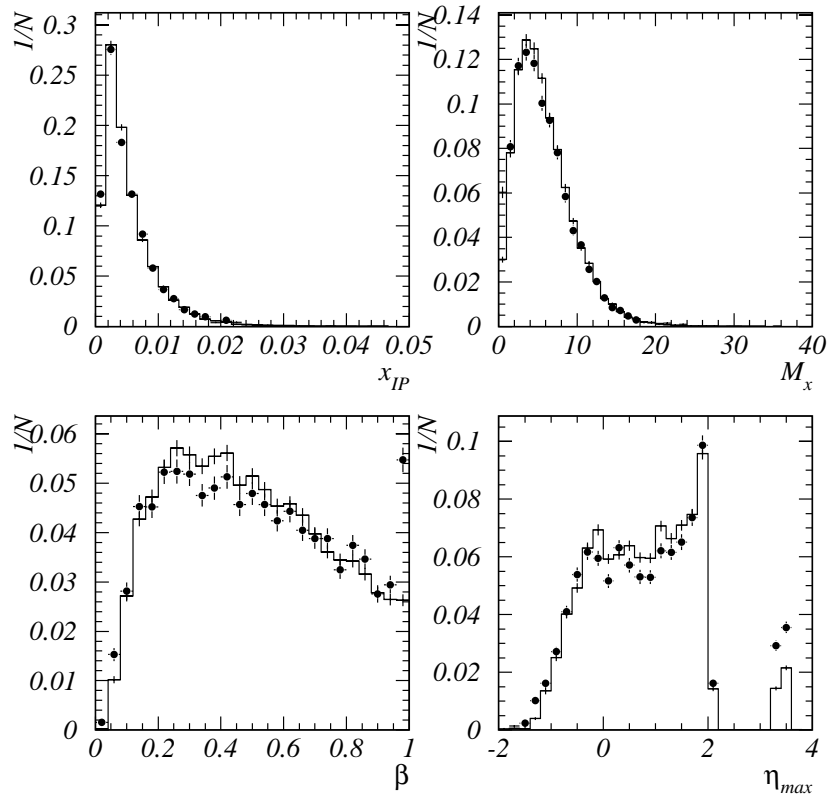


Figure 5.11: The diffractive variables M_X , x_{IP} , β and η_{max} for the DIFFMX event selection.

from this data sample and the reweighting of the \mathcal{R} contribution is not required. The DIFFMX event selection is not generally used to select diffractive events due to its restrictions on M_X and its lack of “control” on the Y (proton) system. It does have the advantage of simplicity and is easily calculated in generated Monte-Carlo.

5.6 Studies of Systematic Errors

5.6.1 Energy Scales

SpaCal Electromagnetic Energy Scale

The scattered electron energy is measured by the SpaCal calorimeter. This detector has an uncertainty in the energy scale for electrons of $\pm 1\%$. Any mismeasurement

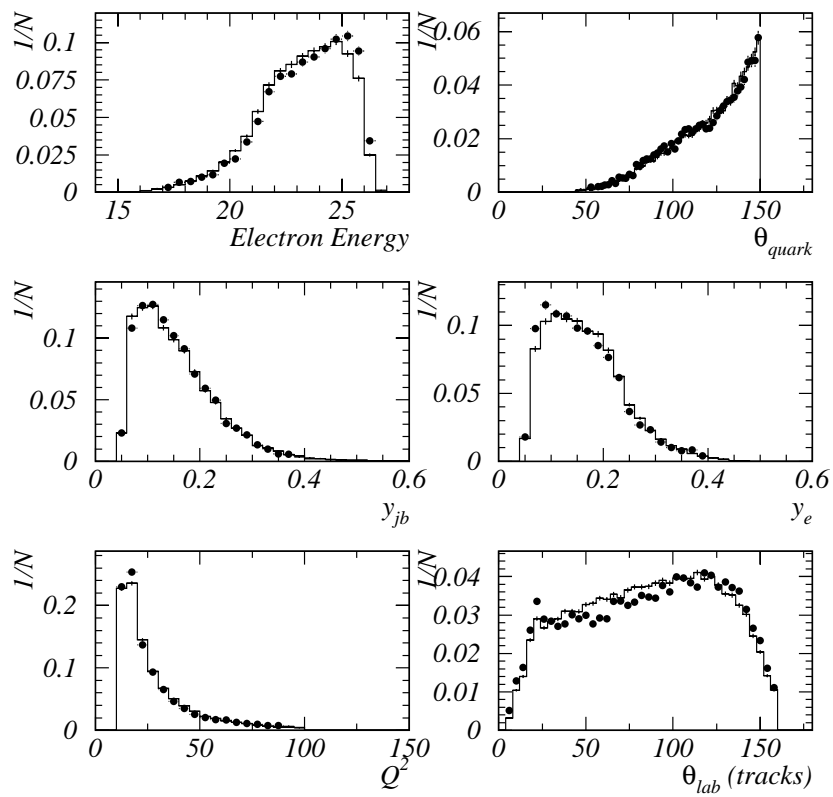


Figure 5.12: RAPGAP vs data for some event and track distributions for the DIFFMX event selection.

of the electron energy will lead to a miscalculation of the event kinematics, since the kinematics are calculated using the electron only method (see chapter 6). This then directly affects the boost to the Breit frame.

LAr Hadronic Energy Scale

The hadronic energy measurement is made by the LAr calorimeter which has a $\pm 4\%$ uncertainty in its energy scale. Only a few event variables use the hadronic energy measurement and changes to the energy scale has little effect on this analysis.

5.6.2 Monte-Carlo Corrections

Fragmentation model error

The MEAR Monte-Carlo used to make corrections to the data implements a fragmentation model based on the Colour Dipole Model. An alternative model is the parton shower model which is implemented in the MEPS Monte-Carlo. The differences between corrections made by the two Monte-Carlos is taken as a systematic uncertainty. This is in general the dominant systematic uncertainty.

\mathcal{R} contribution error.

In order to improve the M_X distribution for the DIFFMY selection the relative \mathcal{R} contribution has to be altered. The difference in the results obtained using the unaltered \mathcal{R} contribution compared to the altered \mathcal{R} contribution is taken as a systematic uncertainty.

Altering the \mathcal{R} contribution changes the relative proportion of large M_x events which mostly affects the target region of the Breit frame. As a result the effect of changing the \mathcal{R} contribution is seen mostly as a systematic error on the rapidity spectra.

Error from modifying the scattered electron energy.

The scattered electron energy distribution of the Monte-Carlo is modified in the DIS selection to improve the description of the data. The difference in the results obtained using the unaltered electron distribution compared to the altered electron distribution are negligible.

Error from altering the Z vertex.

As for the scattered electron energy distribution the z vertex distribution is altered to improve the Monte-Carlo description of the data. This alteration has a negligible effect on the physics results.

5.6.3 Detector Efficiency

Forward Muon Detector Efficiency.

To estimate the uncertainty in the FMD the efficiency is varied by $\pm 4\%$. This uncertainty has little effect on the results ($< 1\%$).

Proton Remnant Tagger Efficiency.

The uncertainty in the calibration of the PRT is estimated by varying the correction factors applied to the PRT in section 5.5.3 by $\pm 100\%$. This uncertainty has little effect on the results ($< 1\%$).

Track Reconstruction Efficiency.

Additional selections to the track quality cuts (see section 5.3) are made to assess their effect on the overall results and are added to the total systematic error.

Typical changes made to the track selection for the CJC are; $p_t > 0.25$ GeV, $DCA < 0.5$ cm, $R_0 < 25$ cm, track length > 25 cm, $30^\circ < \theta < 150^\circ$. The results is a typical systematic error of 3% on central tracks.

Typical changes made to the track selection for the FTD are; $P > 1.0$ GeV, $R_0 < 6$ cm, $\delta p/p \leq 0.25$, $\chi^2_{track\ fit}/NDF \leq 25.0$. The result is a typical systematic error of $10 \sim 15\%$ on Forward tracks⁵.

Fitting errors.

In chapter 8 the area around the peak of the fragmentation function is fitted with a Gaussian. An arbitrary definition of the peak region is taken as ± 1 unit around the peak position. Since this is not a strict definition we also vary this by ± 0.5 and take the difference in the peak and width results as a systematic error.

⁵Forward tracks are only used in the rapidity spectra

Chapter 6

Breit Frame Studies

6.1 Introduction

An overview of the Breit frame is presented together with an investigation to find the best method for reconstructing the event kinematics.

6.2 The Breit Frame

The Breit frame is collinear with the hadronic centre of mass but boosted along the z axis such that the incident virtual photon is completely space like, i.e. it has zero energy, zero transverse momentum and a z component of momentum (p_z) of $-Q$. The negative z axis is defined to be that of the incoming photon and is referred to as the current hemisphere. The positive z direction is called the target hemisphere.

In the naive quark parton model (QPM) the massless incoming quark has energy $Q/2$ and $p_z = +Q/2$, carrying a fraction x_{Bj} of the proton's momentum. After scattering it has energy $Q/2$ but $p_z = -Q/2$, Figure 6.1. In the case of diffraction we can simply insert an intermediate \mathbb{P} taking a fraction ($x_{\mathbb{P}}$) of the proton's momentum and the struck quark carrying a fraction β of the pomeron's momentum, such that $x_{Bj} = \beta x_{\mathbb{P}}$.

The Breit frame separates the struck quark from the proton remnant (the “specta-

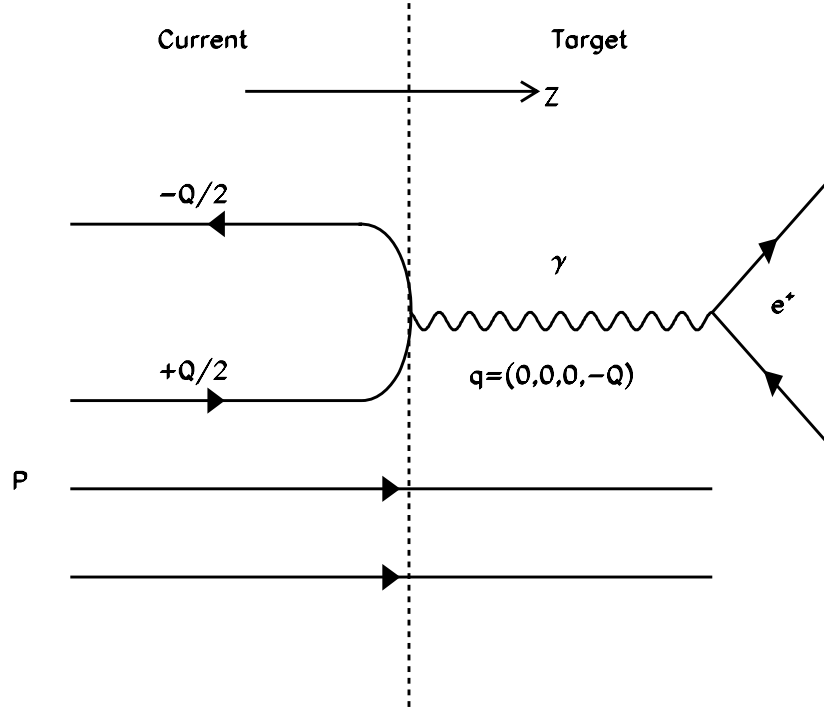


Figure 6.1: The Breit frame of reference in the quark parton model.

tor system”) with the current region dominated by the struck quark while the proton remnant is in the target region with much higher momentum. The struck quark stays within the central region of the H1 detector, where the acceptance is very good.

A comparison between the current hemisphere of the Breit frame and one half of an e^+e^- interaction can be made where the equivalent to the e^+e^- centre of mass energy, $\sqrt{s_{e^+e^-}} = E^*$, is Q , Figure 6.2.

Higher order processes such as BGF and initial state QCD Compton (figure 6.3a,b), which have no analogue in e^+e^- physics, together with final state QCD Compton (figure 6.3c), which does occur in e^+e^- , can, if the mass is large relative to Q , depopulate the current hemisphere of the Breit frame [49], sometimes leading to an empty current hemisphere. This phenomena of empty current hemispheres especially in the context of diffraction will be discussed later.

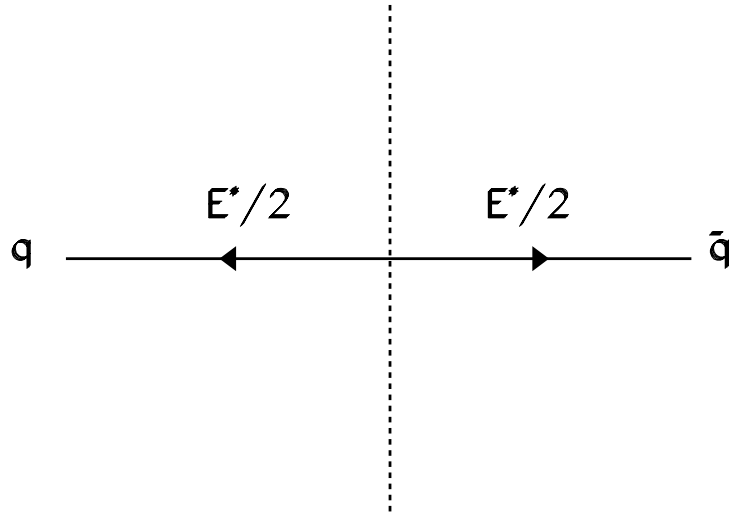


Figure 6.2: e^+e^- centre of mass system. One hemisphere is equivalent to the current hemisphere.

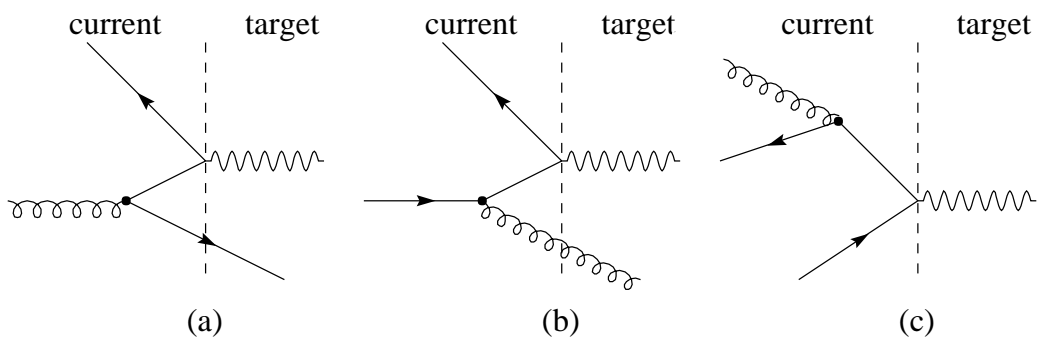


Figure 6.3: Higher order processes as viewed in the Breit frame. (a) BGF events, (b) initial state QCD Compton, and (c) final state QCD Compton.

6.3 Event Kinematics

Since the magnitude and direction of the boost to be applied to each particle in order to reach the Breit frame is a function of x and Q , the kinematic variables are important not only for event selection but also for the boost to the Breit frame. The event kinematics can be determined from several different methods [50], so it is important to choose the method that gives the best measure of the kinematic variables.

Both the electron beam energy (E_e) and proton beam energy (E_p) are known to a high accuracy in the laboratory frame, with the positive z -direction defined as the direction of the incoming proton. The energy (E'_e) and polar angle (θ_e) of the scattered electron is well measured, while the energy (E'_p) and polar angle (γ) of the total outgoing scattered hadronic system (the products of the fragmenting scattered proton) is less well measured due to the loss of hadrons at small angles down the beam pipe.

6.3.1 The Electron Method

The electron method uses only information from the scattered electron. This allows the kinematic variables to be calculated independently of the hadronic final state thus not explicitly biasing it. The electron method gives

$$Q_e^2 = 2E_e E'_e (1 + \cos \theta_e) \quad (6.1)$$

$$y_e = 1 - \frac{E'_e}{2E_e} (1 - \cos \theta_e) \quad (6.2)$$

$$x_e = \frac{E_e E'_e (1 - \cos \theta_e)}{E_p (2E_e - E'_e (1 - \cos \theta_e))} \quad (6.3)$$

where x_e is calculated from $Q_e^2 = s x_e y_e$. A problem with the electron method is that QED radiation can affect the angle and energy of the scattered electron resulting

in a mis-calculation of the kinematic variables especially in the low y region.

6.3.2 The Jacquet-Blondel Method

The Jacquet-Blondel (JB) method uses only the information from the hadronic final state and is thus most useful for determining the kinematics in charged-current events.

The JB method gives

$$y_{JB} = \frac{\sum_h (E_h - p_{z,h})}{2E_e} \quad (6.4)$$

$$Q_{JB}^2 = \frac{(\sum_h p_{z,h})^2 + (\sum_h p_{y,h})^2}{1 - y_{JB}} \quad (6.5)$$

$$x_{JB} = \frac{Q_{JB}^2}{s y_{JB}} \quad (6.6)$$

where the subscript h denotes hadrons and \sum_h is the sum over all detected hadronic objects. Due to the loss of hadrons down the beam pipe this method gives a poor measurement of Q^2 . This method does not suffer from QED radiation and can give a better measurement of y at low y ($y < 0.2$) than the electron method.

6.3.3 The Double Angle Method

The double angle (DA) method uses the polar angle of the scattered electron and the inclusive angle of the hadronic final state. The DA method assumes a homogeneous energy measurement over the full solid angle but is independent of absolute energy calibrations. The DA method gives

$$Q_{\theta_e \gamma}^2 = 4E_e^2 \frac{\sin \gamma (1 + \cos \theta_e)}{\sin \gamma + \sin \theta_e - \sin (\theta_e + \gamma)} \quad (6.7)$$

$$y_{\theta_e \gamma} = \frac{\sin \theta_e (1 - \cos \gamma)}{\sin \gamma + \sin \theta_e - \sin (\theta_e + \gamma)} \quad (6.8)$$

$$x_{\theta_e \gamma} = x_o \frac{\sin \gamma + \sin \theta_e + \sin (\theta_e + \gamma)}{\sin \gamma + \sin \theta_e - \sin (\theta_e + \gamma)} \quad (6.9)$$

where $x_o = E_e/E_p$.

6.3.4 The Sigma Method

The sigma method reconstructs the initial electron energy and hence is independent of initial state QED radiation. The Σ method uses

$$\Delta \equiv \Sigma + E'_e (1 - \cos \theta_e) = 2E_e \quad (6.10)$$

where $\Sigma = \Sigma_h (E_h - p_{z,h})$. If no particles escape detection the quantity Δ will equal twice the incident electron energy. The Σ method gives

$$y_\Sigma = \frac{\Sigma}{\Sigma + E'_e (1 - \cos \theta_e)} \quad (6.11)$$

$$Q_\Sigma^2 = \frac{E_e'^2 \sin^2 \theta_e}{1 - y_\Sigma} \quad (6.12)$$

$$x_\Sigma = \frac{Q_\Sigma^2}{s y_\Sigma} = \frac{E_e' \sin^2 \theta_e}{s y_\Sigma (1 - y_\Sigma)} \quad (6.13)$$

6.3.5 The Mixed Method

By combining the y measurement from the JB method together with the Q^2 measurement from the electron method we can extend the electron method measurements to lower values of y .

$$x_{MI} = \frac{Q^2}{s y_{JB}} \quad (6.14)$$

Q^2 bin (GeV ²)	Electron	DA	Sigma	JB	Mixed
$12 < Q^2 < 15$	0.043	0.091	0.068	0.248	0.060
$15 < Q^2 < 20$	0.043	0.099	0.070	0.279	0.063
$20 < Q^2 < 40$	0.049	0.098	0.068	0.273	0.059
$40 < Q^2 < 60$	0.049	0.095	0.075	0.266	0.061
$60 < Q^2 < 80$	0.067	0.090	0.098	0.262	0.074
$80 < Q^2 < 100$	0.084	0.089	0.112	0.257	0.091

Table 6.1: Resolution of Q^2 ($gQ^2 - Q^2$)/ gQ^2 (g indicates generator value)

Q^2 bin (GeV ²)	Electron	DA	Sigma	JB	Mixed
$12 < Q^2 < 15$	0.292	0.385	0.326	0.32	0.341
$15 < Q^2 < 20$	0.293	0.389	0.318	0.308	0.332
$20 < Q^2 < 40$	0.297	0.385	0.322	0.316	0.34
$40 < Q^2 < 60$	0.29	0.36	0.324	0.332	0.335
$60 < Q^2 < 80$	0.316	0.347	0.326	0.320	0.344
$80 < Q^2 < 100$	0.36	0.354	0.33	0.332	0.36

Table 6.2: Resolution of y ($gy - y$)/ gy (g indicates generator value)

6.3.6 Resolution Studies

The resolution in x , Q^2 , and y in bins of Q^2 are shown in Tables 6.1, 6.2, 6.3 for each of the different methods of reconstructing the event kinematics. The rms is used to calculate the resolution and the Q^2 bins used are the same as those used throughout this analysis. Previous studies have shown the most important variables in the evolution of fragmentation properties is Q therefore this is the most important variable to measure with the best accuracy.

The electron only method gives the best resolution in Q^2 , y and x . Other methods apart from the Jacquet-Blondel method also provide a reasonable reconstruction of the kinematics but are never able to compete with the electron method simultaneously for the three kinematic variables examined. Figures 6.4 and 6.5 show the Q^2 and x resolution for all five methods in the Q^2 range $15 < Q^2 < 20$ GeV², the superior resolution of the electron method is clearly visible.

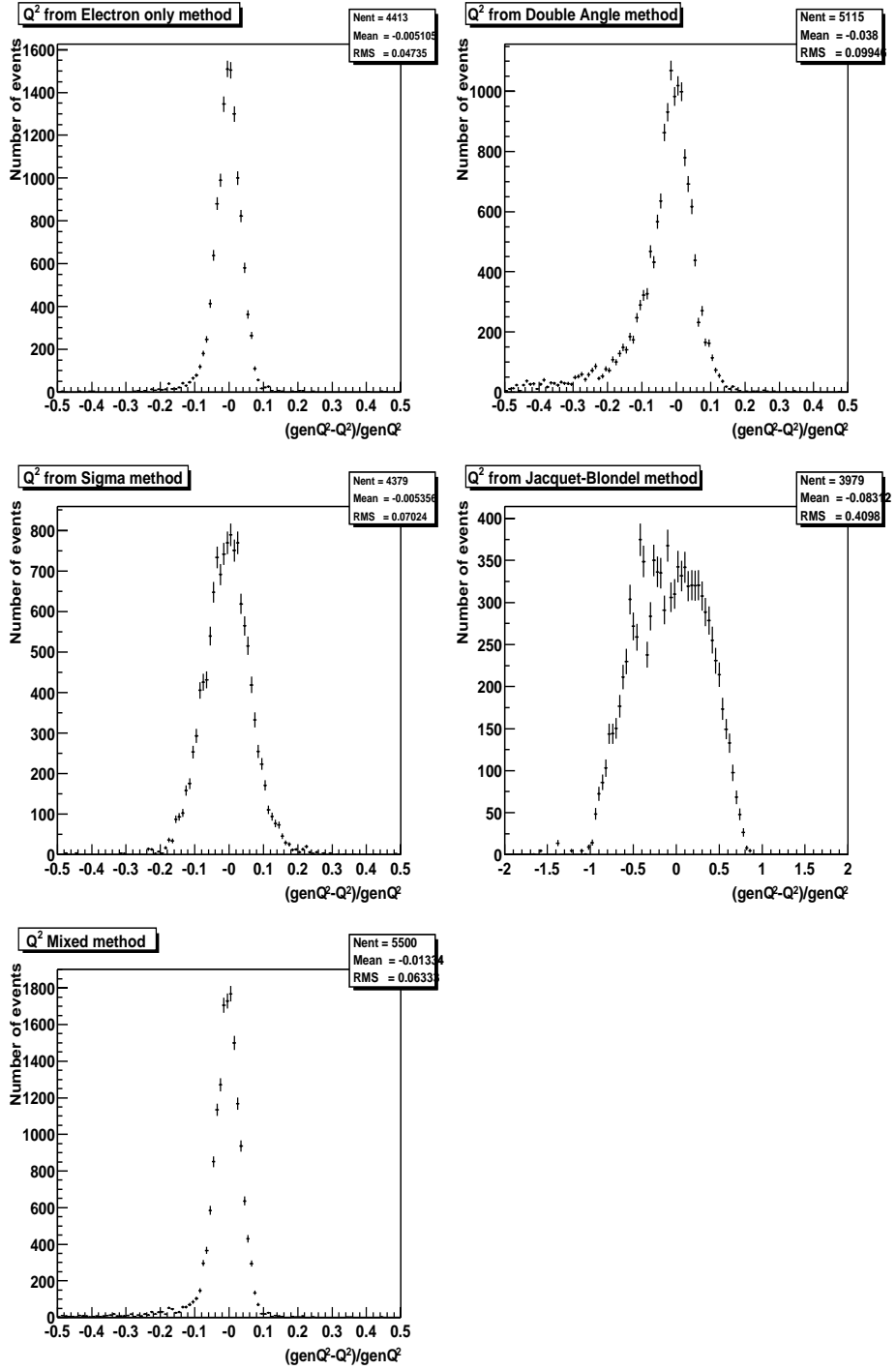


Figure 6.4: The resolution of Q^2 for the five different reconstruction methods in the Q^2 range $15 < Q^2 < 20 \text{ GeV}^2$.

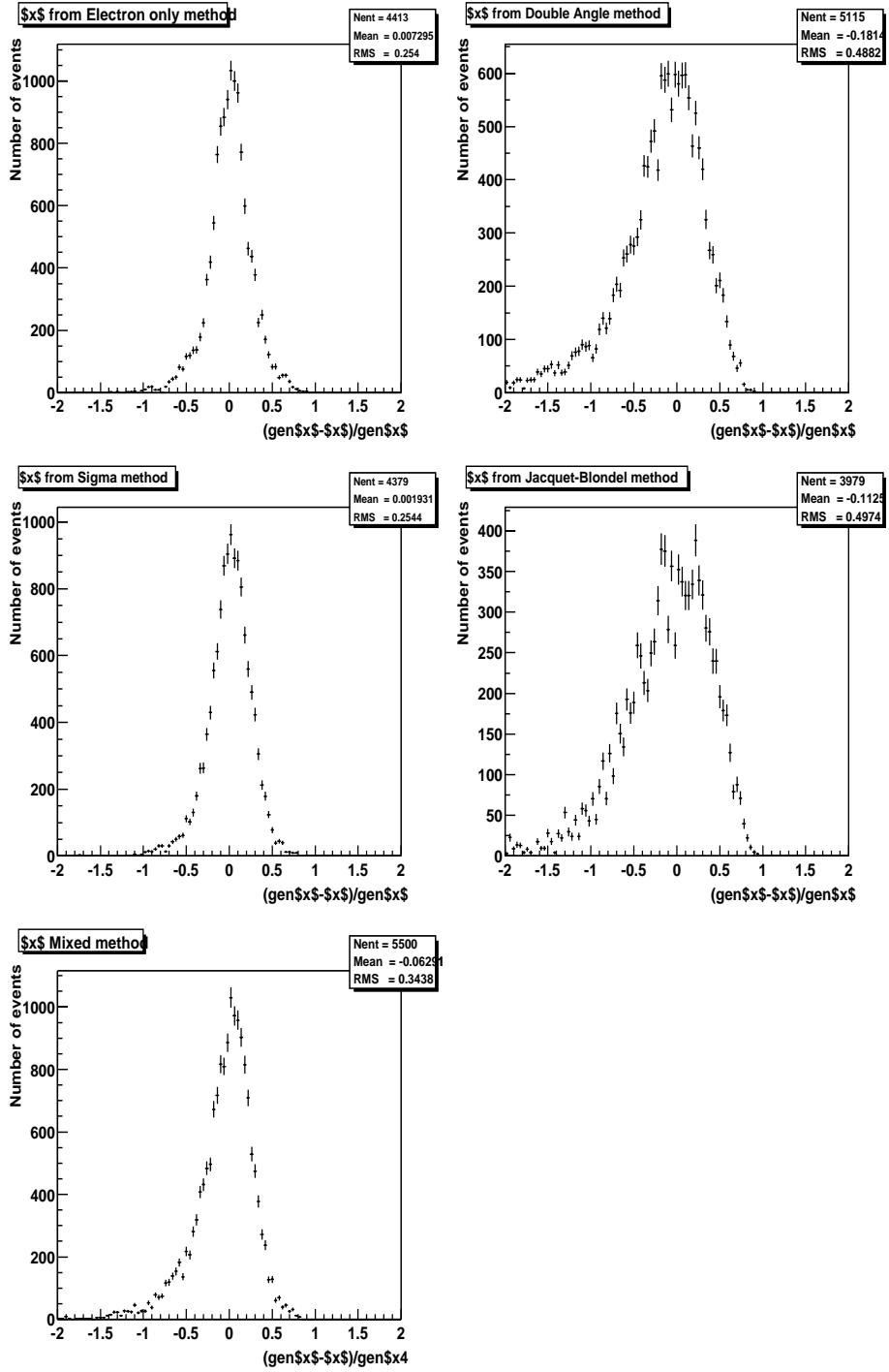


Figure 6.5: The resolution of x for the five different reconstruction methods in the Q^2 range $15 < Q^2 < 20 \text{ GeV}^2$.

Q^2 bin (GeV ²)	Electron	DA	Sigma	JB	Mixed
$12 < Q^2 < 15$	0.246	0.488	0.27	0.412	0.356
$15 < Q^2 < 20$	0.254	0.488	0.254	0.497	0.344
$20 < Q^2 < 40$	0.232	0.429	0.239	0.623	0.335
$40 < Q^2 < 60$	0.221	0.355	0.226	0.663	0.309
$60 < Q^2 < 80$	0.237	0.32	0.235	0.625	0.297
$80 < Q^2 < 100$	0.273	0.282	0.228	0.619	0.284

Table 6.3: Resolution of $x(gx - x)/gx$ (g indicates generator value). Highlighted values show the best resolution.

Chapter 7

Rapidity Spectra

7.1 Introduction

The Rapidity (Y) for a given hadron is defined as

$$Y = \frac{1}{2} \ln \left(\frac{E + p_z}{E - p_z} \right) \quad (7.1)$$

where p_z is the longitudinal momentum. For this analysis the energy, E , is calculated assuming that each charged hadron has the mass of a pion. Corrections are made using Monte-Carlo to take the admixture of other particles into account. In the Breit frame the positive Y direction is that of the incoming proton and the negative direction that of the virtual photon.

In the fragmentation modified Quark Parton Model (QPM) the hadronic final state of DIS consists of a jet of hadrons originating from the struck quark (current jet) and hadrons produced by the proton remnant. Including QCD modifications, the phase space between the current jet and the proton remnant is filled with particles produced from the emission of gluons created by the colour transfer between the struck quark and the proton remnant. This produces a *rapidity plateau*¹ as shown by the solid line in figure 7.1.

¹As predicted by Feynman [51].

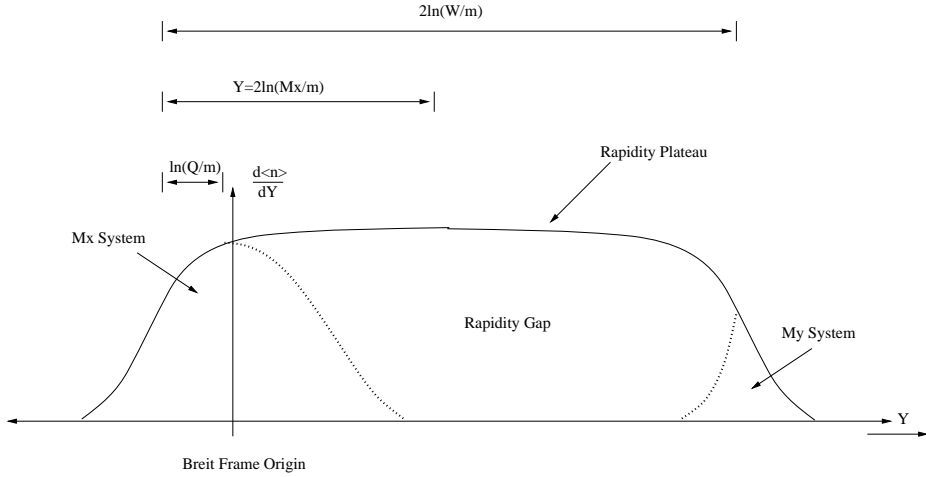


Figure 7.1: The rapidity plateau as seen in the Breit frame.

The width of the rapidity distribution, the longitudinal phase space, scales with energy and is typically given by

$$2 \ln (W / m) = 2 \ln (Q / m) + \ln ((1 - x) / x) \quad (7.2)$$

where m is the mass of the hadron and $\ln(Q/m)$ is the width of the distribution in the current hemisphere of the Breit frame. There is good detector acceptance for tracks in the $-Y$ region in the hadronic centre of mass, which includes the entire current region of the Breit frame.

In diffraction there is no colour transfer between the proton (M_y system) and M_x system and the expectation is of a *rapidity gap* between the proton and M_x system as shown by the dotted line in figure 7.1. The expected width of the M_x system is $2 \ln(M_x/m)$, while the width of the current hemisphere of the Breit frame is still $\ln(Q/m)$ allowing a direct comparison with non-diffractive DIS and e^+e^- . There is good detector acceptance for tracks in the entire M_x system.

In [27] a parameterisation has been made of the diffractive DIS cross section, the main features of which is the decomposition of the β spectrum into three contributions: $q\bar{q}g$ production (dominating at low β) and transverse and longitudinal $q\bar{q}$ production (dominating at medium and high β). This motivates the subdivision of the DIFFMY

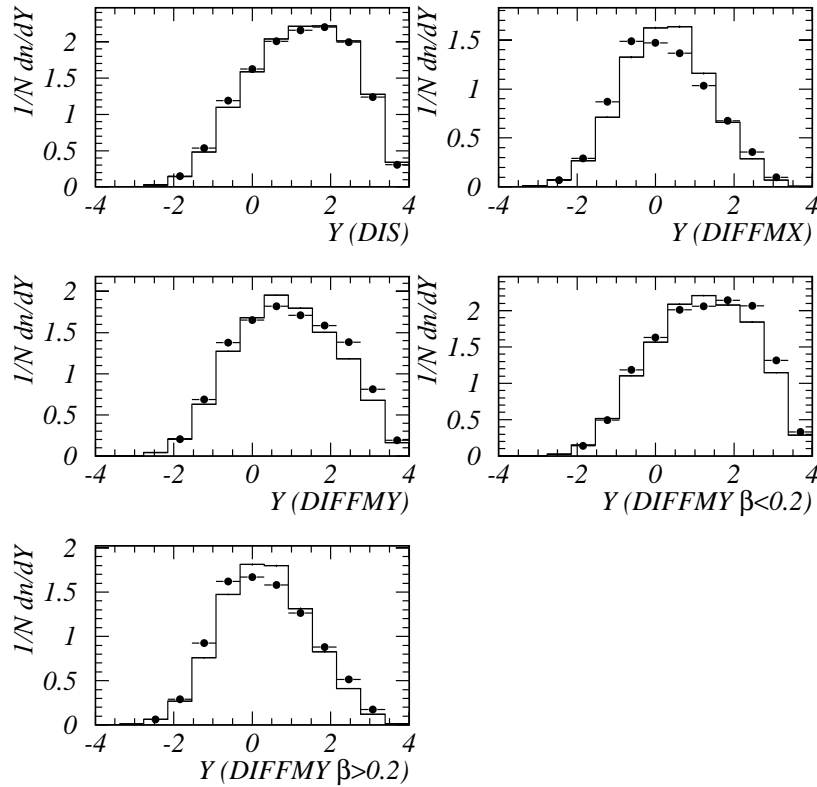


Figure 7.2: Comparison between uncorrected Data and reconstructed MEAR (for DIS) or RAPGAP (for the diffractive selections). (statistical errors only)

selection into two different β regions, $\beta < 0.2$ and $\beta > 0.2$.

7.2 Data Quality

Data Monte-Carlo Comparison

Figure 7.2 shows a comparison between uncorrected data and MEAR (for DIS) or RAPGAP (for the diffractive selections) Monte-Carlos. MEAR provides a very good description of the data and although the RAPGAP description of the data is imperfect there are no major discrepancies which would cast doubt on the use of the Monte-Carlo to correct the data.

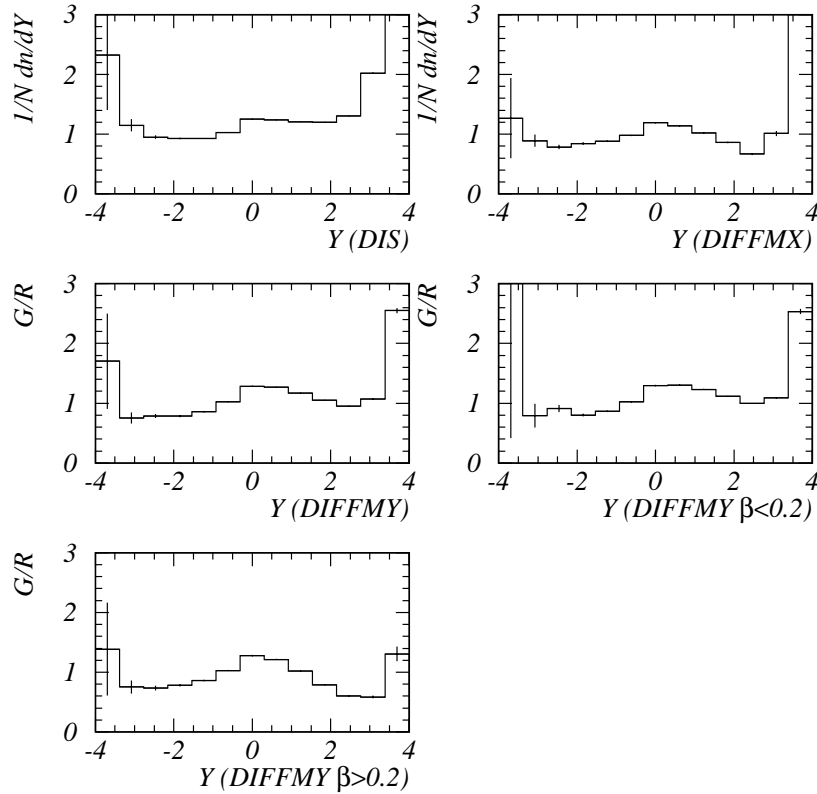


Figure 7.3: Acceptance correction factors with statistical errors. The correction factor for DIS in the last bin is 8, for DIFFMX is 20. (statistical errors only)

Correction Factors

The data is corrected for detector acceptance and QED radiative effects (see chapter 5). Figure 7.3 shows the correction factors applied to the data for the rapidity distributions. In general the correction factors are close to unity ($\sim 1 \pm 20\%$) and stable. Correction factors much larger than 1 means increasing reliance on a good Monte-Carlo description of the data.

Resolutions and purity

The resolution is defined as the difference between the generated and reconstructed rapidity of a track. For each interval in rapidity we assume that the distribution of the differences is a Gaussian and take the RMS value as the resolution. In figure 7.4

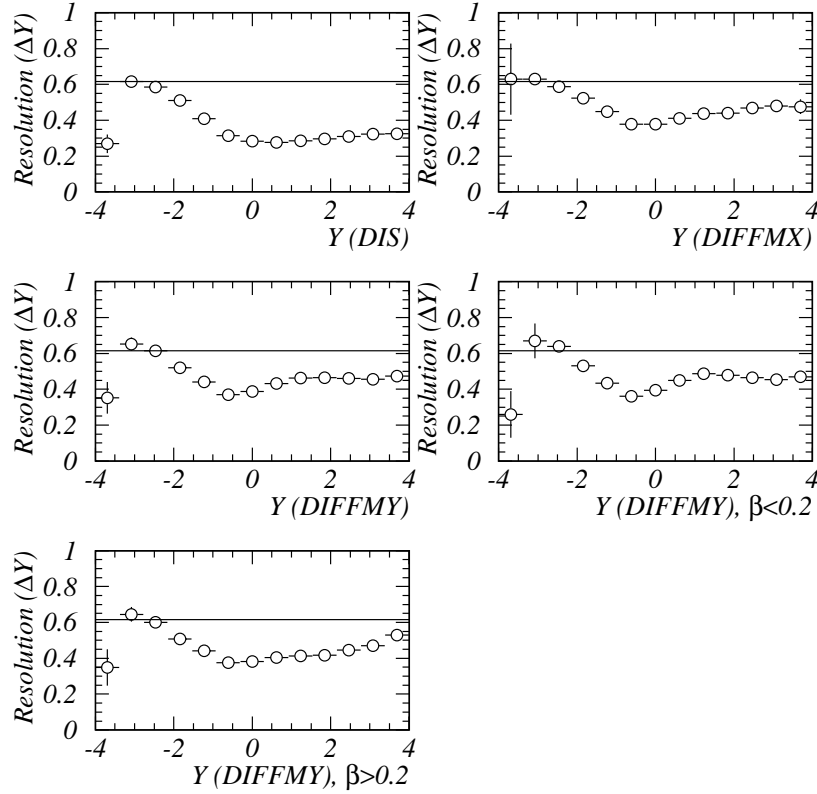


Figure 7.4: The resolution in Y as a function of Y for the different event selections. The solid line shows the bin-width ($Y \sim 0.6$). (statistical errors only)

the resolution in Y is shown as a function of Y . Over most of the rapidity distribution and in all event selections the resolution is smaller than the bin-width. Only in the first 3 intervals ($Y < -2.0$) is the value of the resolution close to the bin-width.

The purity is defined as the proportion of tracks in a given analysis interval after simulation and reconstruction procedures that were generated in that interval. Figure 7.5 shows the purity of Y for the different event selections. In general the purity is greater than 35%, but in the first 3 intervals the purity is lower.

Due to the low purity and bad resolution the first 3 intervals in rapidity have been dropped from the analysis. They have very few tracks and their removal does not affect the results of the analysis. Due to the very large correction factor of the last interval it has also been removed from the analysis although the results from this

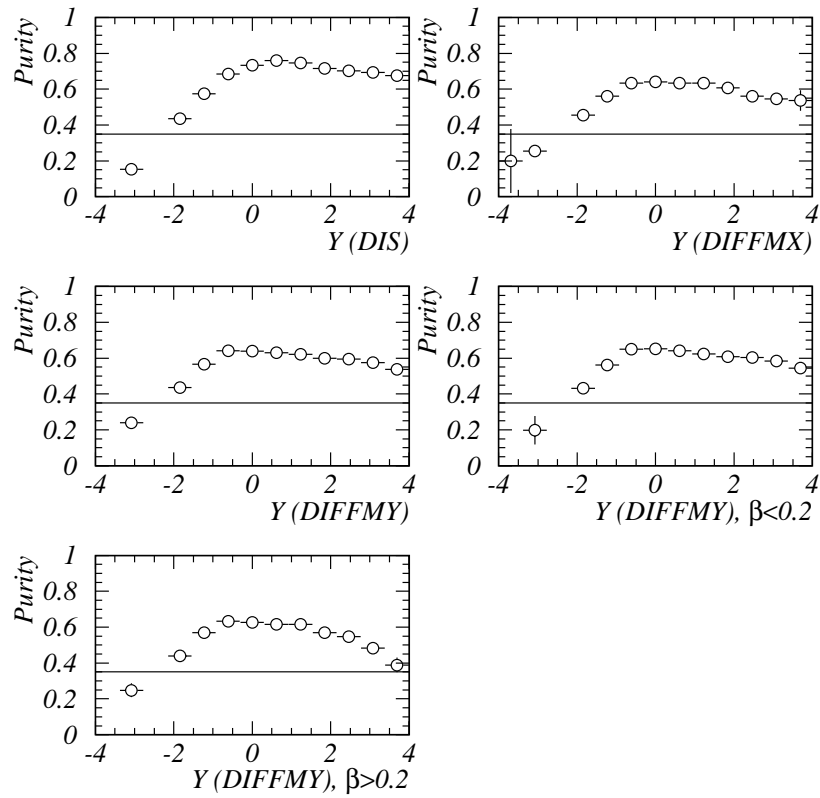


Figure 7.5: The purity in Y as a function of Y for the different events selections. The solid line shows an (arbitrary) minimum value for the purity of 35%. In some intervals there are no data points because no tracks were both generated and reconstructed in that interval. (statistical errors only)

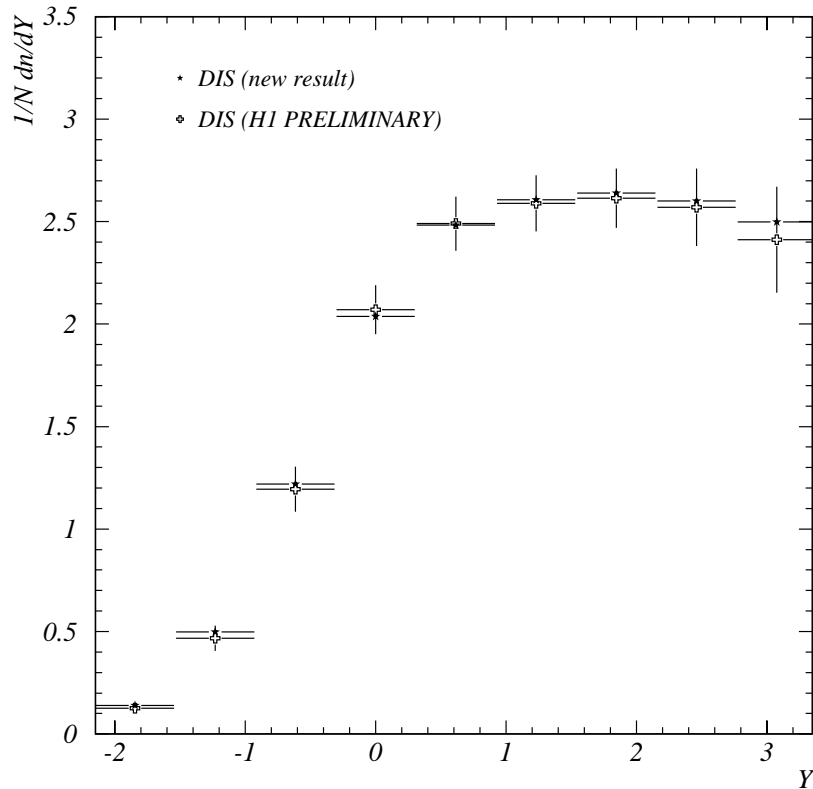


Figure 7.6: Comparison in rapidity of preliminary DIS results with the most recent (this analysis) DIS results (statistical and systematic errors).

interval are still consistent with the smoothly varying Y distribution observed in the other intervals.

Systematic Errors

The statistical errors for all distributions are negligible. The errors for all distributions are dominated by a correlated systematic error due to the different fragmentation models (MEAR and MEPS) of about $\sim 7\%$ (see chapter 5).

7.3 Results

New DIS results compared with Preliminary Results

The rapidity intervals used in this analysis are the same intervals used to obtain the preliminary result [44]. This allows us to compare directly the DIS results as a cross check between the two analyses (figure 7.6). The new DIS results agree quite well with the old, but they do show a slightly higher multiplicity in the target region. Over the past two years there has been several changes to the analysis.

- There have been several new releases of the H1 analysis software which have introduced new software features and hopefully removed some bugs (but has possibly introduced some more!). The new software has also introduced a new calibration of the calorimeters.
- Changes in the steering cards used to control the H1 analysis software have been introduced to improve the quality of the data. This includes changes in the type of calibration that the LAr calorimeter uses, the refinements to the electron finder, and removal of the plug calorimeter information due to its poor modelling in the Monte-Carlos simulation.
- The 1996 data has been reprocessed to benefit from an improved understanding of the detector.

No single change could be traced as the prime cause of the difference. As it stands the new result should be considered as summarising the best understanding of the detector and software currently available.

DIS compared with DIS2

For the DIS selection, diffractive events are removed because they are not well modelled in the Monte-Carlo used (MEAR). Diffractive event have been removed historically by using the $egap > 0.5\text{ GeV}$ cut (the DIS selection). This cut has the advantage

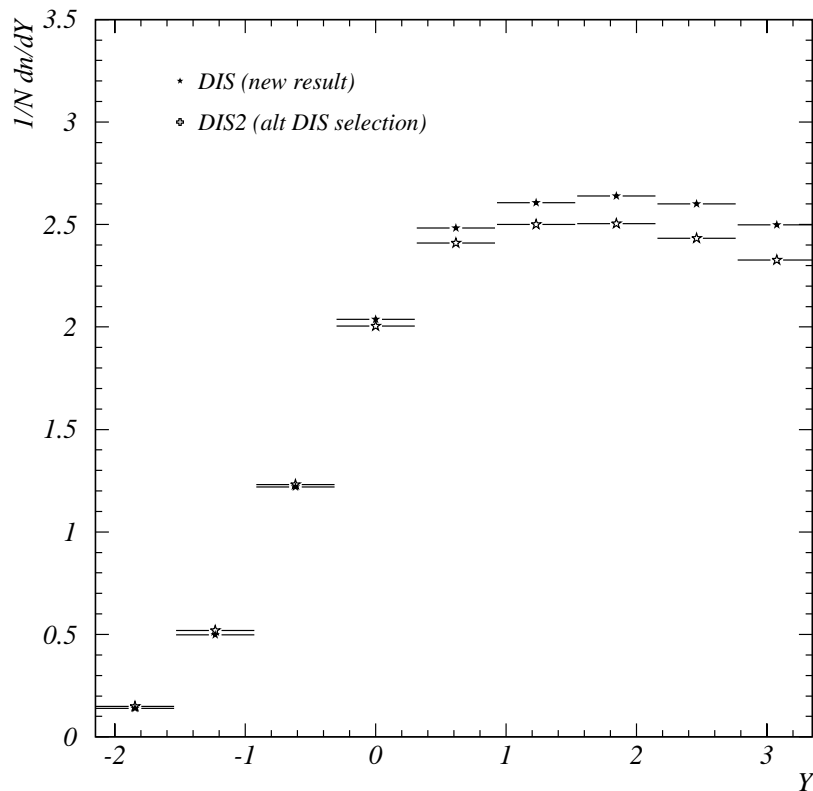


Figure 7.7: Comparison in rapidity of two different definitions of deep-inelastic scattering, DIS ($egap > 0.5$ GeV) and DIS2 (\overline{DIFFMY}) (statistical errors only). Note that it is expected that the results should not be differentially affected by the systematic errors.

of simplicity (it only uses the LAr calorimeter) and can be applied effectively at both reconstructed and generated levels. It is also possible to remove diffractive events using the DIFFMY cuts, this is called the DIS2 selection.

Figure 7.7 compares the DIS and DIS2 selections, an excess of events in the target region is observed for the DIS selection. In the DIS event selection the *egap* cut requires there to be hadronic activity in the forward region ($2.2 < \eta < 3.2$) of the LAr, while the DIS2 event selection requires there to be activity only in the very forward region ($\eta > 3.3$). It is therefore not surprising to see more tracks in the forward region in the DIS event selection than in the DIS2 selection. Indeed the multiplicity in the target region can be forced to rise further by requiring even more activity in the region .

Diffractive compared with DIS

Figure 7.8 shows the rapidity distributions for DIS and diffractive event selections. Compared to DIS, diffractive events have a higher multiplicity in the current region. This is discussed in detail in Chapter 8. By definition the multiplicity of diffractive events must approach zero at the beginning of the rapidity gap. This effect is clearly seen for both DIFFMX and DIFFMY selections. In the DIFFMX selection the rapidity gap is shifted to the left, the peak of the data is narrower and the multiplicity is lower than that for DIFFMY, consistent with its more restrictive M_X range. The distribution for the DIS selection shows a plateau in the target region, which has been investigated in [30].

High/low β DIFFMY

Figure 8.10 shows that for $\beta > 0.2$ the rapidity distribution is symmetric about the Breit frame origin consistent with a quark back to back in either hemisphere. The selection $\beta < 0.2$ gives a broader and more asymmetric distribution extending further into the target hemisphere of the Breit frame. This would be consistent with a $q\bar{q}g$

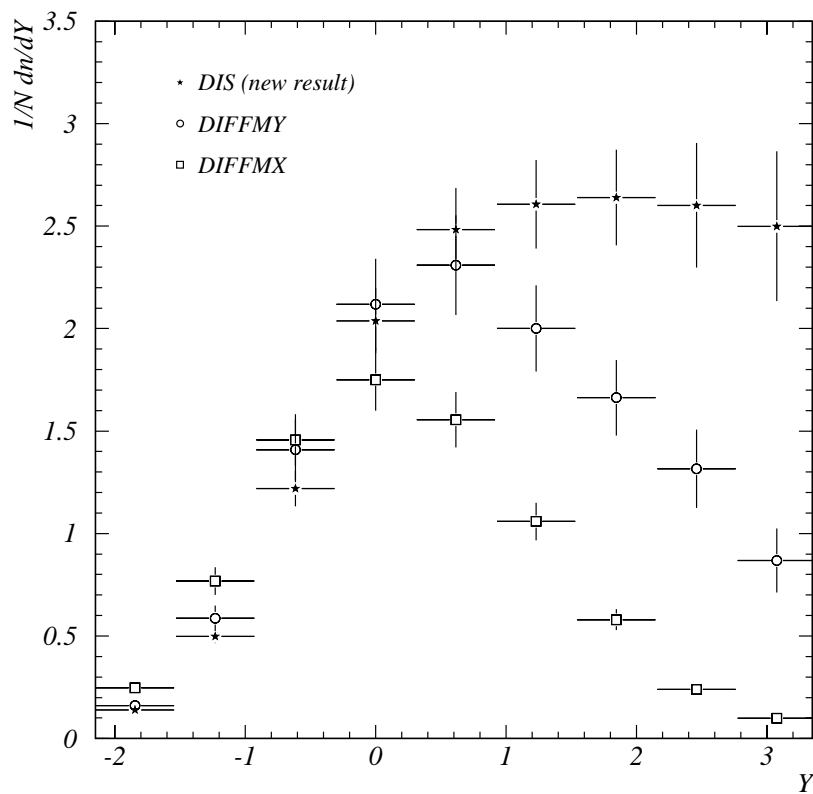


Figure 7.8: Rapidity plateau data comparing DIS, DIFFMX and DIFFMY selections (statistical and systematic errors).

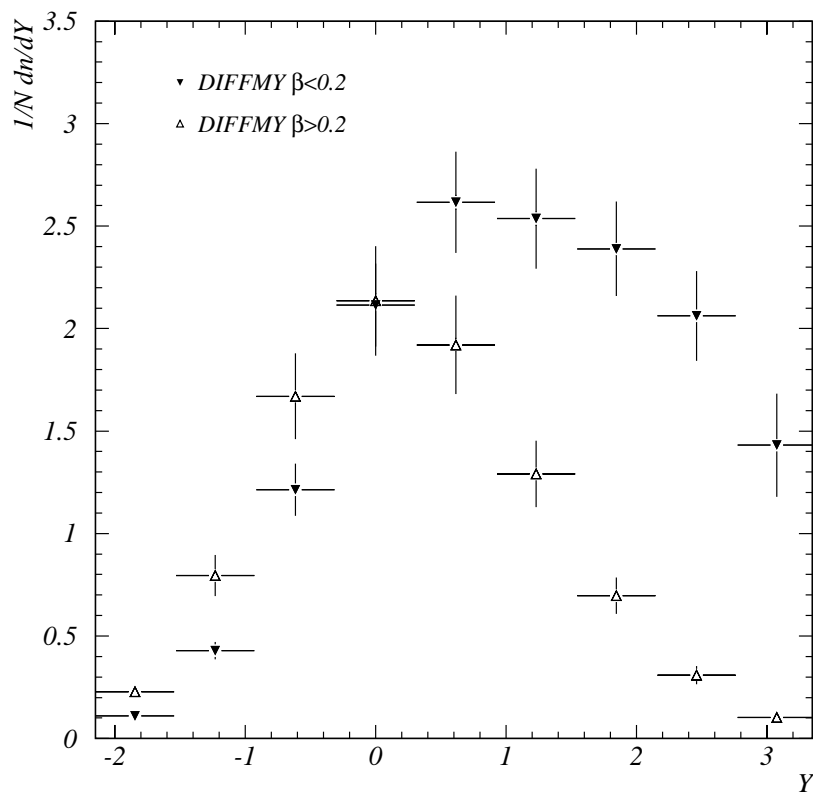


Figure 7.9: Rapidity plateau data comparing DIFFMY for $\beta < 0.2$ and $\beta > 0.2$ (statistical and systematic errors).

system as claimed in [27].

From equation 7.3

$$\beta = \frac{Q^2}{Q^2 + M_X^2}, \quad (7.3)$$

there is a relationship between β , Q^2 and M_X so that low (high) β is large (small) M_X . This means that a high β selection restricts the multiplicity of the observed hadronic system, which is related to M_X , making it look more like the result of a $q\bar{q}$ system, and vice versa for low β . It is difficult to separate kinematic phase space effects from a dynamic effect such as that which motivated the selection in β [27].

7.4 Model comparisons

One of the major goals of this thesis is to compare the data with various models of diffraction that were introduced in chapter 8:

In [1] the H1 collaboration interpreted the measurement of the diffractive structure function, $F_2^{D(3)}$, in terms of a resolved pomeron model incorporating a leading diffractive exchange and a subleading reggeon contribution. Three different parameterisations were presented, a quark dominated parameterisation (fit 1)² and two gluon dominated parton distributions, a ‘flat gluon’ (fit 2) and a ‘peaked gluon’ (fit 3). Figure 7.10 shows that (the generally preferred [53]) fit 2 gives a good description of the diffractive rapidity distribution and that fit 2 and fit 3 cannot be differentiated. Fit 1 clearly does not describe the data and shows that the rapidity distribution is sensitive to different models of diffraction.

Diffractive DIS can be treated (in the proton rest frame) by considering the $q\bar{q}$ and $q\bar{q}g$ photon fluctuations as colour dipoles [27]. The saturation model by Golec-Biernat and Wusthoff [54][55] uses the colour dipole approach, with an ansatz for the dipole cross section which interpolates between the perturbative and non-perturbative

²The fit 1 parameterisation has been shown to be very similar to e^+e^- ([52]).

regimes of the γ^*p cross section. The model does not describe the data as well as fits 2 and 3 of the resolved pomeron model, predicting a lower multiplicity in the central region.

In the soft colour interaction model (SCI), diffraction occurs through soft colour rearrangements between the outgoing partons. The original SCI model [28] used only one free parameter, the universal colour rearrangement probability, fixed by a fit to $F_2^{D(3)}$. A recent refinement to the model [56] has been made by making the colour rearrangement probability proportional to the normalised difference in the generalised area of the string configurations before and after the rearrangement.

SCI as implemented in LEPTO both in the original and refined forms together with a version of LEPTO without SCI are compared with the data in figure 7.11. The new versions of SCI improves the description of the rapidity spectra for DIS in the target region compared to the old version but still the version of LEPTO without SCI gives a better description. Despite the significant changes to the rapidity spectra for DIS the diffractive distributions show very little effect due to these changes. SCI describes the rapidity spectra at high β but underestimates the multiplicity in the target region at low β .

All the models discussed are able to describe at least qualitatively the differences between high and low β indicating that they are mainly resulting from phase space restrictions which are due to the correlation between β and M_x .

7.5 Summary

The rapidity spectra presented in this chapter have been shown to have high purity and stable correction factors for DIS and diffractive event selections.

- The results for the DIS event selection are consistent with the previous analysis of rapidity on the 1996 data. This gives us confidence in the quality of the results present on rapidity.

H1 PRELIMINARY

- · · RES. IP (H1 fit1)
- - - RES. IP (H1 fit2)
- · · RES. IP (H1 fit3)
- Saturation model

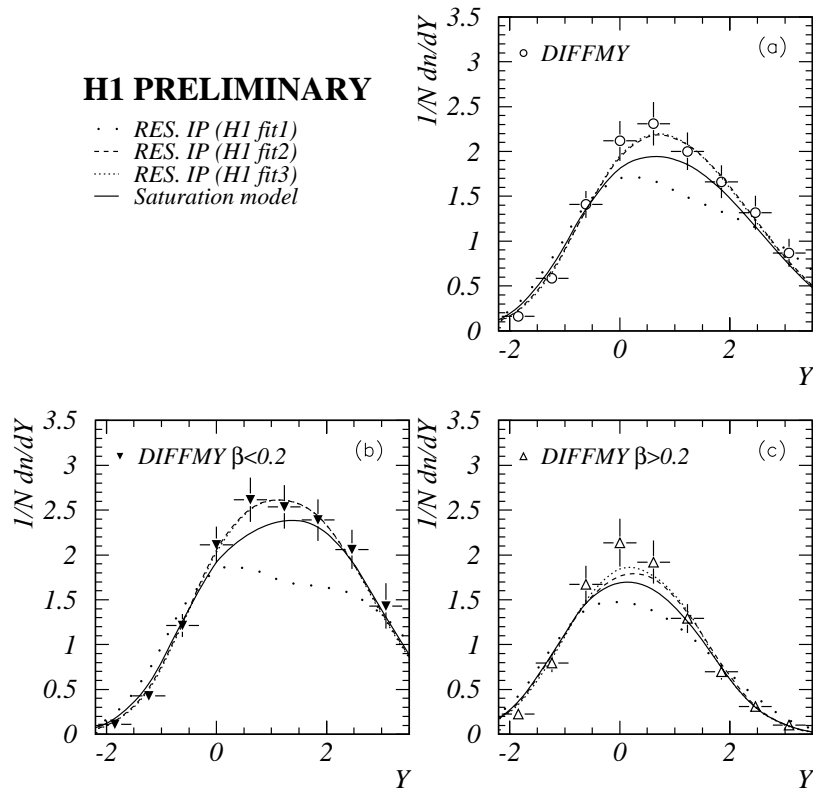


Figure 7.10: Comparison of rapidity distributions with predictions from a resolved pomeron model using three different parameterisations from H1 and the saturation model. For (a) the DIFFMY selections, (b) low β DIFFMY, and (c) high β DIFFMY.

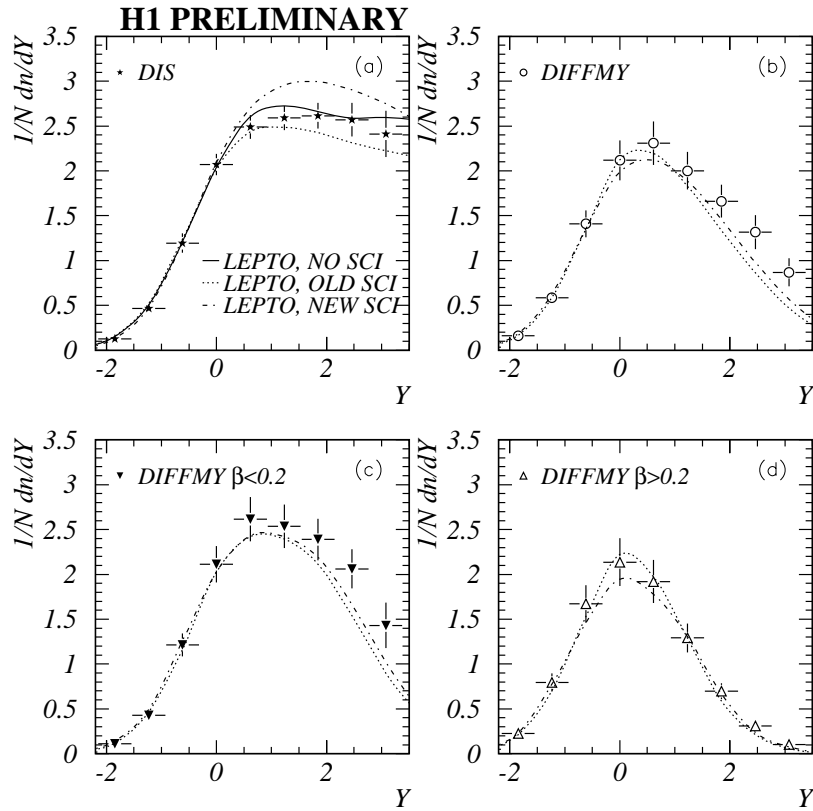


Figure 7.11: Comparison of rapidity distributions from the LEPTO Monte-Carlo with different implementations of Soft Colour Interactions (SCI). For (a) the DIFFMY selections, (b) low β DIFFMY, and (c) high β DIFFMY. Note that only in the high β DIFFMY sample can fits 2 and 3 be differentiated.

- Differences between DIS and DIS2 are due to changes in the definition of “*egap*” (the forward activity requirement of the event selection). It should be noted that *egap* is part of the definition of the truth phase space and is therefore accounted for in comparisons with Monte-Carlo models.
- Differences between DIFFMX and DIFFMY are due to changes in the definition of the rapidity gap. The more restrictive nature of the DIFFMX selection produces a smaller observed hadronic system.
- The above two points reinforces the importance of taking into account the slightly different definitions of diffraction that exist when making comparisons of results (e.g. ZEUS select diffractive events by tagging the scattered proton compared to the H1 method of finding a rapidity gap).
- The DIFFMY distribution is consistent with the expectation for final states from $q\bar{q}$ at high β and $q\bar{q}g$ at low β but is also reproduced in models where there is no explicit modeling of these final state configurations, suggesting that these effects are a result of restricting the phase space that is implicit in making a selection in β .
- Comparison with a variety of model shows that the resolved pomeron model using H1 fit 2 (or 3) provides the best description of the rapidity spectra as previous studies of diffractive DIS have shown [53][52].

Using rapidity spectra we have been able to investigate two of the three principle aims of this thesis as set out in chapter \ref{ch:dis} (testing different models of diffraction and different definitions of diffraction). To study the remaining principle aim (quark fragmentation universality), and to further study the other aims, the following two chapters will examine the evolution of the fragmentation function and p_t spectra with Q .

Y Range	DIS	DIFFMX	DIFFMY
$-2.15 < Y < -1.54$	$0.138 \pm 0.003 \pm 0.01$	$0.247 \pm 0.009 \pm 0.021$	$0.16 \pm 0.005 \pm 0.018$
$-1.54 < Y < -0.92$	$0.497 \pm 0.005 \pm 0.038$	$0.768 \pm 0.016 \pm 0.066$	$0.59 \pm 0.011 \pm 0.062$
$-0.92 < Y < -0.31$	$1.22 \pm 0.008 \pm 0.093$	$1.46 \pm 0.02 \pm 0.12$	$1.41 \pm 0.02 \pm 0.15$
$-0.31 < Y < 0.31$	$2.03 \pm 0.01 \pm 0.16$	$1.75 \pm 0.03 \pm 0.15$	$2.12 \pm 0.02 \pm 0.22$
$0.31 < Y < 0.92$	$2.48 \pm 0.01 \pm 0.19$	$1.56 \pm 0.03 \pm 0.13$	$2.31 \pm 0.03 \pm 0.24$
$0.92 < Y < 1.54$	$2.61 \pm 0.01 \pm 0.20$	$1.06 \pm 0.019 \pm 0.090$	$2.00 \pm 0.02 \pm 0.21$
$1.54 < Y < 2.15$	$2.64 \pm 0.01 \pm 0.22$	$0.580 \pm 0.013 \pm 0.050$	$1.66 \pm 0.02 \pm 0.18$
$2.15 < Y < 2.77$	$2.60 \pm 0.01 \pm 0.26$	$0.240 \pm 0.008 \pm 0.023$	$1.32 \pm 0.02 \pm 0.19$
$2.77 < Y < 3.38$	$2.50 \pm 0.01 \pm 0.30$	$0.098 \pm 0.006 \pm 0.012$	$0.87 \pm 0.02 \pm 0.16$

Table 7.1: $1/Ndn/dY$ as a function of Y for the DIS, DIFFMX and DIFFMY selections. The errors are the statistical error and then systematic error

Y Range	DIFFMY $\beta < 0.2$	DIFFMY $\beta > 0.2$
$-2.15 < Y < -1.54$	$0.11 \pm 0.006 \pm 0.01$	$0.23 \pm 0.01 \pm 0.03$
$-1.54 < Y < -0.92$	$0.43 \pm 0.01 \pm 0.04$	$0.80 \pm 0.02 \pm 0.10$
$-0.92 < Y < -0.31$	$1.21 \pm 0.02 \pm 0.12$	$1.67 \pm 0.03 \pm 0.21$
$-0.31 < Y < 0.31$	$2.11 \pm 0.03 \pm 0.20$	$2.14 \pm 0.04 \pm 0.26$
$0.31 < Y < 0.92$	$2.62 \pm 0.04 \pm 0.24$	$1.92 \pm 0.03 \pm 0.24$
$0.92 < Y < 1.54$	$2.54 \pm 0.04 \pm 0.24$	$1.29 \pm 0.03 \pm 0.16$
$1.54 < Y < 2.15$	$2.39 \pm 0.03 \pm 0.23$	$0.70 \pm 0.02 \pm 0.09$
$2.15 < Y < 2.77$	$2.06 \pm 0.03 \pm 0.22$	$0.31 \pm 0.01 \pm 0.04$
$2.77 < Y < 3.38$	$1.43 \pm 0.03 \pm 0.25$	$0.10 \pm 0.006 \pm 0.02$

Table 7.2: $1/Ndn/dY$ as a function of Y for the low and high β DIFFMY selections. The errors are the statistical error and then systematic error

Chapter 8

The Fragmentation Function

8.1 Introduction

In $e^+e^- \rightarrow q\bar{q}$ the momentum distribution of hadrons produced from quark fragmentation scales to first order with the centre of mass energy (CMS), $\sqrt{s_{ee}} = E^*$. The fraction of momentum taken by a final state hadron of the total energy that the hadron could have in one hemisphere is $x_p = 2p_{hadron}^\pm/E^*$. This assumes that there is an equal share of energy between the two hemispheres, due to final state QCD Compton this need not be the case ($e^+e^- \rightarrow q\bar{q}g$). In the current hemisphere of the Breit frame, where $Q \sim E^*$, the equivalent variable is $x_p = 2p_{hadron}^\pm/Q$. In addition to final state QCD Compton there is also initial state QCD Compton and BGF processes that cause the available energy to differ similarly from $Q/2$ in the current hemisphere of the Breit frame.

The single particle inclusive scaled momentum distribution $D(x_p)$ is defined as

$$D^\pm(x_p, Q) = (1/N) \times dn_{tracks}^\pm/dx_p. \quad (8.1)$$

It is an event normalised charged track density (integrated over x_{Bj} where dependence has been found to be very weak [57]) commonly termed the fragmentation function. This function characterises the complete process of final state parton shower

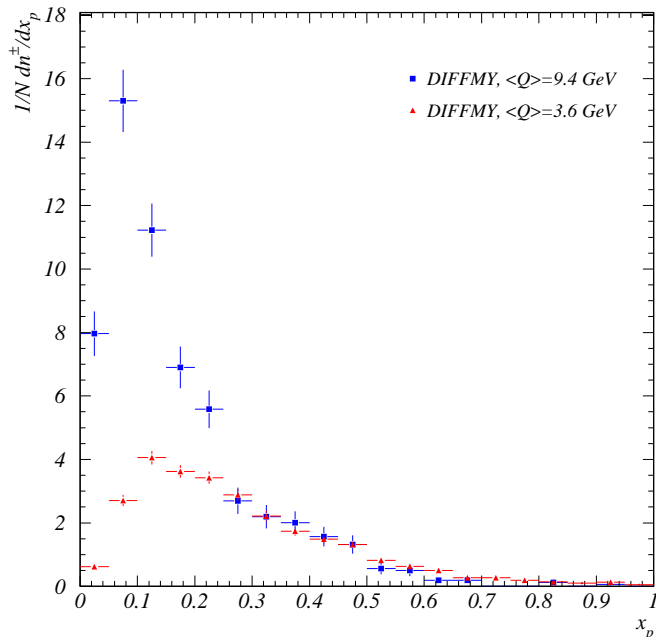


Figure 8.1: The fragmentation function, $1/N dn^\pm/dx_p$, of the DIFFMY event selection for the current hemisphere of the Breit frame (raw distributions and statistical errors only).

development and non-perturbative hadronisation. In this analysis we have integrated over parton and charged hadron varieties. An investigation of identified hadron fragmentation has been performed in [58].

Figure 8.1 shows the spectrum $D(x_p)$ for two different Q values for the DIFFMY event selection. As the available energy for fragmentation increases, the phase space for gluon radiation increases and the likelihood of observing a final state hadron with a large share of the initial parton momenta gets smaller. The function turns over as $x_p \rightarrow 0$ and becomes softer with increasing energy. These scaling violations have been studied in depth in [59].

To examine the turnover region the fragmentation function is recast in terms of the variable $\xi = \ln(1/x_p)$ and defined as

$$D^\pm(\xi) = (1/N) \times dn_{tracks}^\pm/d\xi. \quad (8.2)$$

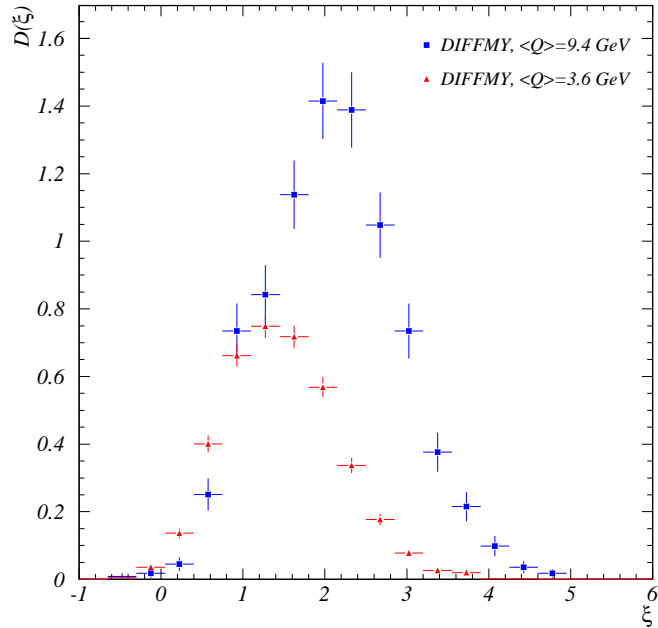


Figure 8.2: The fragmentation function, $D(\xi)$, of the DIFFMY event selection for the current hemisphere of the Breit frame (raw distributions and statistical errors only).

Figure 8.2 shows the fragmentation function, $D(\xi)$, for two different Q values for the DIFFMY event selection. Gluon coherence gives rise to a suppression of soft gluon radiation at wide angles in the parton cascade, without gluon coherence the spectra would develop a shoulder in the low momentum (large ξ) region.

8.2 Data Quality

Data Monte-Carlo Comparison

As before the data is corrected for detector acceptance and QED radiative effects. Figure 8.3 shows a comparison between uncorrected data and RAPGAP Monte-Carlo for the DIFFMY event selection for six different Q^2 bins; $12 < Q^2 < 15 \text{ GeV}$, $15 \rightarrow 20$, $20 \rightarrow 40$, $40 \rightarrow 60$, $60 \rightarrow 80$, and $80 \rightarrow 100$. The Monte-Carlo compares well to the data with a very good description of the shape of the fragmentation function.

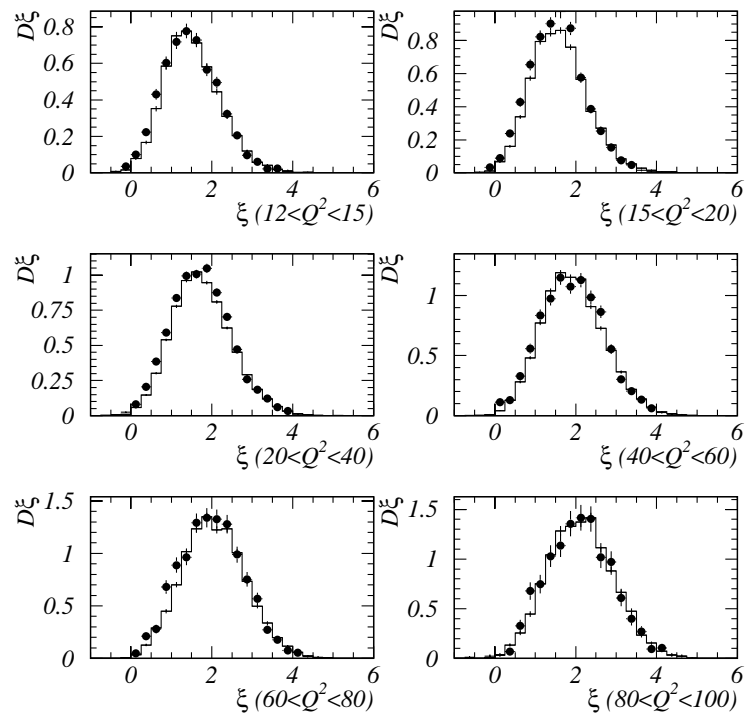


Figure 8.3: Comparison of uncorrected data and RAPGAP Monte-Carlo for the DIFFMY event selection (statistical errors only).

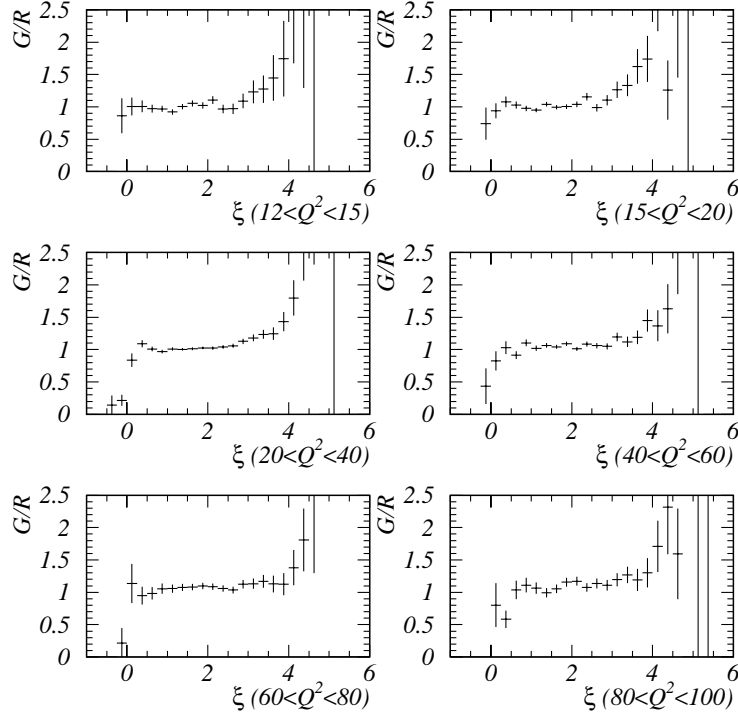


Figure 8.4: Acceptance correction factors applied to the data for the DIFFMY event selection (statistical errors only).

Correction Factors

Figure 8.4 shows the correction factors applied to the data for the DIFFMY rapidity distributions. Correction factors are small and their distribution flat in the area around the peak position, this is important for peak and width measurements of the fragmentation function. This is also the area where most of the tracks are, which is important for measurements of the average charged multiplicity $\langle n \rangle$.

Resolution and Purity

The resolution is defined as the difference between the generated and reconstructed track ξ . For each interval in ξ we assume that the distribution of the differences is a Gaussian and take its RMS value as the resolution. In figure 8.5 the resolution in ξ is shown as a function of ξ for each Q^2 bin. Over most of the distribution the resolution is smaller than the bin-width. Only in the first and last few intervals is the value of

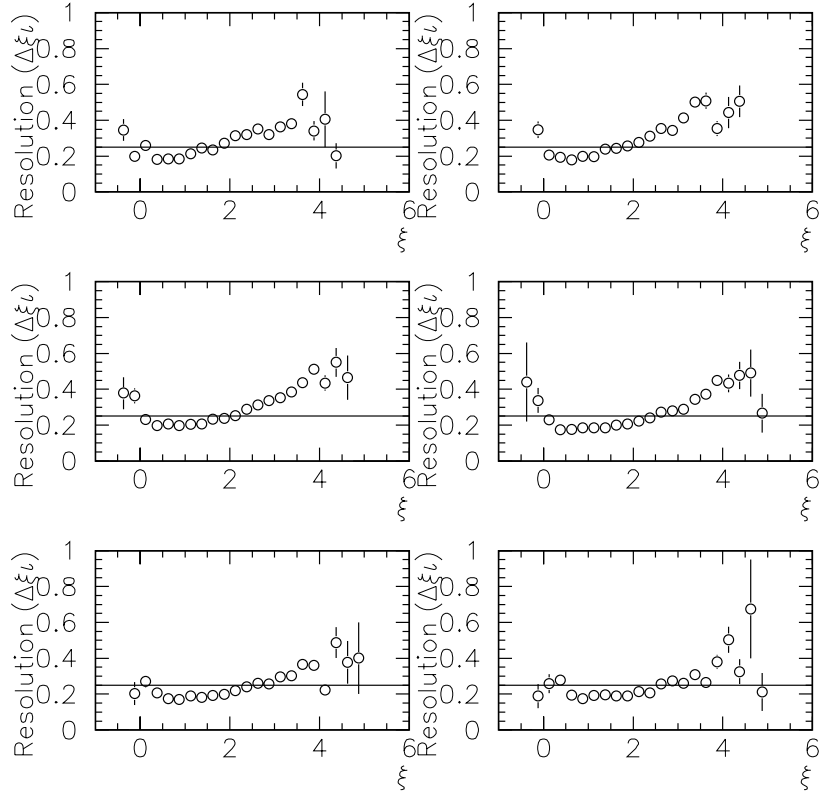


Figure 8.5: The resolution in ξ as a function of ξ for the DIFFMY event selection. The solid line shows the bin-width ($\xi \sim 0.25$) (statistical errors only).

the resolution larger than the bin-width.

The purity is defined as the proportion of tracks in a given analysis interval after simulation and reconstruction procedures that were generated in that interval. Figure 8.6 shows the purity of ξ , in general the purity is greater than 35%.

The results show high purity, good resolution and flat correction factors for all Q^2 bins for the DIFFMY selection. Comparisons for the other event selections show similar agreement. These findings provide evidence that the results presented below are reliable and accurate.

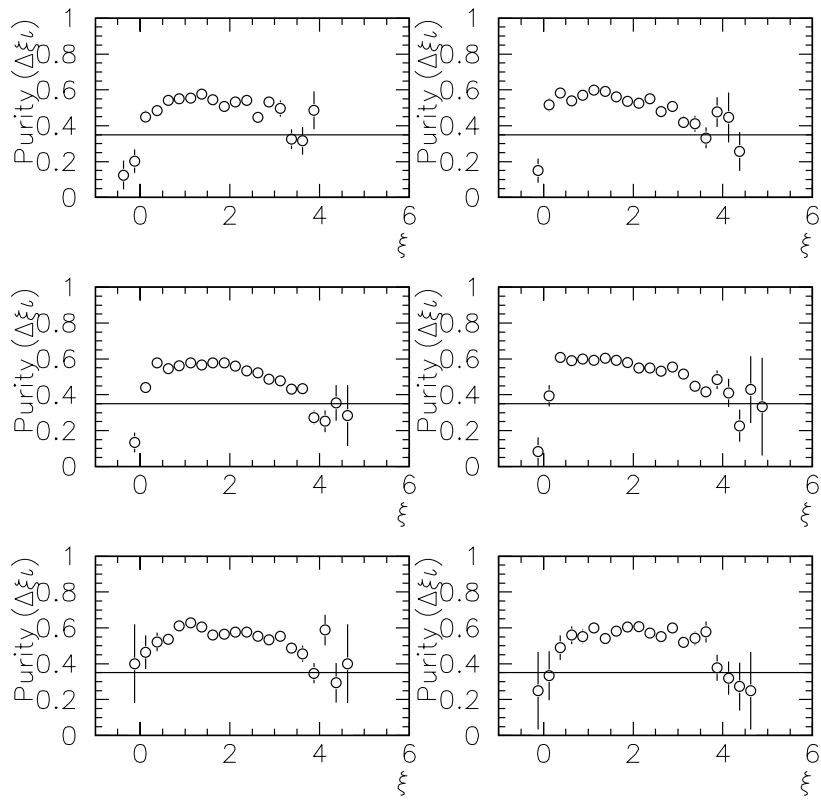


Figure 8.6: The purity in ξ as a function of ξ for the DIFFMY event selection. The solid line shows a minimum value for the purity of 35% (statistical errors only).

Systematic Errors

The errors for the average charged multiplicity are dominated by a correlated systematic error of $\sim 6\%$ associated with the SpaCal energy scale and a separate correlated error of $\sim 7\%$ from the fragmentation model dependence.

8.3 Average charged Multiplicity

The integrated area under the fragmentation function is the average charged multiplicity ($\langle n \rangle$) and is often called the zeroth moment of the fragmentation function. The solid line shown in the following plots is a parameterisation [60] of e^+e^- results for a single hemisphere. A reduction of $\sim 8\%$ has been made to the parameterisation to account for additional K^0 and Λ decays present in e^+e^- but not in ep .

New DIS results compared with Preliminary Results

The average charged multiplicity for preliminary¹ DIS and for DIS from this analysis is compared in figure 8.7. The preliminary DIS points (open crosses) are consistently above the new DIS points (solid stars). This difference is consistent with using a different energy calibration for the scattered electron, approximately a 1% increase in the energy scale produces a 7% increase in the average charged multiplicity. An error in the energy calibration is already included in the systematics.

Both distributions show a shortfall in multiplicity when compared to the e^+e^- parameterisation. In [49] this significant shortfall was explained by LO QCD processes present in ep but absent in e^+e^- interactions (see Chapter 6). Such higher order QCD processes lead to a depopulation of tracks in the current region or even an empty current region².

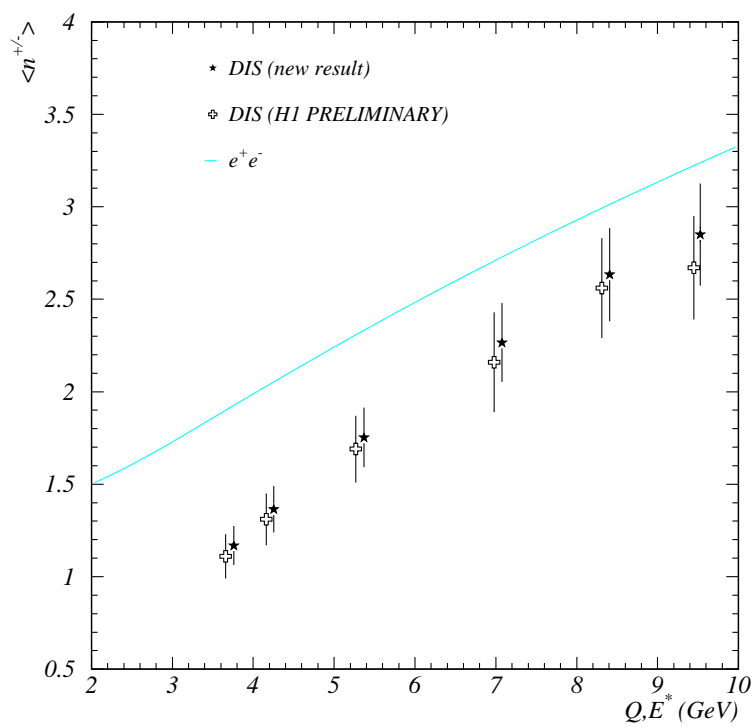


Figure 8.7: Comparison of Preliminary DIS results with the most recent (this analysis) DIS results for the $\langle n \rangle$. (statistical and systematic errors). The DIS data points have been shifted by 0.1 GeV for ease of comparison.

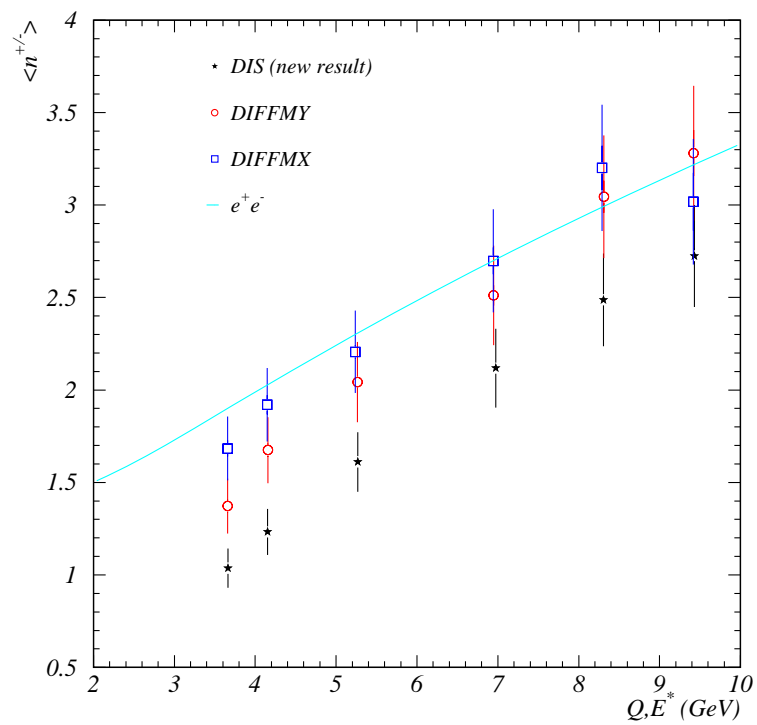


Figure 8.8: Data comparing $\langle n \rangle$ for DIS, DIFFMX and DIFFMY selections (statistical and systematic errors).

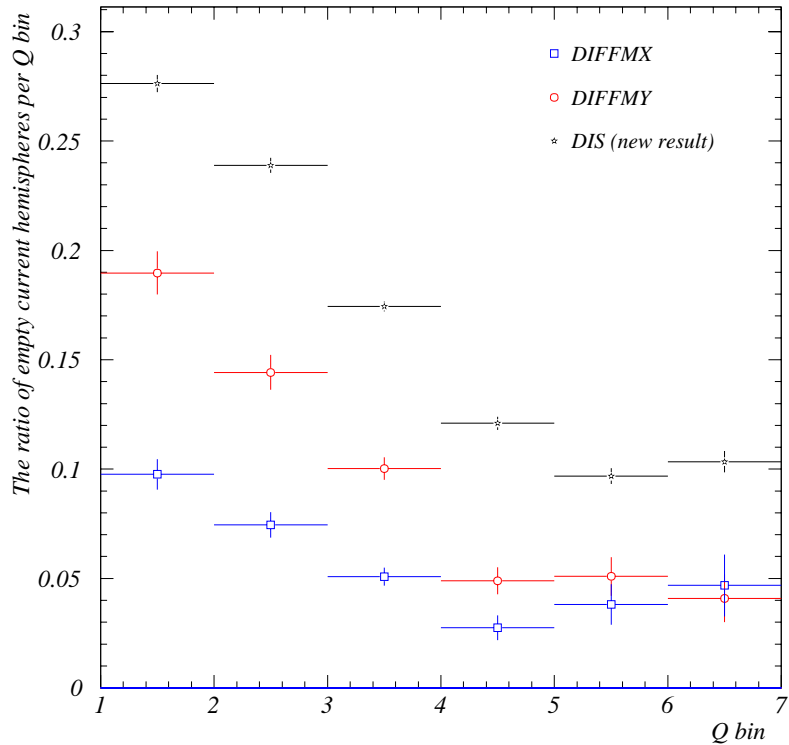


Figure 8.9: The ratio of events with an empty current hemisphere as a function of the Q^2 bin for DIS, DIFFMX and DIFFMY event selections. (statistical errors only)

Diffraction compared with DIS

Due to the gluonic nature of the pomeron and in analogy to the same processes that depopulates the current region in DIS events the initial expectation for diffraction was that the data would have a lower $\langle n \rangle$ than DIS. Figure 8.8 clearly shows that the opposite is true and that the diffractive distributions have a higher $\langle n \rangle$, it is also noticeable that the DIFFMX distribution has a result compatible with that of e^+e^- at an equivalent E^* .

Figure 8.9 show the ratio of events in each Q^2 bin with an empty current hemisphere. From figure 8.9 it would seem that the increased multiplicity in the diffractive distributions can be attributed predominantly to fewer empty current hemisphere events.

The reduction in empty current hemispheres can be attributed to two processes

¹Preliminary data points taken from [44].

²An empty current hemisphere has no measured hadronic activity in it.

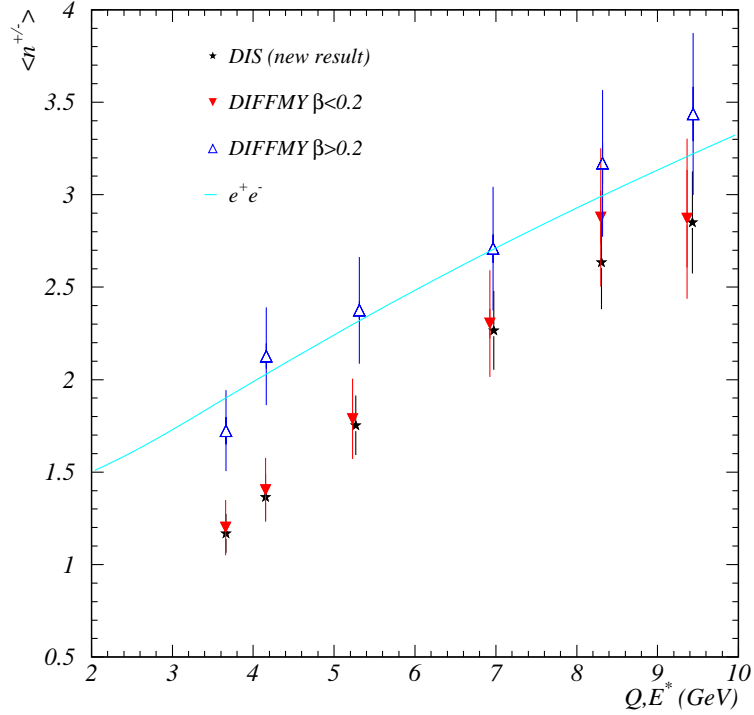


Figure 8.10: Comparison of $\langle n \rangle$ for DIFFMY $\beta < 0.2$ and DIFFMY $\beta > 0.2$. (statistical and systematic errors). The DIS data points have been shifted by 0.1 GeV for ease of comparison.

previously outlined in the last chapter. The decomposition of the cross section into a contribution from $q\bar{q}$ production at high β producing a more e^+e^- like multiplicity, and $q\bar{q}g$ production at low β which can be interpreted as BGF like events and which produce the empty current hemispheres. Additionally a kinematic effect which means for $Q > M_x$ ($\beta > 0.5$)³ it is kinematically forbidden to have an empty current hemisphere.

Figure 8.10 shows $\langle n \rangle$ in two different intervals of β . The results are consistent with $q\bar{q}g$ production dominating at low β producing a more DIS like behaviour and $q\bar{q}$ production dominating at high β and is closer to the e^+e^- behaviour with significantly fewer events with an empty current region. For $12 < Q^2 < 15$ ($60 < Q^2 < 80$) GeV^2 , 28% (10%) of events in the DIS selection have an empty current region, compared to

³For DIS the same requirement would be for $Q > W$ which is not possible.

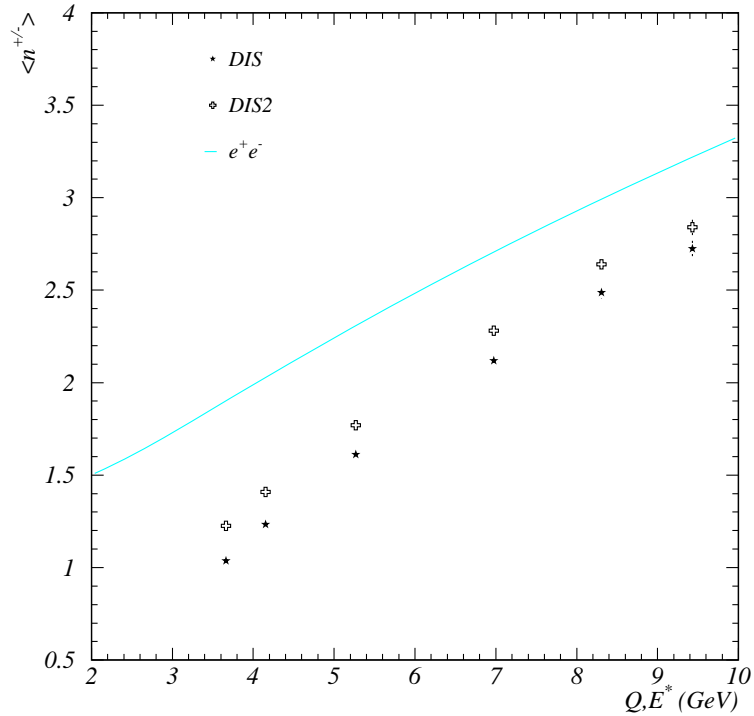


Figure 8.11: Comparison of $\langle n \rangle$ for two different definitions of deep-inelastic scattering, DIS ($egap > 0.5$ GeV) and DIS2 (\overline{DIFFMY}). (statistical errors only)

22% (7%) in the DIFFMY sample at low β and 8% (3%) at high β .

DIS compared with DIS2

Having seen that the DIFFMX selection has a higher $\langle n \rangle$ than that for DIFFMY we can understand the difference in figure 8.11 between DIS and DIS2. In the DIS2 event selection DIFFMY events (comprising 8% of the total) have been replaced by DIFFMX events which have a slightly higher multiplicity, this leads to an overall increase in multiplicity for DIS2 events when compared to DIS events.

8.4 Model comparisons

As with the rapidity spectra both the resolved pomeron model (Figure 8.12) (H1 fit 2) and the saturation model (figure 8.13) are able to describe the β dependence and

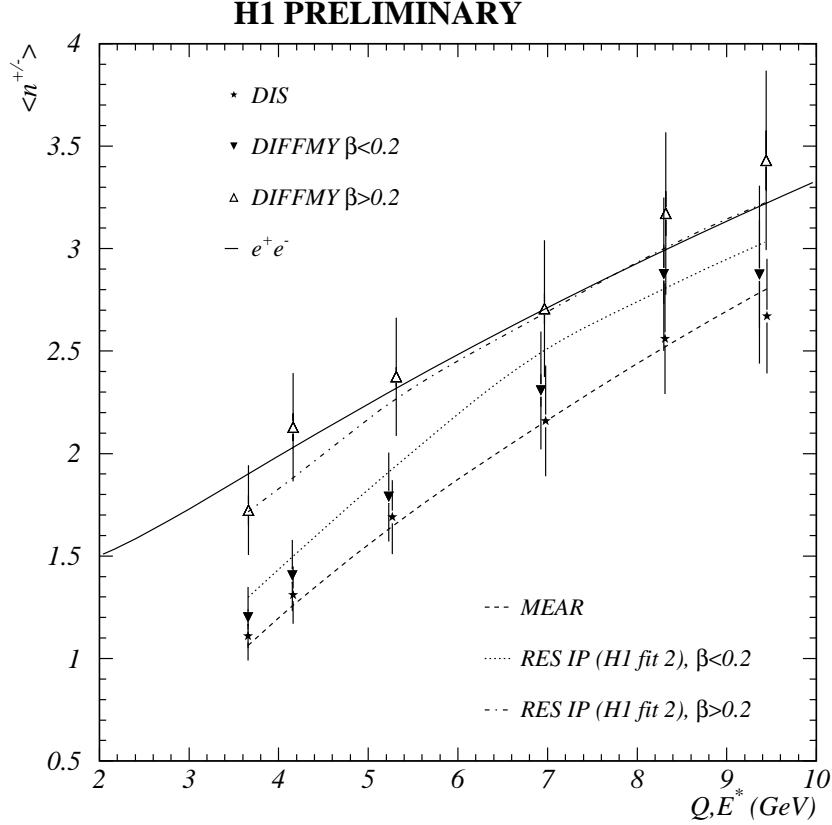


Figure 8.12: The averaged charged multiplicity as a function of the energy scale Q . The solid curve is a fit to many e^+e^- results as a function of the centre of mass energy E^* ($E^* = Q$), the dashed line a prediction for the MEAR Monte-Carlo for DIS events and the dotted and dashed-dotted lines comes from RAPGAP using the resolved IP model and the fit 2 parameterisation from H1.

the Q^2 evolution of the average charged multiplicity seen in the data although the resolved pomeron model appears to describe the data better. This is consistent with the results presented for the rapidity spectra.

8.5 Peak Position and Width of the Fragmentation Function

The Modified Leading Log Approximation (MLLA) [38] coupled with the hypothesis of Local Parton Hadron Duality (LPHD) [36][37] predicts that in the region of the

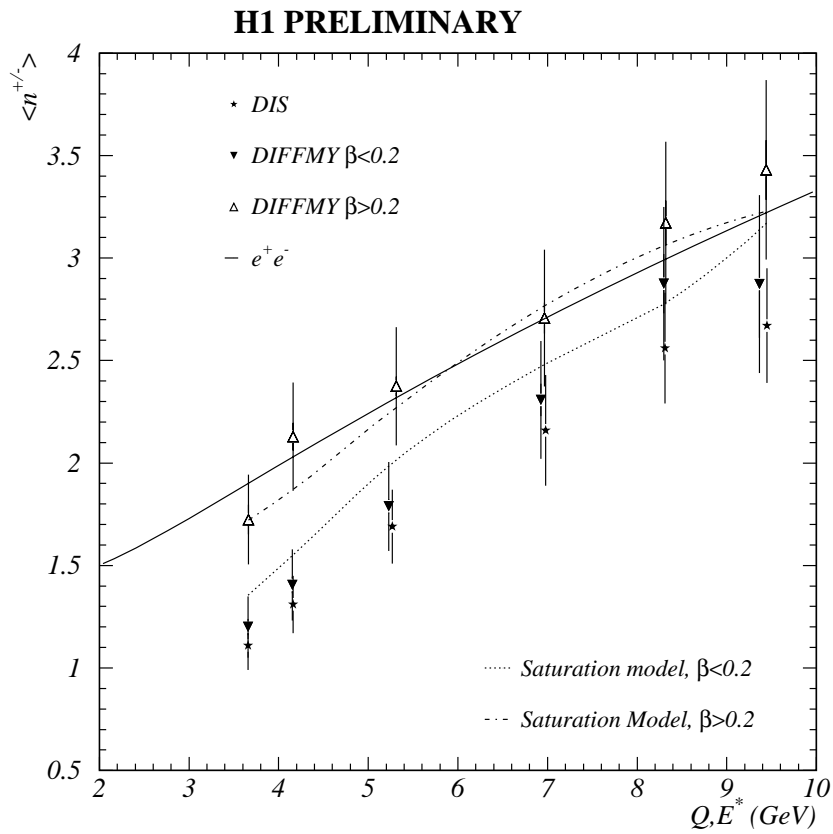


Figure 8.13: The average charged multiplicities as a function of the energy scale Q . The data is compared with a prediction of the saturation model.

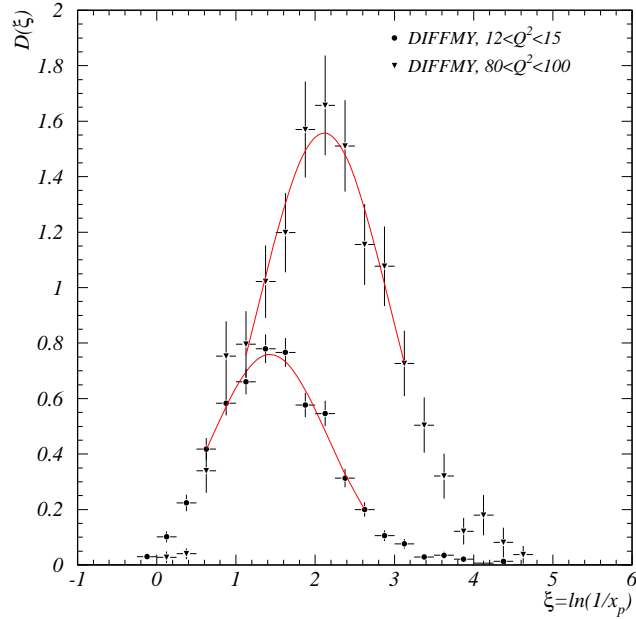


Figure 8.14: The fragmentation function, $D(\xi)$, for the DIFFMY event selection after acceptance corrections together with Gaussian fits in the region of the peak. (corrected distributions and statistical errors only)

peak of the inclusive hadronic ξ distribution, the shape is approximately Gaussian. Figure 8.14 shows Gaussian fits to the fragmentation function for two different intervals in Q^2 and shows that the same property holds for the diffractive subset of events.

The MLLA also gives a prediction for the energy behaviour of the peak and width of this Gaussian (the first and second moments of the fragmentation function respectively),

$$\xi_{peak} = 0.5U + c_2\sqrt{U} + O(1) \quad (8.3)$$

$$\xi_{width} = \sqrt{\frac{U^{3/2}}{2c_1}} \quad (8.4)$$

Here $U = \ln(Q/\Lambda_{eff})$, where Λ_{eff} is an effective scale parameter, c_1 and c_2 are constants dependent on the number of excited flavours and colours in QCD, and $O(1)$

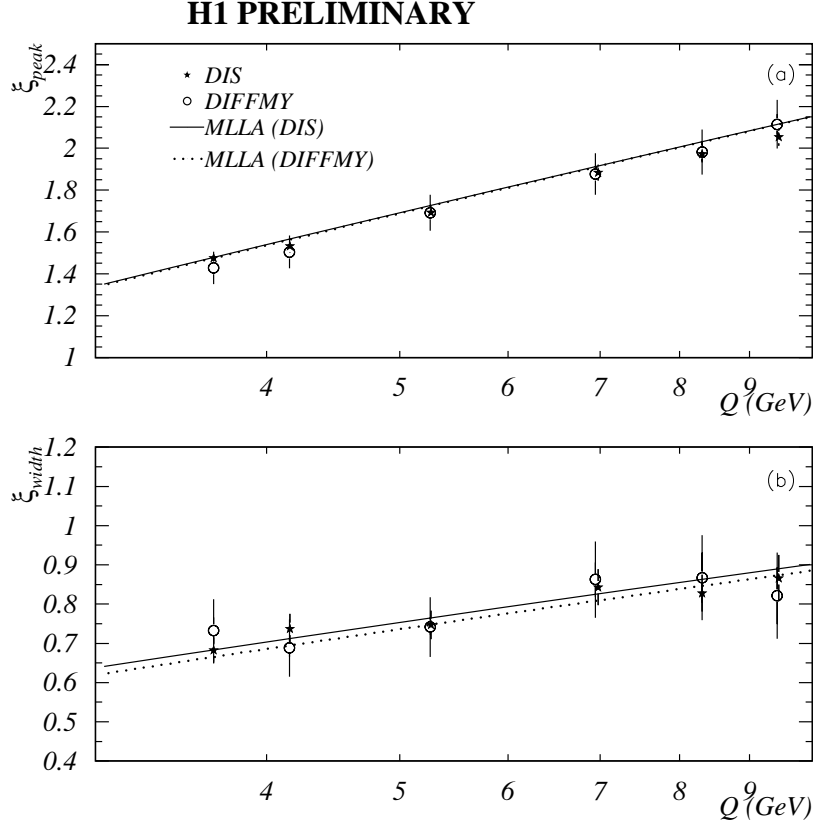


Figure 8.15: The energy evolution of (a) the peak position and (b) the width of the fragmentation function for both DIS and DIFFMY selections. The solid (dashed) line is the simultaneous fit of the MLLA parameterisation to DIS (DIFFMY) data.

is a slowly varying function of energy containing all QCD diagrams beyond leading order. This term is assumed to be constant in this analysis.

Figure 8.15 summarises the energy evolution of the fragmentation function. The solid (dashed) line is the simultaneous fit to the peak position and width of the MLLA parameterisation for the DIS (DIFFMY) data selection which yields a result of $\Lambda_{eff} = 0.21 \pm 0.04$ (0.19 ± 0.03) and $O(1) = -0.42 \pm 0.12$ (-0.49 ± 0.12). The χ^2 of Gaussian fits to the fragmentation function and of the MLLA fit are all less than 2 per degree of freedom.

It can be seen clearly that both DIS and DIFFMY distributions are compatible with each other, a demonstration of quark fragmentation universality (i.e that a quark ejected from a \mathbb{P} behaves in the same manner as one ejected from a proton).

8.6 Summary

Differences with previous results for the average charged multiplicity can be understood as a change most likely related to the energy calibration of the scattered electron in the SpaCal calorimeter as was observed for the rapidity spectra.

- The increased multiplicity of the diffractive selections when compared with the DIS distributions is predominantly related to the decrease in the number of empty current hemisphere events. The number of empty current hemisphere events in DIS have previously been shown to be related to LO QCD effects.
- When the DIFFMY selection is split into high and low β , effects consistent with e^+e^- at high β and LO QCD (BGF and QCD Compton) at low β are observed. This effect is consistent with the different restriction in phase space due to the correlation between β and M_X (as was also seen for the rapidity spectra).
- Comparison with a variety of model shows that the resolved pomeron model using H1 fit 2 (or 3) again provides the best description of the data.
- When higher orders of the fragmentation function are studied, the DIS and DIFFMY selections are found to agree very well with each other and with a MLLA/LPHD prediction, providing a robust test of quark fragmentation universality.

Normalisation differences of the track multiplicity ($\langle n \rangle$), resulting from effects unrelated to the fragmentation process, do not effect the shape of the fragmentation functions higher moments. Unfortunately due to limited statistics and poor resolution in the tails of the fragmentation function it is not possible to study higher moments such as skewness and kurtosis in this analysis. To extend the analysis of quark fragmentation universality the shape of other distribution must be studied.

Q^2 GeV	DIS	DIFFMX	DIFFMY
$12 < Q^2 < 15$	$1.17 \pm 0.02 \pm 0.11$	$1.68 \pm 0.04 \pm 0.17$	$1.37 \pm 0.04 \pm 0.14$
$15 < Q^2 < 20$	$1.37 \pm 0.02 \pm 0.12$	$1.92 \pm 0.05 \pm 0.19$	$1.67 \pm 0.04 \pm 0.17$
$20 < Q^2 < 40$	$1.75 \pm 0.01 \pm 0.16$	$2.21 \pm 0.04 \pm 0.22$	$2.04 \pm 0.03 \pm 0.20$
$40 < Q^2 < 60$	$2.27 \pm 0.02 \pm 0.21$	$2.70 \pm 0.07 \pm 0.27$	$2.51 \pm 0.05 \pm 0.25$
$60 < Q^2 < 80$	$2.63 \pm 0.03 \pm 0.24$	$3.20 \pm 0.12 \pm 0.32$	$3.05 \pm 0.09 \pm 0.31$
$80 < Q^2 < 100$	$2.85 \pm 0.04 \pm 0.26$	$3.02 \pm 0.16 \pm 0.30$	$3.28 \pm 0.12 \pm 0.33$

Table 8.1: The $\langle n \rangle$ as a function of Q^2 for the DIS, DIFFMX and DIFFMY selections. The errors are the statistical error and then systematic error.

Q^2 GeV	DIFFMY $\beta > 0.2$	DIFFMY $\beta < 0.2$
$12 < Q^2 < 15$	$1.73 \pm 0.07 \pm 0.21$	$1.20 \pm 0.04 \pm 0.14$
$15 < Q^2 < 20$	$2.13 \pm 0.07 \pm 0.26$	$1.40 \pm 0.04 \pm 0.17$
$20 < Q^2 < 40$	$2.37 \pm 0.05 \pm 0.29$	$1.79 \pm 0.03 \pm 0.22$
$40 < Q^2 < 60$	$2.71 \pm 0.08 \pm 0.33$	$2.30 \pm 0.08 \pm 0.28$
$60 < Q^2 < 80$	$3.17 \pm 0.11 \pm 0.38$	$2.88 \pm 0.14 \pm 0.35$
$80 < Q^2 < 100$	$3.44 \pm 0.15 \pm 0.41$	$2.88 \pm 0.26 \pm 0.35$

Table 8.2: The $\langle n \rangle$ as a function of Q^2 for the low and high β DIFFMY selections. The errors are the statistical error and then systematic error

Q^2 GeV	DIS ξ_{peak}	DIS ξ_{width}	DIFFMY ξ_{peak}	DIFFMY ξ_{width}
$12 < Q^2 < 15$	$1.42 \pm 0.02 \pm 0.07$	$0.77 \pm 0.03 \pm 0.09$	$1.43 \pm 0.03 \pm 0.07$	$0.73 \pm 0.03 \pm 0.07$
$15 < Q^2 < 20$	$1.52 \pm 0.01 \pm 0.08$	$0.73 \pm 0.02 \pm 0.08$	$1.50 \pm 0.02 \pm 0.08$	$0.69 \pm 0.02 \pm 0.07$
$20 < Q^2 < 40$	$1.70 \pm 0.009 \pm 0.09$	$0.77 \pm 0.01 \pm 0.09$	$1.69 \pm 0.02 \pm 0.09$	$0.74 \pm 0.02 \pm 0.07$
$40 < Q^2 < 60$	$1.90 \pm 0.01 \pm 0.10$	$0.84 \pm 0.02 \pm 0.09$	$1.88 \pm 0.03 \pm 0.09$	$0.86 \pm 0.04 \pm 0.09$
$60 < Q^2 < 80$	$1.99 \pm 0.02 \pm 0.10$	$0.85 \pm 0.02 \pm 0.09$	$1.98 \pm 0.04 \pm 0.1$	$0.87 \pm 0.06 \pm 0.09$
$80 < Q^2 < 100$	$2.07 \pm 0.02 \pm 0.10$	$0.85 \pm 0.03 \pm 0.09$	$2.11 \pm 0.05 \pm 0.11$	$0.82 \pm 0.07 \pm 0.08$

Table 8.3: The energy evolution of the peak position and width of the fragmentation function for both DIS and DIFFMY selections. The errors are the statistical error and then systematic error

Chapter 9

Transverse Momentum Spectra

9.1 Introduction

In the previous chapters we studied the rapidity spectra and the fragmentation function of charged hadrons. Both of these quantities are dominated by the longitudinal momentum of the track. It is a natural extension of the analysis to study the transverse momentum spectra (p_t) of charged hadrons.

The distribution $\frac{1}{N}dn_{tracks}^{\pm}/dp_t^2$ is plotted as a function of p_t (figure 9.1) for charged hadrons in the current region only. Technically this is achieved by weighting each track with $\frac{1}{2p_t}$. The data is fitted by an exponential of the form

$$a * e^{-bm_t} \tag{9.1}$$

in the low p_t region, $0.15 < p_t < 0.75$ GeV, where m_t is known as the transverse mass and is equal to $\sqrt{p_t^2 + m_{\pi}^2}$. This is shown by the dashed line in figure 9.1. Equation 9.1 is very similar to the tunnelling probability, equation 4.1, used in the string hadronisation model. In string hadronisation the production of $q\bar{q}$ pairs from the vacuum can be described by a tunnelling probability. The result is a Gaussian transverse momentum distribution (from the Fermi motion of the quarks).

The exponential fit fails to describe the data for $p_t > 1.0$. At high p_t the distribu-

tion is expected to be dominated by p_t from the hard interaction. A power law fit of the form

$$A \times (1 + p_t/P_{t0})^{-m} \tag{9.2}$$

is thus made in the region $1.0 < p_t < 3.0$ GeV, where $P_{t0} = 0.75$ GeV is taken from [61]. Due to the large intervals of p_t used and the steply falling p_t spectra the fits must take into account ‘bin centre’ corrections (i.e the centre of gravity of the bin is not the same as the centre of the bin). This is done by fitting to the integrated contents of the bins. Given that at large p_t the hadronic momenta are dominated by the parent parton, the value of m is a measure of the size of the interaction, where $m = 4$ would indicate point like (Rutherford) scattering. The function is defined such that A represents the normalised cross section as $p_t \rightarrow 0$. The power law is shown by the solid line in figure 9.1. Derived values of parameters will be discussed later in this chapter.

9.2 Data Quality

Data Monte-Carlo Comparison

As before, the data is corrected for detector acceptance and QED radiative effects. To be accurate this requires a fair description of the data by Monte-Carlo. Figure 9.2 shows a comparison between uncorrected data and RAPGAP Monte-Carlo for the DIFFMY event selection for six different Q^2 bins. The Monte-Carlo compares well to the data with a very good description of the p_t spectra. There is a similar agreement for the comparison between DIS and MEAR (not shown).

Correction Factors

The correction factors applied to the data for the DIFFMY selection is shown in figure 9.3. Correction factors are of the order of unity and their distribution flat

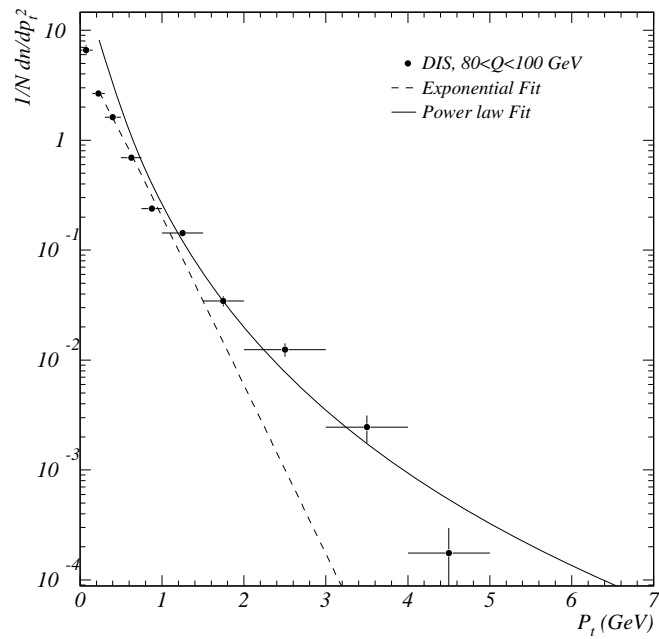


Figure 9.1: The transverse momentum spectra, $\frac{1}{N} \frac{dn_{tracks}^{\pm}}{dp_t^2}$, as a function of p_t for charged hadrons in the current hemisphere of the Breit frame (statistical errors only). The fits shown are made within restricted p_t ranges but plotted over the whole p_t range.

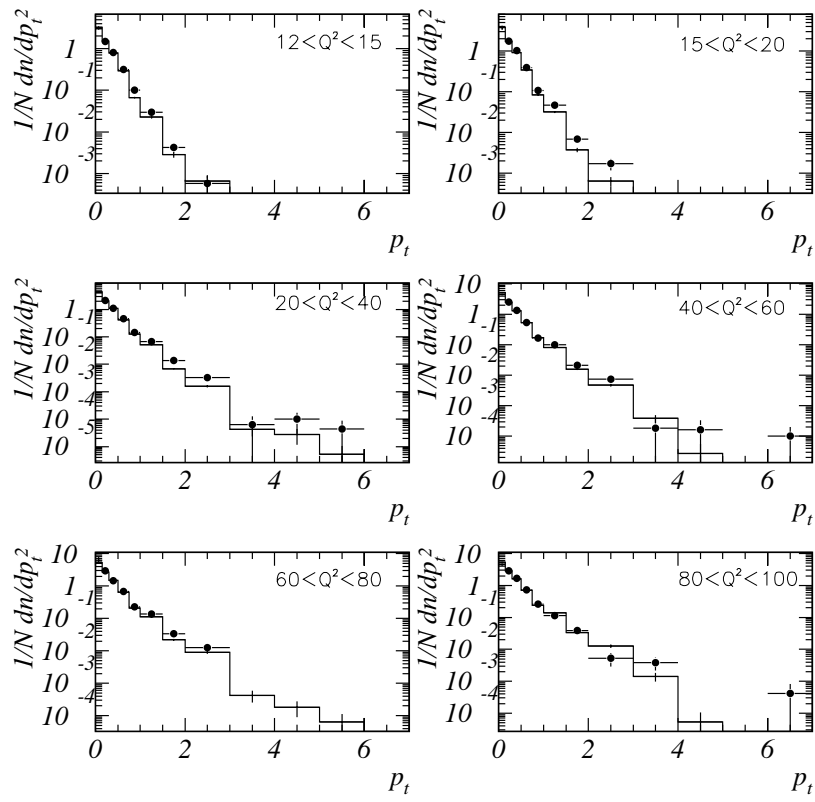


Figure 9.2: Comparison of uncorrected data and RAPGAP Monte-Carlo for the DIFFMY event selection. (statistical errors only)

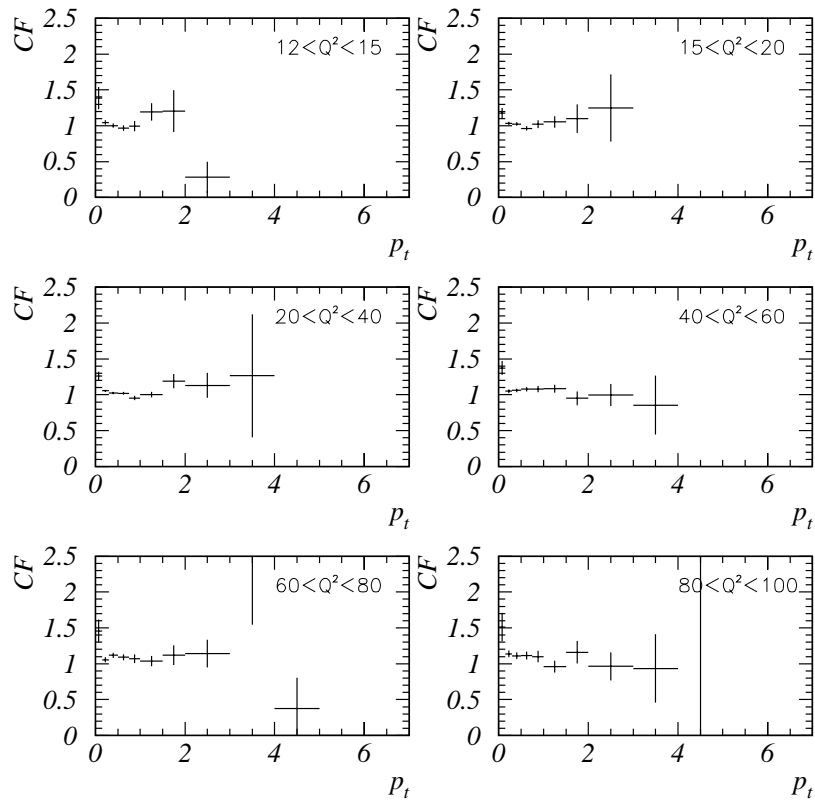


Figure 9.3: Acceptance correction factors applied to the data for the DIFFMY event selection. (statistical errors only)

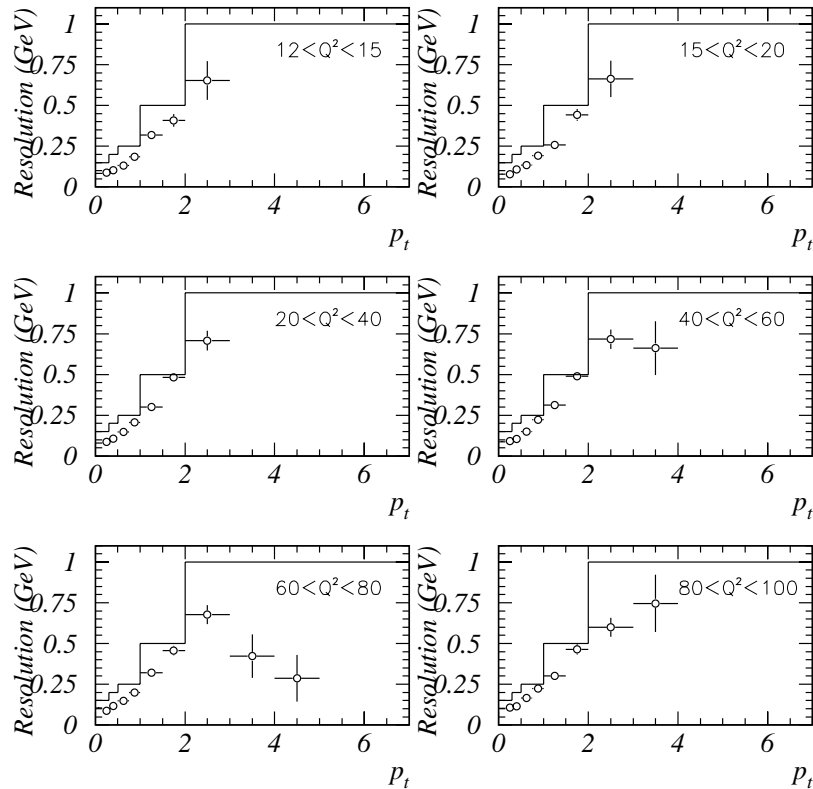


Figure 9.4: The resolution of p_t as a function of reconstructed p_t for the DIFFMY event selection (RAPGAP Monte-Carlo). The solid line shows the bin-width employed. (statistical errors only)

($\sim 1.0 \pm 0.1$) in the regions where the exponential and power law fits are made. Similar correction factors are seen for the DIS selection.

Resolutions and purity

The resolution is defined as before as the difference between the generated and reconstructed track p_t . For each interval in p_t the RMS value is taken as an estimate of the resolution since the distribution of differences is approximately Gaussian. In figure 9.4 the resolution in p_t is shown as a function of p_t for each Q^2 bin. Over most of the distribution the resolution is smaller than the bin-width.

The purity is defined as the proportion of tracks in a given analysis interval after simulation and reconstruction procedures that remain in that interval. Figure 9.5

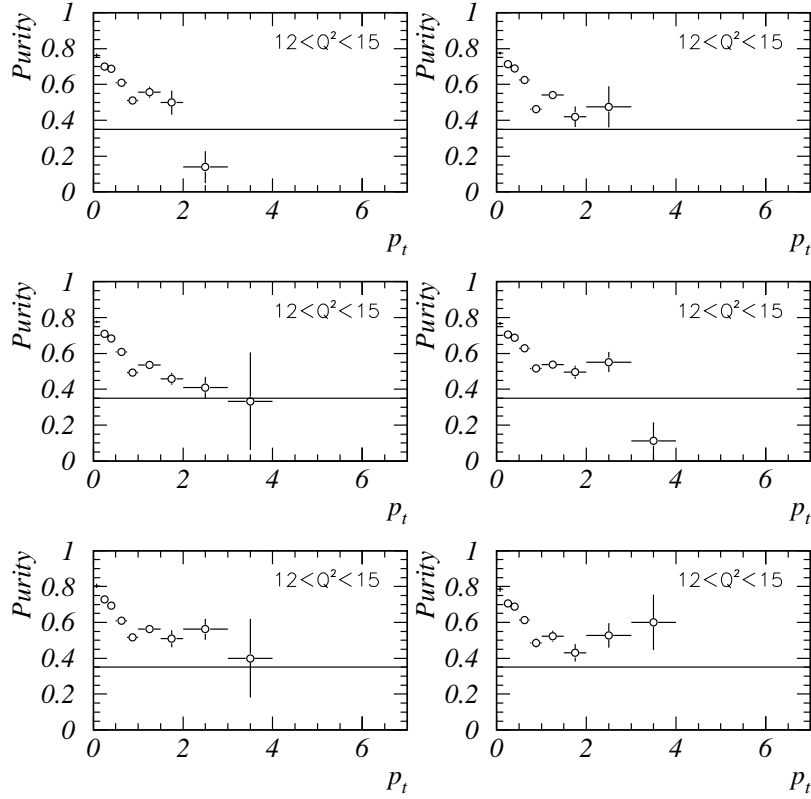


Figure 9.5: The purity in p_t as a function of reconstructed p_t for the DIFFMY event selection (RAPGAP Monte-Carlo). The solid line shows an arbitrary minimum value for the purity of 35%. (statistical errors only)

shows the purity of p_t , which in general, is greater than 35%.

Systematic errors

The systematic error on b is dominated by a correlated $\sim 3\%$ uncertainty from the fragmentation model dependence. For the value of m the dominant systematic error is a similar correlated error of $\sim 6\%$ from the same source.

9.3 Results

A summary of the results can be found in Tables 9.1 and 9.2.

Figure 9.6 shows the evolution with Q of values of b from the exponential fits

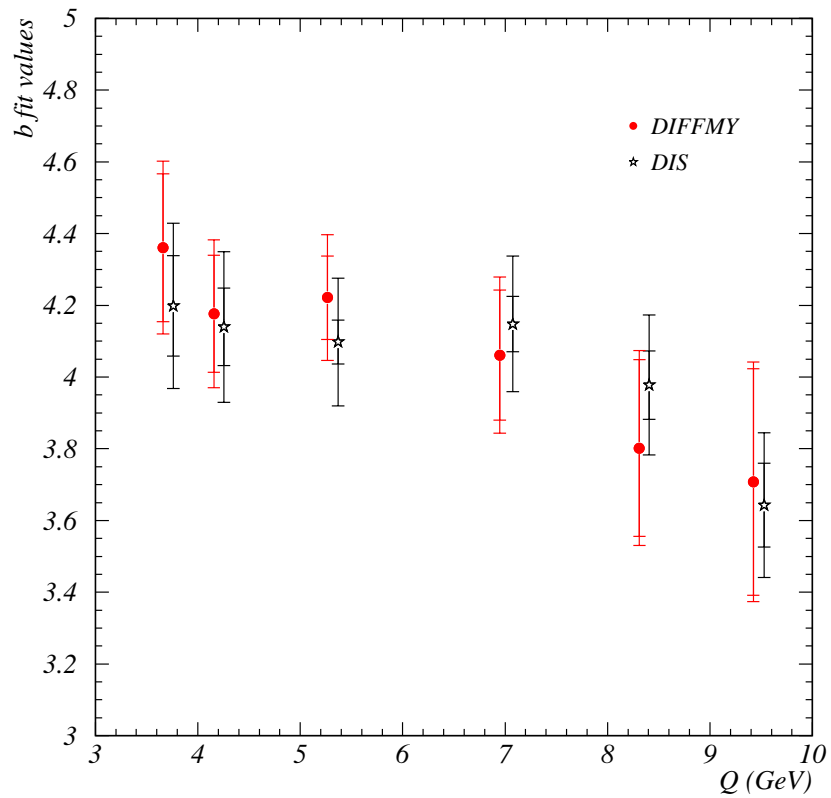


Figure 9.6: The b values of the exponential fits as a function of Q for DIS (stars) and DIFFMY (open triangles). The DIS data points have been shifted to the right by 0.1 GeV for ease of comparison. The inner error bars are statistical and outer error bars also include systematic errors added in quadrature.

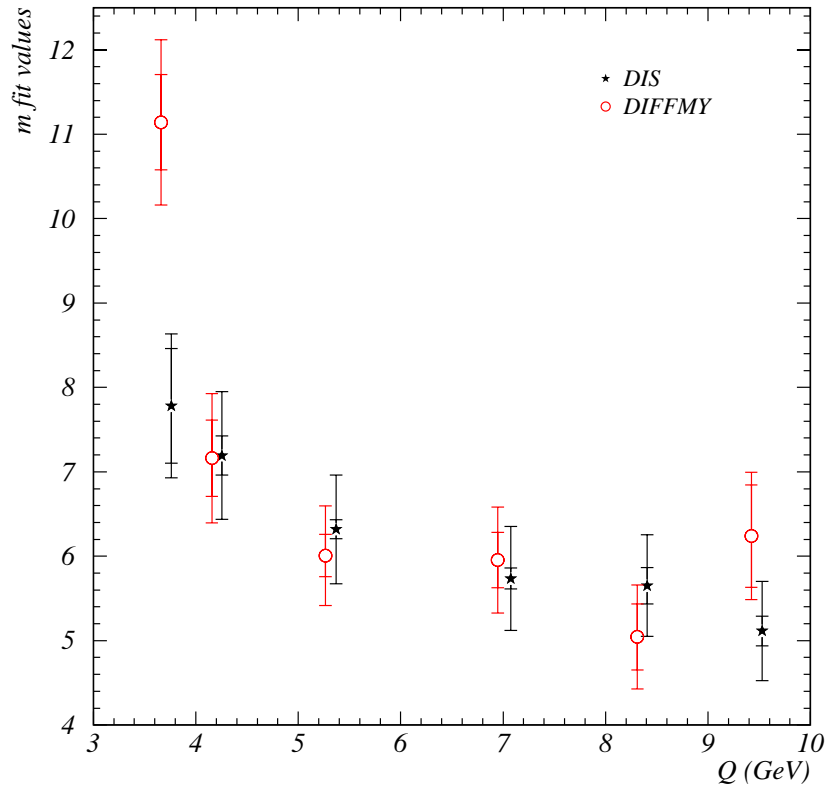


Figure 9.7: The m values of the power law fits as a function of Q for DIS (stars) and DIFFMY (open triangles). The DIS data points have been shifted to the right by 0.1 GeV for ease of comparison. The inner error bars are statistical and outer error bars also include systematic errors added in quadrature.

(equation 9.1) made in the region $0.15 < p_t < 0.75$ GeV for DIS and DIFFMY event selections. Results from the two different event selections are consistent with each other. The results shows a slow drop in the value of b with Q . The small Q dependence observed for the value of b is consistent with that observed in [2] but the actual values are consistently lower by one to two units. When the same fitting range as that analysis is used similar values for b are observed but with a much worse χ^2 . If we interpret b as related to the tunnelling probability then the same Q dependence seen in DIS and DIFFMY results demonstrates quark fragmentation universality. The small Q dependence seen in b shows that the hadronisation process is independent from the hard scale Q (i.e the hard scattering process).

Figure 9.7 shows the evolution with Q of values of m from the power law fits (equation 9.2) made in the region $1.0 < p_t < 3.0$ GeV for DIS and DIFFMY event selections. Apart from the lowest Q interval (which has one bin of very low purity) both DIS and DIFFMY results are consistent with each other. The results show a steady fall in the value of m with Q . The interpretation of the result of figure 9.7 shows that as Q increases smaller scales are able to be resolved.

It is possible to calculate the weighted average of the A values from table 9.2, for DIS this equals 63 ± 9 GeV⁻² and for DIFFMY 61 ± 19 GeV⁻² (statistical error only). These results show that again the DIS and DIFFMY distributions are in good agreement with each other. It is also obvious that the calculated means are consistent with almost all the individual Q^2 points, indicating that while the cross-section itself changes hugely with Q , the differential values as $P_t \rightarrow 0$ remains constant.

It should be noted that there is a correlation between between A , p_{t0} , and m . The value of p_{t0} has been fixed at 0.75 but other values in the range 0.25 – 2.0 were found to give reasonably good fits. If the value of p_{t0} is increased from 0.25 to 2.0 the weighted average of A for DIS decreases from 106 ± 15 to 52 ± 8 and similarly for DIFFMY. Using different values of P_{t0} results in different values of A but they are still constant as a function of Q . So changing p_{t0} does not change any of the conclusions made above about the evolution of m , A or the agreement between DIS and DIFFMY.

Figure 9.8 displays the results of three different fits to the evolution of m with Q ; a linear fit, an exponential fit of the form $\exp(a - bQ)$, and a power law of the form $4 + a(1 + Q)^{-b}$. All three fits are able to describe the data with $\chi^2 < 2$, even if the fits are made with statistical errors only (inner error bars on data points). From these results it is not possible to conclude how the p_t spectra will evolve at higher Q although the power law fit looks like it gives the best description of the data. Further data is needed at higher Q in order to determine which type of evolution will describe the data.

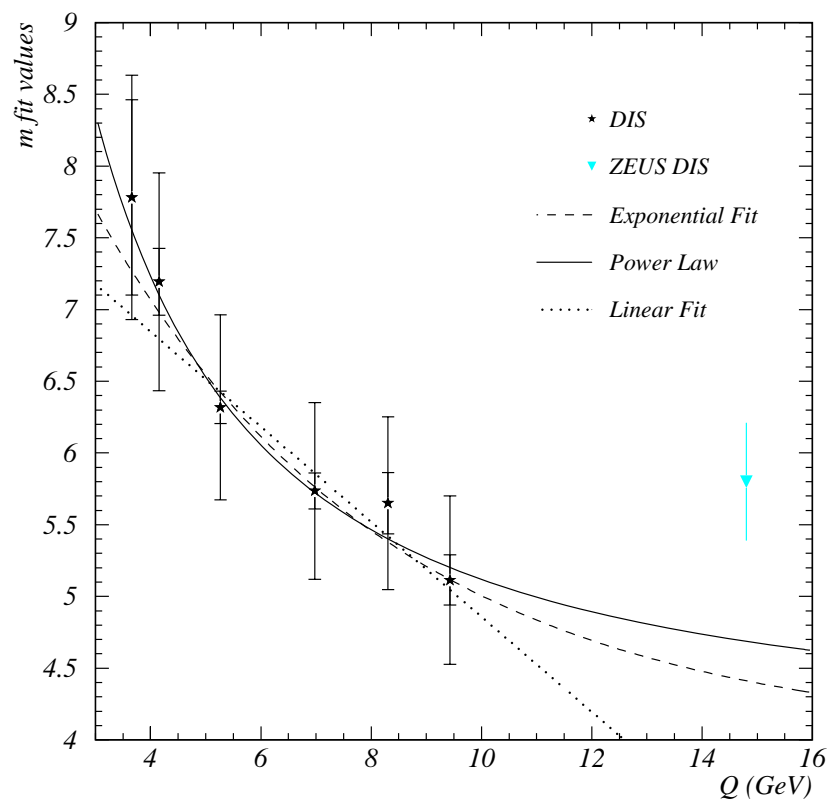


Figure 9.8: The m values of the power law fits as a function of Q for DIS only. Also shown are three different fits to the data. The inner error bars are statistical and outer error bars also include systematic errors added in quadrature.

Q^2 GeV	b (DIS)	χ^2	b (DIFFMY)	χ^2
$12 < Q^2 < 15$	$4.19 \pm 0.16 \pm 0.17$	1.4	$4.35 \pm 0.20 \pm 0.13$	0.2
$15 < Q^2 < 20$	$4.23 \pm 0.12 \pm 0.17$	0.4	$4.17 \pm 0.16 \pm 0.13$	4.4
$20 < Q^2 < 40$	$4.08 \pm 0.07 \pm 0.16$	3.5	$4.22 \pm 0.12 \pm 0.13$	0.3
$40 < Q^2 < 60$	$4.13 \pm 0.09 \pm 0.17$	0.3	$4.06 \pm 0.18 \pm 0.12$	0.03
$60 < Q^2 < 80$	$3.92 \pm 0.12 \pm 0.16$	0.0002	$3.82 \pm 0.25 \pm 0.11$	0.4
$80 < Q^2 < 100$	$3.58 \pm 0.14 \pm 0.14$	2.5	$3.70 \pm 0.32 \pm 0.11$	0.2

Table 9.1: Results from the exponential fits to the p_t spectra of the DIS and DIFFMY selections. The errors are the statistical error and then systematic error

9.4 Summary

Results from studies of the evolution of shape of the p_t spectra of charged particles in the current region of the Breit frame from H1 have been presented.

- Exponential fits describe the low p_t region. The slope parameter, b , shows little evolution in Q , this is consistent with a hadronisation process independent of the hard scattering process. Results for both DIS and DIFFMY selections are in agreement.
- Power law fits have been made to the high p_t region. The parameter m (related to the size of the interaction) gets smaller at Q increases, this is consistent with being able to resolve a smaller scale at larger Q . Values of m and the weighted average of parameter A are in agreement for both DIS and DIFFMY selections.
- Speculative attempts to study the evolution of m with Q were not able to distinguish between linear, exponential or a power law form to the evolution more data at higher Q is needed.

These results complement the results from studies of the fragmentation function in supporting the concept of quark fragmentation universality for diffractive and non-diffractive processes.

Q^2 GeV	m (DIS)	A	χ^2	m (DIFFMY)	A	χ^2
$12 < Q^2 < 15$	$7.78 \pm 0.40 \pm 0.75$	77 ± 48	0.06	$11.1 \pm 0.44 \pm 0.88$	1317 ± 656	3.15
$15 < Q^2 < 20$	$7.19 \pm 0.27 \pm 0.71$	100 ± 22	0.56	$7.15 \pm 0.48 \pm 0.60$	107 ± 45	0.000
$20 < Q^2 < 40$	$6.32 \pm 0.14 \pm 0.63$	68 ± 7	6.48	$6.01 \pm 0.26 \pm 0.53$	55 ± 13	3.5
$40 < Q^2 < 60$	$5.73 \pm 0.15 \pm 0.60$	61 ± 7	0.006	$5.95 \pm 0.34 \pm 0.53$	81 ± 26	0.02
$60 < Q^2 < 80$	$5.65 \pm 0.17 \pm 0.58$	72 ± 15	0.71	$5.04 \pm 0.42 \pm 0.45$	51 ± 19	0.1
$80 < Q^2 < 100$	$5.11 \pm 0.21 \pm 0.55$	51 ± 9	0.1	$6.23 \pm 0.52 \pm 0.54$	113 ± 65	5.7

Table 9.2: Results from the power law fits to the p_t spectra of the DIS and DIFFMY selections. The errors are the statistical error and then systematic error except for A where only the statistical error is given.

Conclusions

This thesis has presented various studies of the fragmentation properties of charged particles in diffractive and non-diffractive DIS. Where possible results have been compared with previous non-diffractive analyses that used different selection criteria and shown to agree. In general the results agree with the expectation from QCD (verified by comparison with DIS data and Monte-Carlo Models).

Comparisons between diffractive and non-diffractive results of the fragmentation function and p_t spectra support the concept of quark fragmentation universality. In distributions where differences were seen (rapidity spectra and average charged multiplicity) these differences can be understood as resulting from phase space differences (M_x) and from the different physics involved in diffraction.

Comparisons with various models of diffraction have shown that the resolved pomeron model using fit 2 (or 3) provides the best description of the diffractive data. Other models though are able to describe the quantitative behaviour of the diffractive distributions.

The energy evolution of the peak and widths of the fragmentation function for both diffractive and non-diffractive DIS agree and are described by the Modified Leading Log Approximation (MLLA).

The p_t spectra for both diffractive and non-diffractive DIS can be described by two simple fits with similar parameters; an exponential at low p_t to describe hadronisation and a power law at higher p_t to describe the hard interaction.

Acknowledgments

First I would like to thank my supervisor Graham Thompson for the freedom and time he has given me.

From the Flat; Thanks to Rich (for his driving), Mark (F) and Calixe for moving in and out at the right times.

From QMW; Thanks to Rob for his impressions. Thanks to Keith for teaching me to be SpaCal expert. Thanks to Dave (K) for his several thousand lines of fortran and for moving jobs. Thanks to Paul for not moving jobs. Thanks to John (T) for the music. Thanks to Dan (A) for leaving physics and making lots of money. Thanks to Ed for going to Brazil (at least we didn't have to put up with you for three weeks). Also thanks to Caroline, Martin, John (B), Hue, Richard (P), Dave (M), Mark (W) and anybody else who plays footy on Wednesday.

From DESY; Thanks to Dave (L) ,Glen , Mike, and John (S) for many many random words, and to Paul (N) for some useful words.

From Home; Thanks to Mum (for the warnings about academics), Dad, Catherine, Immy and the little ones for making life more fun.

I should also acknowledge PPARC for their financial support.

Bibliography

- [1] HERA, A Proposal for a Large Electron-Proton Colliding Beam Facility at DESY. DESY 81-10, 1981.
- [2] H1 Collaboration, I. Abt, et al. *Nucl. Instr. and Meth. A*, 386:310–347, 1997.
- [3] H1 Collaboration, I. Abt, et al. *Nucl. Instr. and Meth. A*, 386:348–396, 1997.
- [4] J. Burger et al. *Nucl. Instr. and Meth. A*, 279:217, 1989.
- [5] H1 FTD group, S. Burke, et al. *Nucl. Instr. and Meth. A*, 373:227, 1996.
- [6] H1 SPACAL group, R.D. Appuhn, et al. *Nucl. Instr. and Meth. A*, ??:?, 1996.
- [7] H1 calorimeter group, B. Andrieu, et al. *Nucl. Instr. and Meth. A*, 336:460, 1993.
- [8] G. Wolf. Hera Physics, February 1994. DESY 94-022.
- [9] F. Halzen and A.D. Martin. *Quarks and Leptons*. Wiley and Sons, Chichester, 1984.
- [10] C.Adloff H1 Collaboration et al. *Eur.Phys.J.*, C21:33, 2001.
- [11] A.C.Benvenuti BCDMS Collaboration et al. *Phys. Lett.*, B223:485, 1989.
- [12] R.P. Feynman. *Phys. Lett*, 23:1415, 1969.
- [13] J.D.Bjorken. *Phys. Rev*, 179:1547, 1969.
- [14] M. Breidenbach et al. *Phys. Rev. Lett*, 23:935, 1969.

- [15] F. Eisele. Invited Talk at the XVIII Physics in Collisions, Frascati, Italy, 1998. hep-ex/9807028.
- [16] V.N. Gribov and L.N. Lipatov. *Sov. J. Nucl. Phys*, 1972.
- [17] Yu.L. Dokshitzer. *Sov. Phys. JETP*, 46:641, 1977.
- [18] G. Altarelli and G. Parisi. *Nucl. Phys.*, 126:297, 1977.
- [19] E.A. Kuraev, L.N. Lipatov, and V.S. Fadin. *Sov. Phys. JETP*, 45:199, 1972.
- [20] Y.Y. Balitsky and L.N. Lipatov. *Sov. J. Nucl*, 28:822, 1978.
- [21] M. Ciafaloni. *Nucl. Phys.*, B296:49, 1988.
- [22] S. Catani, F. Fiorni, and G. Marchesini. *Nucl. Phys.*, B336:18, 1990.
- [23] G. Ingelman, A. Edin, and J. Rathsman. Lepto 6.5 - a Monte Carlo Generator for Deep Inelastic Lepton-Nucleon Scattering. DESY 96-057, (1996).
- [24] C. Adloff, H1 Collaboration, et al. *Z. Phys*, C76:613, 1997.
- [25] J. Breitweg, ZEUS Collaboration, et al. *Eur. Phys. J*, C1:81, 1998.
- [26] J.Bartels, J. Ellis, H. Kowalski, and M. Wusthoff. An analysis of diffraction in deep-inelastic scattering, 1998. DESY 98-034.
- [27] G. Ingelman, A. Edin, and J. Rathsman. Lepto 6.5 - a Montecarlo Generator for Deep Inelastic Lepton-Nucleon Scattering. DESY 96-057.
- [28] H. Jung. *Phys. Comm*, 86:147, 1995.
- [29] K.T.Donovan. *Hadronic Fragmentation Studies in ep Scattering at HERA*. PhD thesis, Department of Physics, Queen Mary and Westfield College, University of London, 1998.
- [30] G. Gustafson. *Phys. Lett*, 175B:453, 1986.

- [31] G. Gustafson and U. Pettersson. *Nucl. Phys.*, 306B:746, 1988.
- [32] B. Andersson, G. Gustafson, L. Lonnblad, and U Pettersson. *Zeit. Phys.*, C43:625, 1989.
- [33] B. Andersson, G. Gustafson, and L. Lonnblad. *Nucl. Phys.*, 339B:393, 1990.
- [34] L. Lonnblad. *Compt. Phys. Commun*, 71:15, 1992.
- [35] Ya.I.Azimov, Yu.L.Dokshitzer, V.A.Khoze, and S.I.Troyan. *Zeit. Phys.*, C31:213, 1986.
- [36] L.V.Gribovand Yu.L.Dokshitzer, V.A.Khoze, and S.I.Troyan. *Phys. Lett*, B202:276, 1988.
- [37] A.H. Mueller Yu.L. Dokshitzer, V.A Khose and S.I. Troyan. *Basics of Perturbative QCD*. Editions Frontieres.
- [38] R.P. Feynman and R.D.Field. *Nucl. Phys.*, 136B:1, 1978.
- [39] T. Sjostrand. *Comp. Phys. Comm*, 39:347, 1986.
- [40] T. Sjostrand and M. Bengtsson. *ibid*, 43:367, 1997.
- [41] M. Seymour. Monte Carlo Event Generators.
- [42] G.Marchesini et al. *Comput. Phy.Comm*, 67:13, 1989.
- [43] H1 Collaboration, C. Adloff, et al. Evolution of ep Fragmentation and Multiplicity Distributions in the Breit Frame. 29th International Conference on High Energy Physics ICHEP98, Vancouver, Canada, July 1998. No. 531.
- [44] Paul Thompson. *Open Charm Production in Inclusive and Diffractive Deep Inelastic Scattering at HERA*. PhD thesis, Department of Physics, University of Birmingham, 1998.

- [45] D.Kant and G.Thompson. The Triggering of DIS Data for Breit Frame Fragmentation Studies. H1-IN-589(12/2000).
- [46] P. Newman and P. Thompson. Private communication.
- [47] H. Jung. private communication.
- [48] H1 Collaboration, C. Adloff, et al. Evolution of ep Fragmentation and Multiplicity Distributions in the Breit Frame. *Nucl. Phys.*, B 504:3, 1997.
- [49] S. Bentvelsen, J. Engelen, and P. Kooijman. Reconstruction of x, Q^2 and Extraction of Structure Functions in Neutral Current Scattering at HERA. In W. Buchmuller and G. Ingelman, editors, *Physics at HERA*, volume 1, page 23, 1991.
- [50] R. P. Feynman and R. D. Field. *Nucl. Phys.*, 136B:1, 1978.
- [51] H1 Collaboration, C. Adloff, et al. Multiplicity structure of hadronic final states in diffractive deep-inelastic scattering at hera. *Eur. Phys. J.*, C5:439, 1998.
- [52] H1 Collaboration et al. Diffractive Jet Production in Deep-Inelastic ep Collisions at HERA. *Eur. Phys. J.*, C20:29, 2001.
- [53] M. Wusthoff K. Golec-Biernat. *Phys. Rev.*, D59:014017, 1999.
- [54] M. Wusthoff K. Golec-Biernat. *Phys. Rev.*, D60:114023, 1999.
- [55] J. Rathsman. *B452*, B452:354, 1999.
- [56] D.Kant. *A Study of Fragmentation of Quarks in ep Collisions at HERA using the H1 Detector*. PhD thesis, Department of Physics, University of London, 1995.
- [57] J.Turney. *A Study of Identified Hadron Fragmentation in ep Collisions at HERA using the H1 Detector*. PhD thesis, Department of Physics, University of London, Thesis in litt.

- [58] P.Dixon. *A Study of the Fragmentation of quarks in ep Collisions at HERA*.
PhD thesis, Department of Physics, University of Lancaster, 1998.
- [59] P.D. Acton OPAL Collaboration et al. *Zeit. Phys.*, C 53:539, 1992.
- [60] H1 Collaboration, I. Abt, et al. *Phys. Lett*, B328:176, 1994.
- [61] ZEUS Collaboration, J. Breitweg, et al. M.